# ABSTRACT

Title of dissertation: HOT CARRIER PLASMONICS

Tao Gong, Doctor of Philosophy, 2016

Dissertation directed by: Professor Jeremy Munday
Department of Electrical and Computer Engineering
Institute for Research in Electronics and Applied Physics

Despite the fact that 1 month of solar illumination contains vastly more energy than is stored in all of the earth's coal, oil, and natural gas reserves, solar power makes up much less than 1% of our power supply. The main reason for this discrepancy is the Cost/Watt of solar electricity. Traditional single-junction semiconductor solar cells are limited to a power conversion efficiency of approximately 30%, known as the Shockley-Queisser (SQ) limit. When photons with energy significantly greater than the bandgap energy of the semiconductor are absorbed, electrons and holes are generated with excess kinetic energy, so-called hot carriers. This extra energy is dissipated, *e.g.* by phonon emission (interaction with lattice). Further, for photons with energy below the bandgap energy, the absence of absorption results in no power generation.

Attempts to indirectly surpass the efficiency limit have been suggested using multiple junctions, multi-exciton generation, or the addition of an intermediate band within the semiconductor bandgap; however, many challenges remain for these

concepts. In the thesis, we will describe the methods and the underlying physics of photon detection and power conversion of both high and low energy photons using hot carrier effects before they lose their excess energy to heat.

For the absorption of high-energy photons, devices utilizing plasmonic nanostructures or three-layer stacks (transparent conductor-insulator-metal) can be used to generate and collect the hot carriers. We show experimental photocurrent generation from both monochromatic and broadband light sources, and uniform absorption for normal and oblique incident illumination. Power conversion efficiencies >10% are predicted with optimized structures. Excitation of the surface plasmon resonances further improves the device performance. In addition, we present a route to beating the SQ limit based on sub-bandgap photon absorption in a nanostructured metal contact followed by hot carrier injection. Our results provide a new pathway for high-efficiency photovoltaics that can be implemented using standard fabrication processes.

From a materials point-of-view, noble metals (gold and silver) are almost exclusively used in hot carrier plasmonic devices; however, many other materials may offer advantages for collecting hot carriers. We present results for several materials and show their potential applicability for hot carrier excitation and extraction. By considering the hot carrier distributions based on the electron density of states for the materials, we predict the preferred hot carrier type for collection and their expected performance under different illumination conditions.

By combining these concepts, hot carrier generation and collection can be exploited over a large range of incident wavelengths spanning the UV, visible, and IR.

Further work is also suggested to more fully explore the potential of this phenomenon and create a long-lasting impact on renewable energy generation.

# HOT CARRIER PLASMONICS

by

Tao Gong

Dissertation submitted to the Faculty of the Graduate School of the
University of Maryland, College Park in partial fulfillment
of the requirements for the degree of
Doctor of Philosophy
2016

Advisory Committee:
Professor Jeremy N. Munday, Chair/Advisor
Professor Martin Peckerar
Professor John Melngailis
Professor Edward Ott
Professor Lourdes G. Salamanca-Riba, Dean's representative

# Acknowledgments

I owe my gratitude to all the people who have helped and supported me all along and have made this thesis possible and because of whom my graduate research experience has been one that I will remember forever.

First and foremost I'd very much like to thank my advisor, Professor Jeremy Munday for giving me an invaluable opportunity to work on challenging and interesting projects over the past four years. He is very knowledgeable and experienced in the field and has provided countless help to me during my research. Besides, he is patient, considerate, and inspiring, and always thinks from the perspective of us students. It has been very fortunate and surely a great pleasure to work with and learn from such an extraordinary individual.

I would also like to thank Professor Martin Peckerar, Professor John Melngailis, Professor Edward Ott and Professor Lourdes G. Salamanca-Riba for agreeing to serve on my thesis committee and for sparing their invaluable time reviewing this thesis.

My colleagues in our laboratory have enriched my graduate life in many ways. We have spent these years doing research together. Though most of the time we have all worked independently on our specific projects, we have worked in an extremely cooperative and friendly environment where everyone loves to share ideas and help each other when in need. As an international student in particular, I have learned a lot from my colleagues through this cross-cultural communication and collaboration. Without them I could not have experienced such wonderful and meaningful research

life over the years.

I would also like to acknowledge help and support from some of the Nano-Center staff members. They have given me great training from the basics of fabrication to operating different Fablab equipment. They have always been there to help whenever I encountered any difficulty and questions.

I owe my deepest thanks to my family-my mother, father and elder brother who have always stood by me wherever I am. Although I have been living overseas alone, we have talked on the phone quite frequently. They have always encouraged and supported me and have pulled me through against the most difficult time in my life. They have been my spiritual forces. Words cannot express the gratitude I owe them.

My housemates at my place of residence have been a crucial factor in my finishing smoothly. I'd like to express my gratitude to Tiantao Lu, Qi Wang, Miao Wang and Mingwei Zhu for their friendship and support.

I would like to acknowledge financial support from the University of Maryland (UMD), the National Science Foundation (NSF) and Office of Naval Research (ONR).

It is impossible to remember all, and I apologize to those I've inadvertently left out.

# Table of Contents

# List of Tables

# List of Figures

# List of Publications

**Tao Gong** and Jeremy N. Munday, "Aluminum-based hot carrier plasmonics," (in review).

**Tao Gong**, Lisa Krayer and Jeremy N. Munday, "Upper limit of photovoltaic efficiency using hot carrier injection," (in review).

**Tao Gong**, Lisa Krayer and Jeremy N. Munday, "Design concepts for hot carrier-based detectors and energy converters in the near UV and IR," *J. Photon. Energy* (2016) (in press).

Qing Zhang, Wenzhong Bao, Amy Gong, **Tao Gong**, Dakang Ma, Jiayu Wan, Jiaqi Dai, Jeremy N. Munday, Jr-Hau He, Liangbing Hu and Daihua Zhang "A highly sensitive, highly transparent, gel-gated MoS2 phototransistor on biodegradable nanopaper," *Nanoscale* **8**, 14237-14242 (2016).

**Tao Gong**, Lisa Krayer and Jeremy N. Munday, "Hot electron detectors and energy conversion in the UV and IR," *Proc. of SPIE* **9608**, 96081C, doi:10.1117/12.2187605 (2015).

**Tao Gong** and Jeremy N. Munday, "Materials for hot carrier plasmonics," *Opt. Mater. Express* **5**, 2501-2512 (2015).

Yunlu Xu, **Tao Gong** and Jeremy N. Munday, "The generalized Shockley-Queisser limit for nanostructured solar cells," *Sci. Rep.* **5**, 13536 (2015).

**Tao Gong** and Jeremy N. Munday, "Angle-independent hot carrier generation and collection using transparent conducting oxides," *Nano Lett.* **15**, 147-152 (2015).

# Chapter 1: Introduction and Background

## 1.1 Overview

The field of plasmonics, which involves the coupling of light and free electron charge densities, has evolved rapidly over the past decade as a result of advances in nanofabrication techniques. Metallic nanostructures have enabled high electromagnetic field intensities near metal interfaces and have led to a range of devices including modulators, lasers, amplifiers, photovoltaic (PV) devices, sensors, nanocircuit elements, etc. [1–9, 11–16]. Surface plasmon interactions can typically be divided into two categories: localized surface plasmons (LSP) and propagating surface plasmon polaritons (SPP). For both cases, an incident electromagnetic wave couples to the free charges in the metal and creates a coupled oscillation at the metal-dielectric interface. These oscillations are typically confined to a small volume and lead to high field intensities. Larger metallic particles ($\sim$100 nm) cause enhanced scattering of the incident light, while smaller particles ($\sim$10s nm) lead to enhanced absorption [17, 20].

Traditionally, plasmonic structures have been applied to PV devices to increase the absorption within the semiconductor. However, the emerging field of hot carrier plasmonics is fundamentally different because the light is absorbed within the metal

to generate the so-called hot carriers (*i.e.* carriers with excess kinetic energy); therefore, the devices are based on metallic absorption rather than semiconductor absorption. In order to achieve high efficiency hot carrier generation and collection, significant light absorption in the metal is necessary through the coupling of incident light into surface plasmons [114, 116, 117]. The boosted light absorption contributes to the enhancement of hot carrier generation and consequently increases the device efficiency. Therefore, the surface plasmon effect is often employed in hot carrier-based devices. Hot carrier generation and collection enables utilization of energy that is usually lost in a conventional semiconductor device due to thermalization (*i.e.* phonon generation and heat dissipation resulting from absorption of high energy photons) and sub-bandgap photon loss (*i.e.* lack of absorption of low energy photons).

Research on the hot carrier effect dates back to the early twentieth century [22, 23]. Strictly speaking, the earliest experiments were the studies of photoemission, in which the incident photons excite electrons to higher energy states in metal, and the excited electrons with sufficiently high energy (greater than the work function of the metal) are able to escape from the metal into vacuum. Early experiments were mainly conducted in a vacuum chamber to prevent gases from impeding the flow of photoelectrons, and to also prevent the metal from being oxidized. These experiments on photoemission served mainly to understand the light-metal interaction, work function of metals and hot carrier generation and transport properties. For example, in copper and silver, the photoemission spectrum of electrons were comprehensively studied [95] to analyze the inelastic scattering of the excited

electrons. Endriz et al. [24] observed for the first time the photoemission induced by surface plasmon decay on a roughened aluminum surface, which in many ways paved the way for the study of hot carrier plasmonics.

In the late 1900s, the internal photoemission effect started to draw more attention, where rather than escaping into vacuum and becoming free carriers, the photo-generated hot electrons are injected through a barrier layer into a solid-state counter-electrode (either a metal or a semiconductor). Photocurrent induced by visible photons in metal-insulator-metal tunnel junctions was reported to aid in the understanding of the potential barrier shape at the metal-oxide interface [25,97,113]. Kovacs et al. [93] also studied the transport properties of hot carriers excited by high-energy photons (deep UV) and particles (argon ions). Braunstein et al. [100] considered hot electron attenuation during its traversal through the conduction band of the oxide layer in the opposite direction of the electric field as a result of scattering and other energy and momentum loss processes. As for the metal-semiconductor Schottky junction, Chan et al. [99] interpreted the internal photoemission mechanisms using a modified Fowler theory by incorporating a realistic peaked distribution of electron density of states (EDOS) in metals and considering hot carrier scattering and multiple reflection in thin metal films.

Despite extensive research on the photoemission effect, the work has mainly focused on the underlying physics of bulk structures, with only a few works exploring the possibility of energy extraction and other applications using this effect. The generation of hot carriers is very important to the operation of many semiconductor devices and detectors. For example, Gunn diodes, which display

negative differential resistance, operate based on hot electrons generated by strong electric fields [66]. Over the past few years, however, various hot carrier-based devices leveraging the excess kinetic energy of electrons excited directly by incident photons or by surface plasmon decay, have been drawing substantially increasing interest owing to the advancement of plasmonics and a new understanding of the useful applications enabled by this phenomenon. These hot carrier-based devices have several advantages over ones based on semiconductors alone. Specific benefits included tunable absorption, higher energy transfer per incident photon due to selective collection of high energy carriers, generation of carriers from sub-bandgap photons, and short thermalization times [26–28, 87], which have been used to alter chemical processes [29–31], to enable advanced energy conversion and photon detection [32–34, 79, 82, 92, 94, 105, 114, 134, 139], for nanoscopy [35], to modify thermally induced processes [36, 37, 136], to induce structure phase transition [38], etc. Hot carriers have extensive applications in photodetection [79, 82, 105, 114, 139], photovoltaics [92, 94, 134], photochemistry [31, 39], inducing phase transition [38] and luminescence [40] and etc.

Figure 1.1 shows the two basic structures that have been used to generate and collect hot carriers in metals: (i) Metal-Insulator-Metal (M-I-M) structures and (ii) Metal-Semiconductor (M-S) Schottky junctions. In either case, light is incident on the structure and is predominantly absorbed in one metallic contact (the left contact in Fig. 1.1(a)), which can be nanostructured to excite surface plasmons. The absorption either leads to the direct generation of hot carriers, or to surface plasmons, which subsequently decay into hot carriers. These carriers will diffuse,

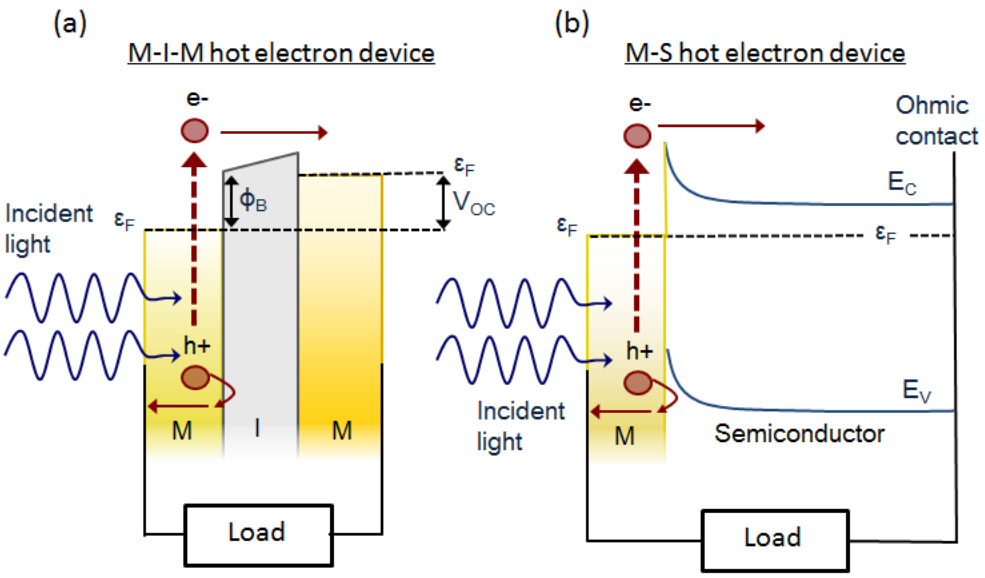


Figure 1.1: Schematic diagrams showing the operational principle of hot carrier plasmonic devices. (a) Absorption in the first layer of a Metal-Insulator-Metal (M-I-M) device generates hot electrons with kinetic energy great enough to traverse the insulating gap. (b) Illustration of a Metal-Semiconductor (M-S) hot carrier plasmonic device based on a Schottky interface.

and a fraction of them will find their way to the dielectric or semiconductor interface and will traverse it. For the M-I-M structure, a net current will flow based on the absorption profile within each metal and on the voltage established by the energy barrier for carriers to travel from one metal to the other. A similar effect is found for M-S devices with a Schottky junction.

## 1.2 Semiconductor-Free Hot Carrier Devices

Traditional photodetectors rely on semiconductor absorption to generate electron-hole pairs that result in photocurrent; however, hot carrier devices that exploit

metallic absorption do not need to include a semiconductor. Thus, simple structures can be constructed out of metals and dielectrics to achieve hot carrier current upon photo-excitation. One semiconductor-free approach can be achieved based on a simple M-I-M structure.

To determine the expected photocurrent from semiconductor-free hot carrier plasmonic devices, we simulated the response of various M-I-M structures. Figure 1.2 shows two devices: an M-I-M device based on a transparent conducting electrode (indium tin oxide, ITO) and a grating-based M-I-M device. Both structures result in preferential photon absorption on one side of the device. The M-I-M based on a transparent conducting electrode benefits from ease of fabrication, while maintaining large absorption of short wavelengths, whereas the grating structure provides an absorption spectrum with tunable resonances determined by the pitch, width, and height of the grating (Fig. 1.2(d)). For a planar ITO-$Al_2O_3$-Au structure (Fig. 1.2(a)), nearly all of the absorption occurs in the Au layer, making it an excellent candidate for a hot carrier plasmonic device. Light incident on the device passes through the glass, ITO, and $Al_2O_3$ with negligible absorption (<1%). Upon striking the Au surface an appreciable amount of light is absorbed within the first 20-40 nm of the film (*e.g.* ∼70% of the 460 nm light is absorbed within the first 30 nm). This satisfies two important criteria for an M-I-M hot carrier device: preferential absorption in only one conductor and absorption near the conductor-insulator interface. The simulated transparent conducting electrode device has a power conversion efficiency of ∼3% for 400 nm illumination and can reach ∼11% if the electron density of states is modified [94, 99, 118, 139, 140].

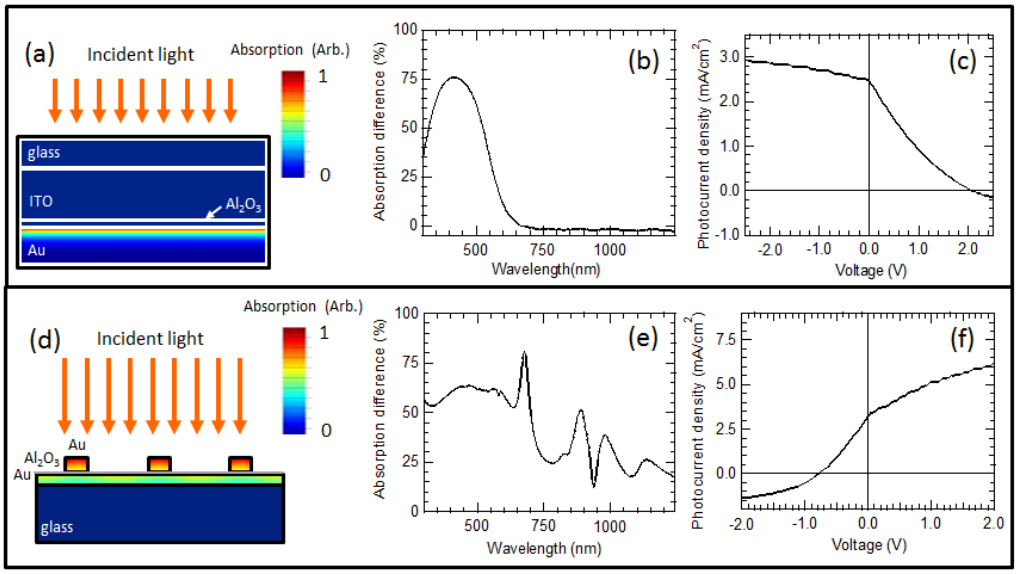


Figure 1.2: Optoelectronic simulations of hot carrier plasmonic devices. (a) Absorption simulation for an ITO-$Al_2O_3$-Au planar structure. High absorption is shown only on the Au side of the Au-$Al_2O_3$ interface. (b) The absorption difference between gold and ITO is large at short wavelengths. (c) Photocurrent-voltage characteristic shows photodetectors expected response and power generation (upper right quadrant of the current-voltage characteristic for this device). The applied voltage is the relative voltage drop between the bottom electrode and top electrode. (d) Absorption profile for a grating device coated with a thin layer of ITO on top as the top electrode. The width and height of the grating is 500 nm and 50 nm respectively, and the width of the slit is 100 nm. (e) Preferential absorption occurs in the grating, leading to a large absorption difference and hence the hot carriers flow from the grating to the thin film. (f) Photocurrent-voltage characteristic for the structure showing power generation in the upper left quadrant. Note the photocurrent increases as the applied voltage increases, which is different from (c). This is because the top layer is the main absorber in this case.

In order to achieve a large net photoresponse from an M-I-M hot carrier device, an asymmetric absorption profile is necessary. Further, the absorption should occur near the metal-insulator interface to aid in carrier traversal across the insulating barrier. In Fig. 1.2, the asymmetric absorption profile was obtained through either the use of a transparent metal contact (ITO), which absorbs negligible amounts of the incident light, or through the coupling to grating resonances, which yields higher fields and absorption in the grating compared to the thin Au film.

Many M-I-M geometries are possible, and we highlight three examples (Fig. 1.3). A planar geometry is the simplest to fabricate; however, achieving strong absorption in only one layer near the metal-insulator interface is difficult. Two routes have shown promise: (i) through the use of a low absorption, transparent conducting layer as discussed above [139] or (ii) through prism coupling to propagating surface plasmon modes [92]. A second promising direction is the use of nanoparticles or gratings [105]. Depending upon the design, the nanostructures can be used to either absorb the incident light or to scatter the light into the lower layer, where it is absorbed (Fig. 1.3(b)). A third option is the use of vertical nanostructures, such as nanowires or nanotubes. Nanowire arrays have proven advantages for photovoltaic applications because they enable a decoupling of the absorption length and the carrier diffusion length, because light is absorbed in the vertical direction, while carriers are collected horizontally. Similar advantages can be achieved for hot carrier devices (Fig. 1.3(c)).

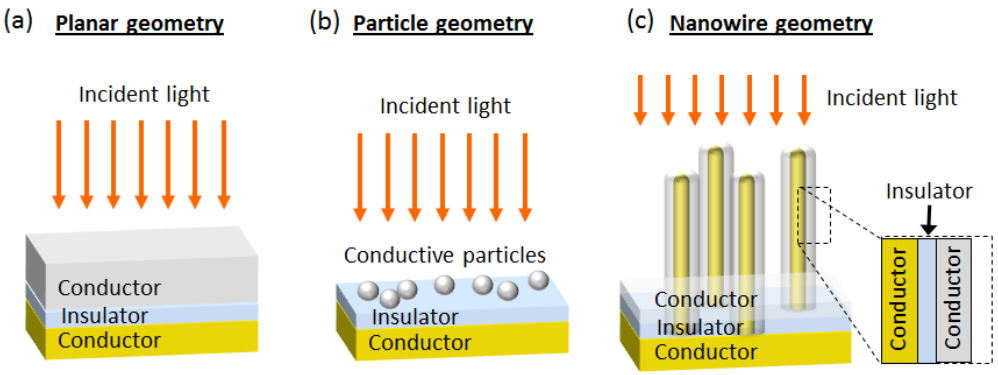


Figure 1.3: Three simple geometries for light absorption and subsequent hot carrier collection. (a) planar, (b) nanoparticle, (c) 3D nanowire or vertical nanostructure.

## 1.3 Sub-Bandgap Photocurrent In Semiconductors

In addition to M-I-M structures, M-S devices composed of metal nanostructures on a semiconductor can also lead to hot carrier excitation in the metal and subsequent collection within the semiconductor [79, 115]. Because the absorption is in the metal rather than the semiconductor, the incident photons do not need to have energy greater than the semiconductor bandgap energy in order to generate carriers. Thus, hot electron injection can enable sub-bandgap photo-detection.

Figure 1.4 shows one such device: a near IR detector made from Si and Au, with illumination from the Si side. As the period is increased, the absorption (which occurs in the metal) is red-shifted. As a result, the absorption peak can be tuned throughout the near IR where the Si is non-absorbing. The energetic carriers excited within the Au are injected into the Si and collected by an Ohmic contact. For photons with sufficiently low energy ($\lambda > 2\,\mu$m), carrier injection can be aided by

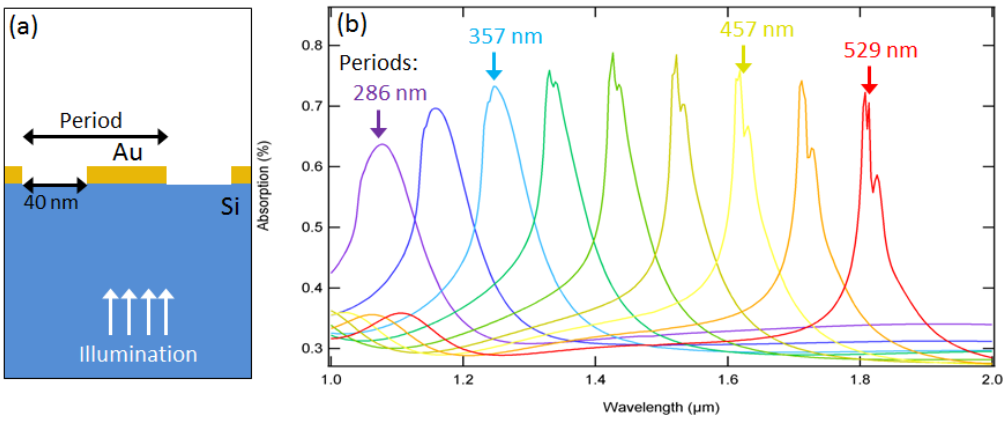


Figure 1.4: Tunable hot carrier plasmon photodetector. (a) Schematic of Si-Au-based device capable of detecting sub-bandgap photons due to plasmonic excitation and hot carrier injection into the Si. (b) Simulated absorption for the structure in (a) with an Au height of 15 nm and varied periodicity. As the period is increased, the absorption peak is red-shifted toward the IR.

the application of an applied external bias.

## 1.4 Hot Carrier Energy Converters

A large discrepancy exists between the maximum solar energy conversion efficiency predicted by the Carnot limit (95%) and that of the best-reported single junction solar cell (29.1%) [41]. This difference arises as a result of both extrinsic losses (*e.g.* series resistance, parasitic recombination, contact shadowing, etc.) and intrinsic losses (*e.g.* fundamental thermodynamic losses) [42]. Extrinsic loss accounts for less than 3% of the total loss in the record GaAs single junction solar cell; however, the intrinsic thermalization loss through phonon emission, along with the sub-bandgap photons not absorbed by the semiconductor, comprise the two main

loss mechanisms (∼46% loss in efficiency) for a single semiconductor junction solar cell.

The thermalization loss is the result of the energy mismatch between the energy of the incident photon and the energy of the collected electron-hole pair (see Fig. 1.5). A typical solar cell is made from a semiconductor with a *p*-*n* junction (in addition to window layers), which is able to absorb photons above the semiconductor bandgap energy. The absorption results in the generation of carriers, which can be collected. If the incident photon has energy in excess of the bandgap energy, that energy is transferred to the excited carriers; however, the carriers will quickly (on the timescale of pico- to nanoseconds) relax down to the semiconductor bandgap through the emission of phonons, *i.e.* lattice vibrations. These phonons generally represent a large loss mechanism. For example, if a 3.0 eV photon is incident on a 1.1 eV bandgap semiconductor, an energy loss of 1.9 eV is expected. Additionally, if the incident photon has energy below the energy of the semiconductor bandgap, all of the photons energy will be lost due to its inability to excite electron-hole pairs in the semiconductor.

In order to avoid these losses, a number of approaches have been attempted. These concepts are often referred to as the third generation photovoltaics. The most successful approach to date is the use of multiple semiconductors with different bandgaps [43–50, 67–69]. This approach allows one to reduce the energy mismatch between the semiconductor bandgap and the incident photon energy by sending photons within a specific energy band to a particular bandgap material. Each material contains a *p*-*n* junction, which can be connected electrically to form

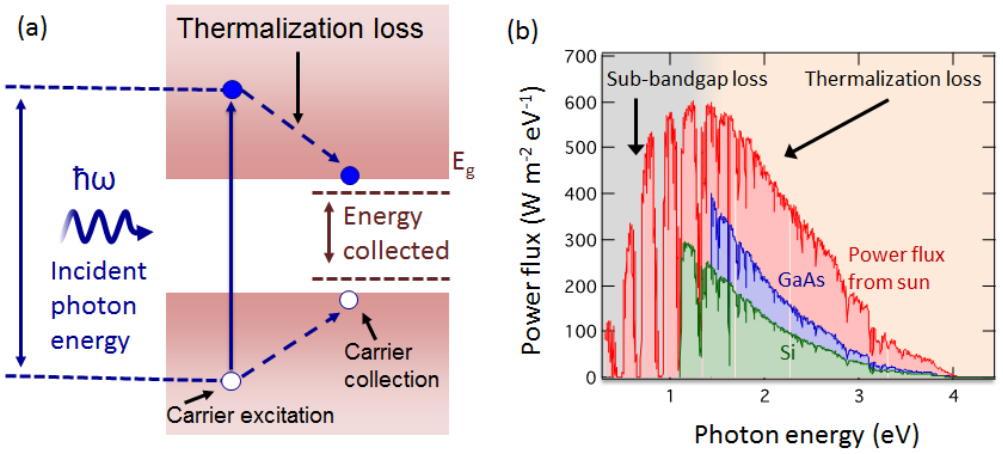


Figure 1.5: Thermalization loss mechanism. (a) Absorption of a high energy photon results in energy loss as the carrier relaxes down to the semiconductor bandgap. (b) Incident power flux from the sun (red) compared to the generated power flux from GaAs (blue) and Si (green). Power is lost from high energy photons due to thermalization. Low energy photons result in a loss due to their inability to excite electron-hole pairs.

a multi-junction device. This approach has resulted in a record solar cell with an efficiency of 46.0% [51], recovering an additional 16.9% of the total possible power when compared to the record single-junction device. In order to achieve efficiencies greater than 50%, further material developments are needed [46, 52, 68]. While multi-junction solar cells have surpassed the efficiency of single-junction devices, they require the union of different semiconductor materials that must be lattice-matched, strain-compensated, or formed into multiple adjacent devices (*e.g.* using spectrum splitting concepts) [68].

Other approaches to recovering the energy loss due to thermalization include multi-carrier excitation [55–57, 70, 72–75] and semiconductor-based hot carrier collection [58–63, 76–78]. Carrier multiplication effects are similar to impact ioniza-

tion effects in traditional semiconductors [64]; however, these effects are typically very small in bulk materials. In nanoscale semiconductor structures (*e.g.* quantum dots), quantum confinement effects can amplify this phenomenon to a measureable amount. Collection of hot electrons from a semiconductor has proven difficult due to short thermalization times (∼ps); however, results of Kempa *et al.* suggest that these effects are observable in ultrathin semiconductor film devices [62]. In general, all the third generation devices have been confined to efficiencies below the single-junction limit based on real-world difficulties that are unique to each technology. As stated in this thesis, the hot carrier generation/collection in metals is nonetheless a promising alternative to these concepts.

While efficiencies of >80% are the ultimate goal, plasmonic devices can be used in conjunction with traditional photovoltaic devices to improve their efficiency. Figure 1.6 shows a hybrid hot carrier plasmonic device coupled to a traditional solar cell. Rather than capture all of the light in the plasmonic structure, the metal in the M-I-M device is only used to capture high energy photons that are typically lost in a standard PV device (*e.g.* due to absorption in the passivating window layer) and separately the sub-bandgap photons are captured in the M-S device. Figure 1.6 shows one example, but various tandem or spectrum splitting schemes can be used. Here, the spectrum is broken up into three spectral regions and the photons are sent to the appropriate device.

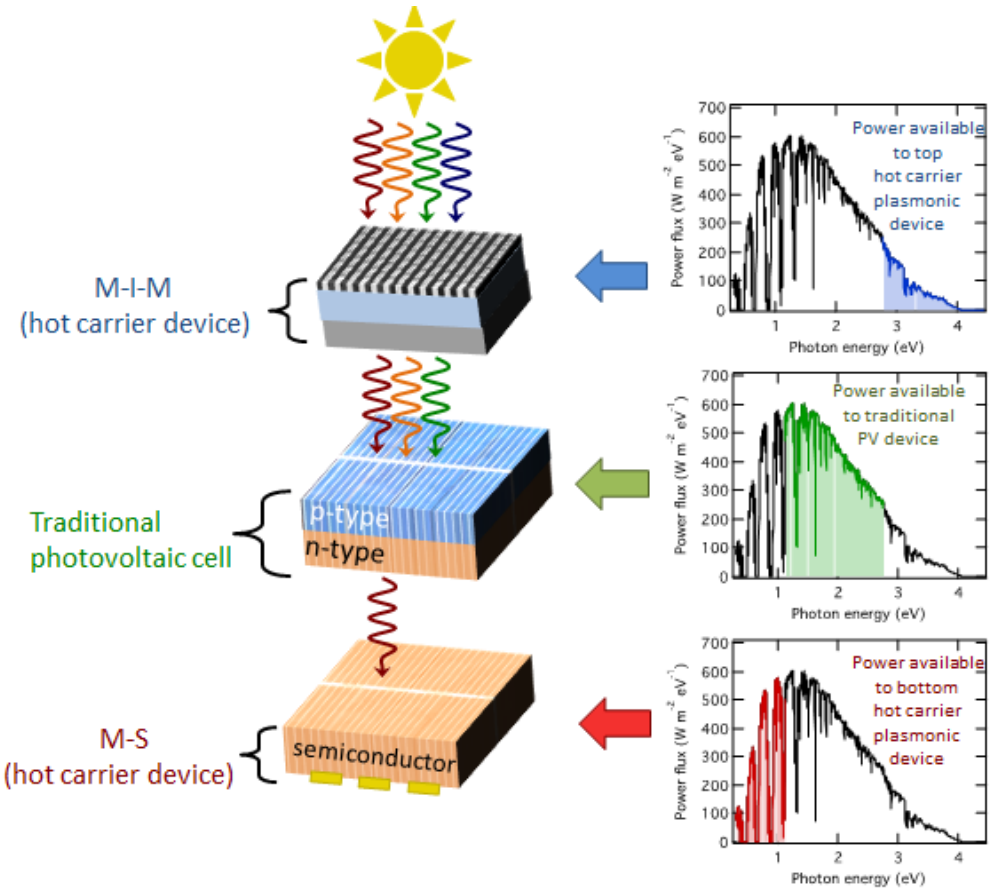


Figure 1.6: Schematic of a hybrid hot carrier effect solar device. A traditional solar cell is used to absorb a fraction of the solar spectrum and the hot carrier devices are used to capture photons that are usually inefficiently converted to energy in a traditional photovoltaic device. Thus, any added power generated by the plasmonic device will increase the total efficiency above that of the traditional PV device.

## 1.5 Outline of This Thesis

Many opportunities exist for using hot carrier effects in metals to create new detectors and solar energy harvesters. By taking advantage of concepts developed in plasmonics, devices can be tuned throughout the UV, visible, and IR ranges using a combination of metals, semiconductors, and insulators. Due to the short thermalization timescales associated with carrier cooling, ultra-fast detectors and sensors can be enabled using these concepts.

This thesis mainly consists of three topics: planar hot carrier devices, novel materials for hot carrier plasmonics, and a new high efficiency photovoltaic device exploiting hot carrier effects in metals. In the next two chapters, we present a new hot carrier device structure based on a transparent conducting oxide (TCO) electrode that enables efficient hot carrier generation and collection independent of incident illumination angle. The device consists of a simple TCO-insulator-metal (TCO-I-M) structure and requires no special coupling mechanism for the incident light. The hot carrier generation yields a wavelength dependent open-circuit voltage, and the device can be applied either for power generation or as a photodetector. Because the TCOs absorption is minimal, most of the incident light is absorbed in the metal layer and in the vicinity of the oxide interface, leading to highly anisotropic hot carrier flow and predicted power conversion efficiencies >10% under optimal conditions. We demonstrate that either using a traditional noble metal, like gold, or a naturally-abundant, but not widely used in the hot carrier field, like aluminum, can contribute to effective hot carrier generation and collection. In the following

chapter, we present the hot carrier energy distributions for 16 different materials (including metals, alloys, and nanostructures) based on the electron density of states (EDOS) determined by first principle calculations or experiments from the literature. We compare these distributions to the idealized distributions that would optimize the hot carrier injection. These results are meant to outline materials and nanostructures that might be most suitable for hot carrier collection and to provide an alternative perspective on choosing plasmonic materials when the goal is hot carrier generation. For the last part of the thesis, we present an additional third generation concept able to surpass the Shockley-Queisser (SQ) limit using an absorbing Schottky contact in conjunction with a *p*-*n* junction. This hybrid cell design enables sub-bandgap absorption and subsequent hot carrier injection, resulting in additional current generation from sub-bandgap photons. This mechanism is distinct from previous third generation hot carrier architectures, which aim to collect additional energy from carriers that are generated from above bandgap photons, rather than sub-bandgap ones. Finally, we conclude with an outlook for future work in the field.

Chapters 1, 2 and 4 are based on materials published in T. Gong *et al.*, "Hot electron detectors and energy conversion in the UV and IR," *Proc. of SPIE* **9608**, Infrared Remote Sensing and Instrumentation XXIII, 96081C, doi:10.1117/12.2187605 (2015), T. Gong *et al.*, "Angle-independent hot carrier generation and collection using transparent conducting oxides," *Nano Lett.* **15**, 147-152 (2015), and T. Gong *et al.*, "Materials for hot carrier plasmonics," *Opt. Mater. Express* **5**, 2501-2512 (2015). Chapters 3 and 5 are based on manuscripts currently in review: T. Gong

*et al.*, "Aluminum-based hot carrier plasmonics," (submitted), and T. Gong *et al.*, "Upper limit of photovoltaic efficiency using hot carrier injection," (in review).

# Chapter 2: Angle-Independent Hot Carrier Devices With TCOs

## 2.1 Overview

When high-energy photons are absorbed in a semiconductor or metal, electrons and holes are generated with excess kinetic energy, so-called hot carriers. This extra energy is dissipated, *e.g.* by phonon emission, which results in sample heating. Recovery of hot carriers is important for detectors, sensors, and power convertors; however, the design and implementation of these devices is difficult due to strict requirements on the device geometry, angle of illumination, and incident photon wavelength. Here we present for the first time a simple, angle-independent device based on transparent conducting electrodes that allows for the generation and collection of hot carriers. We show experimental photocurrent generation from both monochromatic and broadband light sources, uniform absorption for incident illumination at up to 60° from the surface normal, and find an expected open-circuit voltage in the range 1.5-3.0 V. Under solar illumination, the device is one order of magnitude more efficient than previous metal-insulator-metal designs and power conversion efficiencies >10% are predicted with optimized structures. This approach opens the door to new hot carrier collection devices and detectors based on transparent conducting electrodes.

The generation of electrons with sufficiently high kinetic energies, so-called hot electrons, is important to the operation of many semiconductor devices and detectors. For example, Gunn diodes, which display negative differential resistance, operate based on hot electrons generated by strong electric fields [66]. Alternatively, hot carrier generation in photovoltaic applications typically leads to energy loss. High-energy photons create hot carriers within the semiconductor, which relax to the bandgap through the emission of phonons and carrier collisions within pico- to nanoseconds. This carrier cooling (or thermalization) process accounts for a $\sim$46% loss in the overall efficiency of a photovoltaic device when illuminated by the solar spectrum, reducing the maximum efficiency of a single junction device to $\sim$33%. Indirect approaches to recovering this loss include the use of multi-junction devices [67–69] or semiconducting nanostructures capable of generating multiple carriers from a single photon [70–74]. While multi-junction devices have shown great potential, the direct collection of hot electrons in semiconductor solar cells has proven difficult [76–78].

Metal-semiconductor (M-S) interfaces have also been explored for hot carrier devices [79–87]. When a metal is illuminated, the electrons in the Fermi gas absorb the incident photons and generate hot electrons with energy higher than the Fermi level. The hot electrons can be injected into the semiconductor, which forms a Schottky junction with the metal, resulting in a Schottky photodetector that is capable of generating current from photons with energy insufficient to generate carriers within the bulk semiconductor. By exploiting localized plasmonic resonances, a silicon-gold device was found to yield an internal quantum efficiency (IQE) of 0.01$\sim$0.20% in

the near-IR, [79–81] and recently an enhanced photoresponse was found for 1.25 $\mu$m illumination using an Au metamaterial absorber (MPA) on Si [83]. Similarly, in the visible wavelength range (400-700 nm), all-solid-state devices based on $TiO_2$-Au/Ag nanospheres have been reported to exhibit external quantum efficiency (EQE) of 0.4%∼6.0%. [84, 86, 88] To further elucidate the physical mechanisms involved, a first principles calculation was recently used to provide a more comprehensive theoretical description of the hot carrier generation process in Ag nanoparticles. [87]

An alternative, semiconductor-free approach can be achieved based on a metal-insulator-metal (M-I-M) structure. Earlier work on M-I-M diodes showed promising results for power conversion and transmission based on the rectification property of these diodes under illumination in the microwave and IR wavelength range [89, 90]. While operation at optical frequencies has proven difficult, low efficiency rectification has been shown by exploiting plasmonic nanogaps [91]. Recently, a hot-carrier based M-I-M device was proposed by F. Wang *et al.* using a simple Au-$Al_2O_3$-Au junction [92]. To create anisotropic absorption, a Kretschmann prism coupling configuration was used to couple the incident light into a surface-plasmon-polariton (SPP) mode with the field intensity peaked at the interface between one of the Au films and air. The absorption occurs predominantly in the top Au layer, leading to preferential hot carrier flow from the top Au layer to the bottom one. However, due to this coupling mechanism, SPP modes can only be excited for a particular angle of incidence, which depends on the illumination wavelength. Therefore, for normal incidence illumination, the predicted optimized efficiency is reduced from 2-3% to ∼0.12%.

Here we demonstrate a new hot carrier device based on a transparent conducting oxide (TCO) electrode that enables hot carrier generation and collection independent of incident illumination angle. The device consists of a simple TCO-insulator-metal (TCO-I-M) structure and requires no special coupling mechanism for the incident light. The hot carrier generation yields a wavelength dependent open circuit voltage (in the range of 1.5-3.0 V), and the device can be applied either for power generation or as a photodetector that is almost independent of applied bias voltage within 0.5 V. Because the TCOs absorption is minimal, ∼80% of the incident light is absorbed in the metal layer and in the vicinity of the oxide interface, leading to highly anisotropic hot carrier flow and predicted power conversion efficiencies >10% under optimal conditions.

## 2.2 Device Fabrication and Experimental Setup

The device is fabricated by depositing an ITO layer of 30 nm thickness on a BK-7 glass substrate with a stainless-steel shadow mask, which has 4×4 aligned horizontal strips of 300 $\mu$m width. The sputtering is performed in an AJA sputtering unit at a rate of 70 Angstroms/minute with 200 W RF power. The amorphous $Al_2O_3$ layer is deposited in a Beneq TFS 500 Atomic Layer Deposition (ALD) system at 150 Angstroms/minute. 55 operation cycles (resulting in approximately 5 nm of $Al_2O_3$) are used to ensure accurate and conformal coverage of $Al_2O_3$ over the underlying surface. The topmost 80 nm gold layer and 2 nm Ti adhesion layer are deposited with another shadow mask with the 4×4 vertically aligned strips in a Temescal

electron beam deposition system to form a cross junction for the device. Lastly, electrical contact is made to the ITO by attaching a wire to the surface using Chemtronics CW2400 Epoxy A and B mixture. The other contact is realized by directly connecting a probe to the gold electrode.

The optical absorption measurement is conducted by using a 6" Labsphere integrating sphere and a Thermo Oriel xenon lamp as the light source. The white light from the lamp is separated into different wavelengths with a SPEX 500M spectrometer. The photocurrent measurement is performed under chopped illumination of a monochromatic collimated beam from a Fianium WhiteLase Supercontinuum laser source. For the electrical measurement, the sample is connected to a Keithley 2400 SourceMeter, acting as a voltage source and current meter, and to a SR830 DSP lock-in amplifier.

## 2.3 Device Design and Modeling

The performance of a hot carrier device can be determined by considering the following processes: (i) photon absorption, (ii) hot carrier generation, (iii) hot carrier propagation, and (iv) subsequent collection. The detailed modeling for each process [81, 92–101] is elaborated in the following subsections.

### 2.3.1 Device Structure and Its Working Principle

Figure 2.1(a) shows the schematic of a simple planar structure consisting of indium tin oxide (30 nm)-aluminum oxide (5 nm)-gold (80 nm) under illumination.

The indium tin oxide (ITO) acts as the transparent conductor and the aluminum oxide ($Al_2O_3$) is used as the thin insulating barrier to separate ITO and Au. For illumination wavelengths between 300 nm and 600 nm, absorption predominantly occurs in the Au, leading to a highly anisotropic absorption profile (Fig. 2.1(a), 2.1(c)). This exponential decay in the Au promotes electrons in the Fermi gas to higher energy states, simultaneously leaving behind empty hole states. This process leads to preferential hot carrier generation near the Au-$Al_2O_3$ interface. These hot carriers will subsequently diffuse, during which time they are scattered by the electron gas. The timescale of the electron-electron interaction is 500 fs [84, 101] for gold; thereafter these carriers thermally relax producing heat by electron-phonon scattering. Therefore, only a fraction of the carriers find their way to the Au-$Al_2O_3$ interface. Depending upon the energy and momentum of the carriers that reach the interface, they will either traverse or tunnel through the insulating barrier, ultimately being collected as photocurrent at the ITO electrode (Fig. 2.1(b)). Because of the preferential absorption in Au, the carriers predominately flow from Au to ITO with a voltage established by the energy barrier between the two electrodes. Thus, for the hot carrier device, the electrodes function as the light absorber, carrier emitter, and carrier collector simultaneously.

Once the absorption is calculated within the device, the opto-electronic response can be determined. The photocurrent-voltage ($I$-$V$) characteristic for the device is obtained by the summation of the four current contributions arising from the hot electrons and hot holes from both electrodes (see detailed model in the following sub-section).

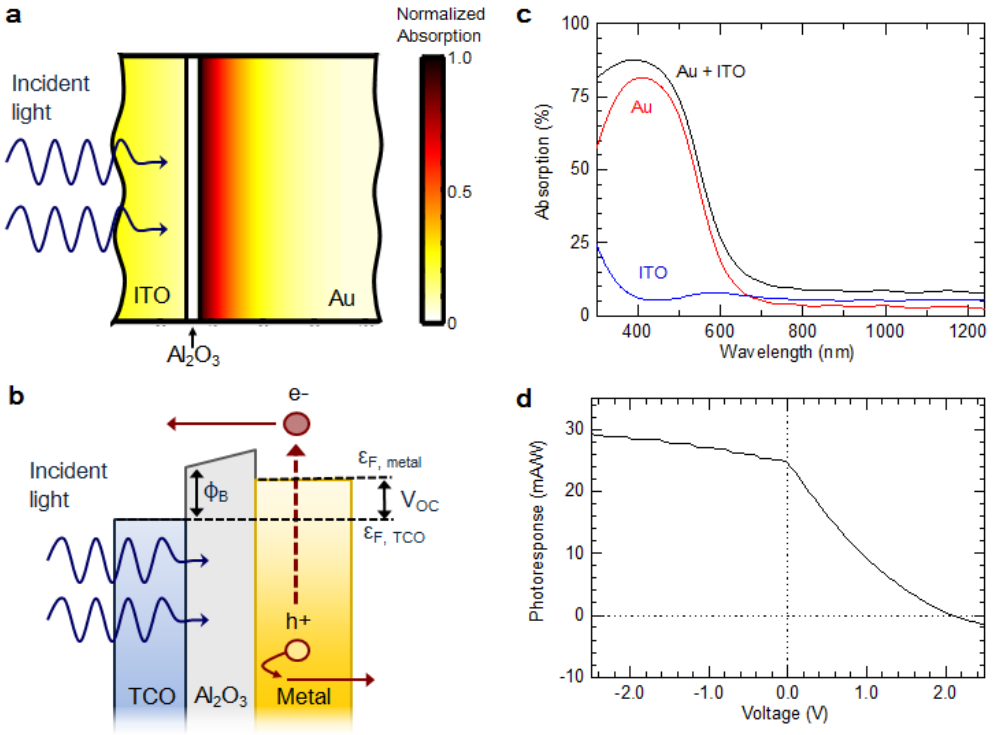


Figure 2.1: Schematic of the hot carrier device and calculated performance. (a) Cross-section of the device under normal incidence illumination. The color scale represents the spatially varying light absorption profile calculated by finite difference time domain simulation. (b) Schematic of the hot carrier generation and injection through the insulating barrier while illuminated. (c) Calculated light absorption in the ITO layer, the Au layer, and the total absorption. (d) Calculated photocurrent under AM1.5G illumination and applied bias. The electron density of states is assumed to be parabolic for the calculation.

The currents depend on the incident spectrum, spatially dependent absorption, bias voltage, electron density of states (EDOS), bandgap of the oxide, barrier height ($\Phi_B$), and the mean-free-paths (MFP) of the carriers. The barrier height at the interface is 0.4 eV for the calculation of optimal performance [92] and the MFPs of Au and ITO are obtained from the literature [92, 93, 103–105].

### 2.3.2 Optical Properties of Gold

The incident light from normal incidence can drive the oscillation of the free electrons (i.e. the plasma model) in gold, but neither at the bulk plasmon resonance nor at the surface plasmon polariton (SPP) resonance, as can be seen from the dispersion relation in Fig. 2.2. The dispersion relation is obtained based on the equations [18, 19]:

$$k_{bulk} = \frac{\omega}{c}\sqrt{1 - \frac{\omega_p^2}{\omega^2 + \gamma^2}}$$

$$k_{spp} = \frac{\omega}{c}\sqrt{\frac{\omega^2 + \gamma^2 - \omega_p^2}{2\omega^2 + 2\gamma^2 - \omega_p^2}} \tag{2.1}$$

where $\gamma$ is the damping coefficient. Usually in a thin metal film, the damping rate is higher than that in the bulk counterpart. This phenomenon is because a thin metal film contains many small grains, which gives rise to additional grain-boundary scattering for free electrons and increases losses. The damping rate in a thin metal film is give by [142]:

$$\gamma = \gamma_0 + A\frac{v_F}{d} \tag{2.2}$$

where $\gamma_0$ is the damping rate for the bulk metal, $A$ is a dimensionless empirical constant which is usually assumed to be close to unity [20, 21], $v_F$ is the Fermi velocity of the electrons in the metal and $d$ is the average grain size. In addition, rough surfaces and edges of thin metal films can lead to more scattering losses [142].

The surface plasmon polariton is excited at the gold-air interface, with the SPP frequency $\omega_{spp} \simeq \omega_p/\sqrt{2} = 9.76 \times 10^{15}$ Hz, corresponding to 195 nm illumination wavelength. The bulk plasmon frequency in gold corresponds to an incident wavelength of ∼140 nm, thus illumination at >300 nm is unable to excite this oscillation. Alternatively, the SPP could be excited if there were an appropriate grating or prism to compensate the momentum mismatch from free space as was done in previous experiments [92, 105]; however, no such coupling mechanism is present (or needed) in our experiment. As a result of the negative dielectric function of the gold in the wavelength range of our experiment, light only penetrates into the metal ∼10-20 nm (*i.e.* skin depth), and exhibits an exponential-like absorption profile as in Fig. 2.1(a) in this chapter. It is this exponential absorption that leads to excitation of hot carriers.

The absorption mechanism in metal is more complicated than a simple Drude model can describe. Specifically, the absorption in gold within the wavelength range of 300-600 nm contains components due to both intraband free carrier absorption and interband (d-band to conduction band) absorption [82, 84, 85]. We use a modified analytic model [141] to calculate the dielectric function for gold. Based on this model, the dielectric function can be described well by introducing two terms for

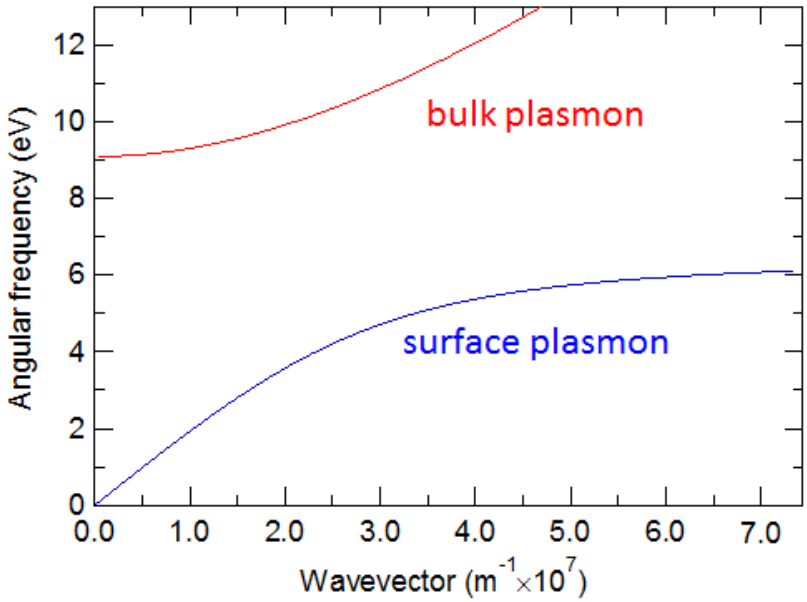


Figure 2.2: Dispersion relation of the bulk plasmon (red) and surface plasmon polariton (blue) in gold. The corresponding wavelength of incident light that is able to excite the bulk plasmon is <140 nm, and the wavelength of incident light that is able to excite the surface plasmon is >195 nm.

the interband transition in addition to the Drude term [141]:

$$\varepsilon(\lambda) = \varepsilon_\infty - \frac{1}{\lambda_p^2\left(\frac{1}{\lambda^2} + \frac{i}{\Gamma_p \lambda}\right)} + \sum_{j=1,2} \frac{A_j}{\lambda_j}\left[\frac{e^{i\Phi_j}}{(\frac{1}{\lambda_j} - \frac{1}{\lambda} - \frac{i}{\Gamma_j})} + \frac{e^{-i\Phi_j}}{(\frac{1}{\lambda_j} + \frac{1}{\lambda} + \frac{i}{\Gamma_j})}\right] \tag{2.3}$$

where $\varepsilon_\infty$ is the high-frequency limit dielectric constant, $\lambda = 2\pi c/\omega$ (incident light wavelength), $\lambda_p = 2\pi c/\omega_p$ (plasma frequency expressed as wavelength), $\Gamma_p = 2\pi c/\gamma$ (damping rate expressed as wavelength), $\lambda_i = 2\pi c/\omega_i$ (interband transition frequency expressed as wavelength), $\Gamma_i = 2\pi c/\gamma_i$ (transition broadenings expressed as wavelength).

As indicated in Fig. 2.3, Drude model assumes free electron oscillation and the imaginary part of the dielectric function at long wavlengths represent the free electron intraband transition loss. However, at short wavelengths, Drude model fails. This is because the interband transition losses are high and play a much more important role in the short-wavelength light absorption.

Nontheless, even in the short wavelength range, hot carrier generation has been successfully modeled (and compared to experiments) by including the free carrier intraband transition under the parabolic EDOS assumption [92, 105]. Reineck *et al.* [84] also reported experimentally that the hot carrier generation due to the d-band absorption was negligible in a gold nanoparticle-$TiO_2$ junction-based device for wavelengths shorter than 500 nm. Therefore in this chapter we model the EDOS in two different ways to get a range of expected values to explain our experimental results. We will consider first a simple parabolic EDOS derived from the free electron Drude model, and then a modified EDOS which represents a peaked electron energy distribution slightly below the Fermi-level due to the band-overlapping effect (just

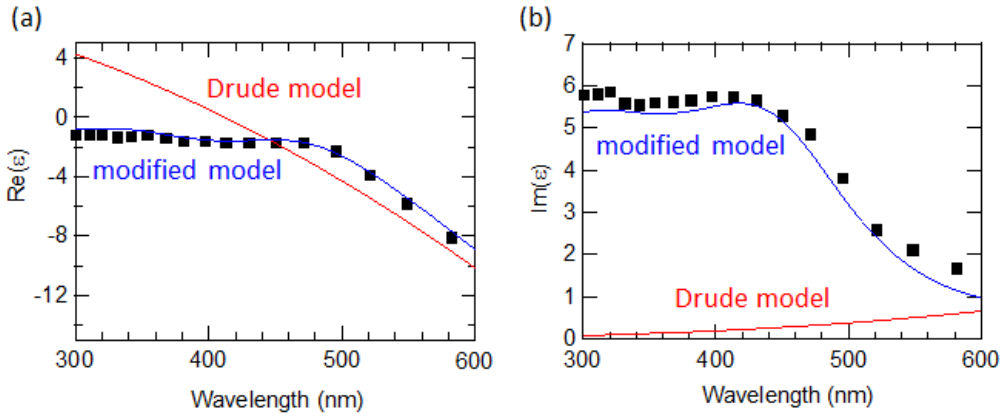


Figure 2.3: Two models used to fit the dielectric function of gold. (a) Real part and (b) imaginary part of the dielectric function. The wavelength of the incident light that drives the charge oscillation in gold is within the visible range. The simple Drude model (red solid line) fits the experimental data (markers) well enough at the long wavelength range, but fails at the short wavelengths. The modified model (blue solid line) incorporates additional terms for the interband transition, which dominates in the light absorption at short wavelengths.

like d-band in gold) to determine the maximum available conversion efficiency.

### 2.3.3 Detailed Hot Carrier Generation and Transport Model

When incident light is absorbed in the metal, the absorbed power density is given by:

$$abs(\mathbf{r},\omega) = \frac{1}{2}\varepsilon_i \omega |\mathbf{E}(\mathbf{r},\omega)|^2 \tag{2.4}$$

where $\varepsilon_i$ is the imaginary part of the permittivity function of the absorber (*e.g.* Au or ITO), $\omega$ is the angular frequency of incident light, and $\mathbf{E}(\mathbf{r},\omega)$ is the electric field at position $\mathbf{r}$. Assuming one absorbed photon excites one hot electron-hole pair, the

density of hot carriers is:

$$N_e(\mathbf{r},\omega) = N_h(\mathbf{r},\omega) = N_{ph}(\mathbf{r},\omega) = abs(\mathbf{r},\omega)/\hbar\omega \tag{2.5}$$

The density of the generated hot electrons, hot holes and the absorbed photons are denoted as $N_e(\mathbf{r},\omega)$, $N_h(\mathbf{r},\omega)$, $N_{ph}(\mathbf{r},\omega)$, respectively. And the total absorbed photon density is simply the summation over all angular frequencies:

$$N_{ph}(\mathbf{r}) = \sum_{\omega} N_{ph}(\mathbf{r},\omega) \tag{2.6}$$

For an electron with initial energy $\xi'$ absorbing a photon with angular frequency $\omega$, the transition rate to a new energy state, $\xi(> \xi_f) = \xi' + \hbar\omega$, is proportional to the product of the Fermi distribution function $f(\xi')$ and the electron density of states (EDOS), $g(\xi')$. The probability density that a hot electron ends up with energy $\xi$ after absorbing a photon of angular frequency $\omega$ is found to be:

$$P_0(\xi,\omega) = \frac{f(\xi')g(\xi')}{\int_{\xi_f-\hbar\omega}^{\infty} f(\xi')g(\xi')\,\mathrm{d}\xi'} \tag{2.7}$$

where $\xi_f$ is the Fermi level of the metal (for gold $\xi_f \simeq 5.5\,\mathrm{eV}$). The momentum conservation selection rule for the transition is neglected for this calculation, and is in good agreement with photoemission experiments for a range of noble metals [99]. $P_0(\xi,\omega)$ is assumed to be nearly uniform given that the final state is far away from the bandedge of the absorbing metal, and the previous result reduces to [92, 93]:

$$P_0(\xi,\omega) = \begin{cases} 1/\hbar\omega, & \xi_f \le \xi \le \xi_f + \hbar\omega \\ 0, & \xi > \xi_f + \hbar\omega \end{cases} \tag{2.8}$$

Under broadband illumination, the spatially dependent hot electron probability density is:

$$P_0(\mathbf{r},\xi) = \sum_{\omega} \frac{N_{ph}(\mathbf{r},\omega)P_0(\xi,\omega)}{N_{ph}(\mathbf{r})} \tag{2.9}$$

Combining these results, we obtain:

$$P_0(\mathbf{r},\xi) = \begin{cases} \frac{\frac{N_{ph}(\mathbf{r},\omega_1)}{\hbar\omega_1}+\frac{N_{ph}(\mathbf{r},\omega_2)}{\hbar\omega_2}+...+\frac{N_{ph}(\mathbf{r},\omega_n)}{\hbar\omega_n}}{N_{ph}(\mathbf{r})}, & \xi_f \le \xi \le \xi_f + \hbar\omega_1 \\ \frac{\frac{N_{ph}(\mathbf{r},\omega_2)}{\hbar\omega_2}+\frac{N_{ph}(\mathbf{r},\omega_3)}{\hbar\omega_3}+...+\frac{N_{ph}(\mathbf{r},\omega_n)}{\hbar\omega_n}}{N_{ph}(\mathbf{r})}, & \xi_f + \hbar\omega_1 < \xi \le \xi_f + \hbar\omega_2 \\ \vdots & \\ \frac{\frac{N_{ph}(\mathbf{r},\omega_n)}{\hbar\omega_n}}{N_{ph}(\mathbf{r})}, & \xi_f + \hbar\omega_{n-1} < \xi \le \xi_f + \hbar\omega_n \end{cases} \tag{2.10}$$

Hot holes have a similar probability density but with an energy that lies in a range below the Fermi level rather than above it.

Next we determine the fraction of exited carriers that reach the energy barrier. After being excited to the higher energy level, the carriers begin to diffuse isotropically under the assumption of a perfectly parabolic energy distribution with respect to the $k$-vector of the free carriers. Thus, the angular distribution of the probability density of a hot carrier is $P_0(\mathbf{r},\xi;\theta,\varphi) = P_0(\mathbf{r},\xi)/4\pi$. During the propagation of the carriers toward the interface, they can be scattered both elastically and inelastically. We only consider the probability density of a carrier ballistically reaching the interface without being scattered. The probability density that an excited carrier reaches the insulating barrier is [93]:

$$P_1(\mathbf{r},\xi;\theta) = \exp\left(-\frac{\Delta l}{\lambda_{ee}(\xi)\cos(\theta)}\right) \tag{2.11}$$

where $\Delta l$ is the distance from the hot carriers initial position right after being excited to the interface, and $\lambda_{ee}(\xi)$ is the inelastic mean-free-path (MFP) of an electron

in the metal, which varies with carrier energy $\xi$ by the random phase approximation (RPA) [93]. For visible wavelength illumination in gold, $\lambda_{ee}$ is approximately 35$\sim$40 nm. For a hot hole excited to the same amount below $\xi_f$, the MFP is similar to that of the electron.

Next we consider the fraction of carriers that are able to traverse the insulating barrier. As long as the barrier is very thin ($\sim$4-5 nm), the barrier shape is approximately linearly with applied bias, resulting in a trapezoidal shape for the energy bands. For this calculation, we neglect distortions at the interface arising from interface dipoles, traps, or metal defects in the insulating film. The probability of a carrier getting over or through the barrier and occupying an empty state at the metal on the other side is given by: [93]

$$P_2(\xi,\theta,V) = \begin{cases} \exp\left\{-2\int_0^{d_{ox}} [-k_z^2(\xi,\theta,z',V)]^{1/2}\,\mathrm{d}z'\right\}, & \xi < max(\xi_{f1}+\Phi_{B1}, \xi_{f2}+\Phi_{B2}) \\ 1, & Otherwise \end{cases} \tag{2.12}$$

where $\xi_{f1}$, $\xi_{f2}$, $\Phi_{B1}$, $\Phi_{B2}$ are the Fermi levels and barrier heights for electrode 1 (Au) and electrode 2 (ITO) under an applied bias voltage $V$, respectively. $d_{ox}$ is the thickness of the oxide film. $k_z$ is the momentum along the direction normal to the interface, which is obtained from: [93]

$$k_z^2 = \frac{2m}{\hbar^2}\left\{\frac{[\xi - E_c(V,z')][\xi - E_c(V,z') + \xi_g]}{\xi_g} - (\xi - \xi_z)\right\} \tag{2.13}$$

$E_c(V,z')$ is the conduction band edge of the oxide layer which depends on bias voltage $V$ and on the position $z'$ inside the oxide. $\xi_g$ is the bandgap of the insulator. For amorphous $Al_2O_3$, the bandgap is $\sim$6 eV, which is smaller than its crystalline

counterpart sapphire ($\sim$8.3 eV) [93, 113]. The tunneling probability is calculated under WKB approximation [92], which is reasonable because the variation of the barrier across the insulator is much slower than the oscillation of the wavefunction of the carriers. We also note that under very high bias, the state on the opposite metal may already be occupied and the probability of transmission will be zero in terms of the Pauli exclusion principle.

Finally, we calculate the total current by considering the total flow of all carriers in both directions across the barrier. The total hot electron current flowing from Au to ITO is:

$$I_e^{Au-ITO}(V) = \int_{\xi_{f1}}^{+\infty} e \cdot n_{Au}(\xi, V)\,\mathrm{d}\xi \tag{2.14}$$

where $n_{Au}(\xi, V)$ is the total number of hot electrons per unit time that contribute to photocurrent from Au to ITO, which is given by:

$$n_{Au}(\xi, V) = \iiint_{\Phi(\mathbf{r},\theta),\theta(\mathbf{r}),\mathbf{r}} N_{ph}(\mathbf{r}) P_2(\xi, \theta, V) P_1(\mathbf{r}, \xi; \theta) P_0(\mathbf{r}, \xi; \theta, \varphi)\,\mathrm{d}\varphi \sin(\theta) \mathrm{d}\theta \mathrm{d}\mathbf{r} \tag{2.15}$$

In the end, the total current is the summation of the four contributions from both hot electrons and hot holes flowing from both electrodes:

$$I(V) = I_e^{Au-ITO}(V) - I_e^{ITO-Au}(V) - I_h^{Au-ITO}(V) + I_h^{ITO-Au}(V) \tag{2.16}$$

In the above carrier transmission calculation, several reasonable approximations are made, which could be further refined in future calculations. Ideally, the electrons with energy greater than the barrier height will all traverse the barrier. However, only the carriers with high enough momentum component in the normal direction to the interface could possibly overcome the barrier directly [94]. However,

while traversing the barrier, carriers could be subject to scattering or other energy or momentum loss processes [100] due to the potential energy gradient across the junction, especially under bias. This effect makes the transmission probability different between the two directions (Au to ITO and ITO to Au) and always lower than unity. In addition, the image potential caused by an image charge induced by a hot carrier when traversing the barrier would also have an interaction with the traversing carrier, which would effectively reduce the height and width of the barrier [93].

## 2.4 Performance of the Device

### 2.4.1 Theoretical Photoresponse of the Device

Figure 2.1(d) shows the calculated $I$-$V$ response under AM1.5G solar illumination. For $V < 0$, the photocurrent increases slowly with increasing negative bias, indicating that most of the current comes from hot electrons flowing from the Au to ITO. These electrons have high enough energy to directly traverse the barrier. Alternatively, for $V > 0$, the total current drops faster with increasing bias. In this region, the barrier height seen by the hot electrons in Au is increased and tunneling becomes necessary for those electrons with lower energy ($\Phi_B < \xi < \Phi_B + qV$), thus causing a faster decrease in the current. With larger bias, the current flow becomes negative as reverse electron flow from the ITO to the Au dominates the total current. Meanwhile the hot electrons generated in Au will find no empty states in ITO to occupy. The contribution to the currents due to the hot holes is also considered;

| Wavelength (nm) | 400 | 500 | 600 | 700 |
|---|---|---|---|---|
| EQE (%) | 17.8 | 13.3 | 3.1 | 1.34 |
| PCE (%) | 3.10 | 2.24 | 0.47 | 0.19 |
| $V_{oc}$ (V) | 2.79 | 2.15 | 1.46 | 1.12 |
| Au absorption (%) | 78.1 | 60.3 | 14.1 | 6.3 |
| ITO absorption (%) | 8.5 | 8.3 | 9.1 | 6.7 |

Table 2.1: Calculated performance of the hot carrier device with parabolic EDOS. EQE, PCE, and $V_{OC}$ represent the external quantum efficiency, power conversion efficiency, and open-circuit voltage of the device, respectively. Higher energy incident photons result in a larger $V_{OC}$ and efficiency. At 400 nm, the PCE reaches to 3.1%, which is comparable to the calculated results obtained with a gold-insulator-gold device with Kretchmann SPP coupling prism [92].

however, their contribution is negligible due to the much larger energy barrier experienced by the hot holes. The overall power conversion efficiency (PCE) is calculated to be 0.95%, which is 8 times the value of a planar Au-$Al_2O_3$-Au junction under normal incidence illumination [92]. For monochromatic illumination at shorter wavelengths, the PCE can reach 3.1% (Table 2.1), which is comparable to the results of the planar Au-$Al_2O_3$-Au junction with the Kretchmann SPP prism coupling [92]; however, no special coupling mechanism is necessary for the TCO-based structure.

Another important parameter associated with the $I$-$V$ characteristic is the fill

factor (FF), which represents how square the $I$-$V$ curve is:

$$FF = \frac{I_{max}V_{max}}{I_{SC}V_{OC}} \tag{2.17}$$

where $I_{max}$ and $V_{max}$ are the current and voltage at max power, and $I_{SC}$ and $V_{OC}$ are the short circuit current and open circuit voltage, respectively. A larger fill factor corresponds to a more rectangular $I$-$V$ curve, and hence a higher efficiency device. In our device, the fill factor (Fig. 2.1(d)) can be improved by modifying the EDOS. To determine the effect of EDOS modification on the device characteristic, two simple models were considered. First, for the above calculations, the EDOS in the metal is assumed to be parabolic, as it would be for a free electron gas. Under this assumption, the generated hot electrons (holes) possess a nearly uniform energy distribution above (below) the Fermi level. Therefore, a large fraction of the hot carriers have an energy lower than the barrier height, which makes traversing the barrier less probable. The efficiency can be further improved if the electrons in the Fermi gas before excitation possess a non-parabolic EDOS. For the second model, we consider the EDOS to have a peak distribution of carriers close to but below the Fermi level, as described below. For most metals, the EDOS is not perfectly parabolic and depends on the crystallography and film thickness. The resulting EDOS may also contain many peaks due to the overlapping bands. For hot carrier generation and collection, the ideal case occurs when most of the electrons in the Fermi gas possess an energy in the vicinity of Fermi level, $\xi_f$, before excitation, which is thought to occur in some noble metals [99]. After illumination, almost all excited hot electrons would be distributed in a narrow energy range above the

barrier height (Fig. 2.4(a)). For this case, nearly all hot electrons can traverse the barrier even under positive bias, and the fill factor in the power generation region is significantly improved from 19% to 44% (Fig. 2.4(b)). In this model, we modify the EDOS by assigning an effective conduction bandedge to be 0.15 eV below the Fermi level [99]. As a result, the PCE improves to 2.33% under AM1.5G solar illumination and reaches 10.7% at short wavelength illumination (Table 2.2). Figure 2.5 indicates that the power conversion efficiency is improved for all incident wavelengths with the modified EDOS. More substantial EDOS modification may be possible through the utilization of silicide alloys or by exploiting quantum confinement effects in nanoscale materials [106, 107].

### 2.4.2 Photoresponse Under Monochromatic and Broadband Illumination

The photoresponse of the device was experimentally determined over a wavelength range of 400-700 nm and was found to exhibit increased photocurrent for short wavelengths (Fig. 2.6(a)). The enhanced photoresponse is due to the large absorption at the Au surface relative to the absorption in the ITO. The photoresponse is consistent with the simulated light absorption spectrum, which is also observed in Au-Si photodetectors [79–81, 84]. The photoresponse and the absorption differ slightly because the photoresponse depends on both the hot carrier emission/collection and the absorption. Under white light illumination, the hot carrier device is found to generate nearly constant current under both forward and reverse bias (Fig.

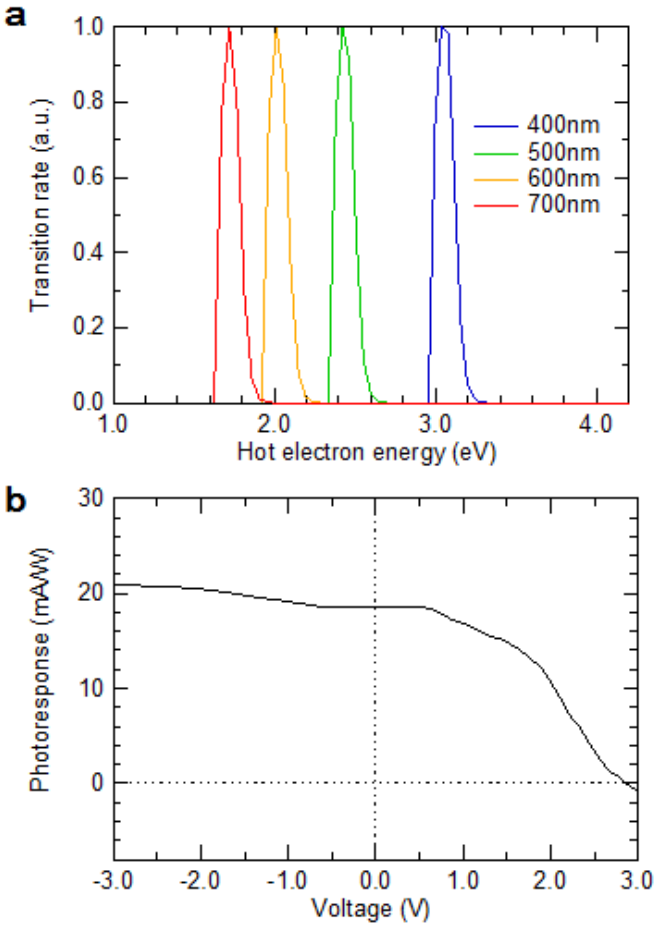


Figure 2.4: Properties and characterization of the hot carrier device with modified EDOS. (a) Transition probability of the hot carriers at different energy levels under illumination at different wavelengths. The transition peak shifts to lower energy as the wavelength increases because the peak distribution required for optimum performance is given approximately by the sum of Fermi level and the photon energy. (b) Photocurrent versus bias voltage under AM1.5G spectral illumination shows improved fill factor resulting from the narrowband energy distribution of hot electrons much above the Fermi level.

| **Wavelength (nm)** | **400** | **500** | **600** | **700** |
|---|---|---|---|---|
| EQE (%) | 11.5 | 9.3 | 2.45 | 1.2 |
| PCE (%) | 10.7 | 8.10 | 2.02 | 0.94 |
| Voc (V) | 3.03 | 2.40 | 1.85 | 1.53 |
| Au absorption (%) | 78.1 | 60.3 | 14.1 | 6.30 |
| ITO absorption (%) | 8.5 | 8.3 | 9.1 | 6.7 |

Table 2.2: Calculated performance of the hot carrier device with a peaked EDOS distribution just below the Fermi energy. EQE, PCE, and $V_{OC}$ represent the external quantum efficiency, power conversion efficiency, and open-circuit voltage of the device, respectively. Higher energy incident photons result in a larger $V_{OC}$ and efficiency. At 400 nm, the PCE reaches 10.7%, which is comparable to that of a typical silicon solar cell with similar illumination.

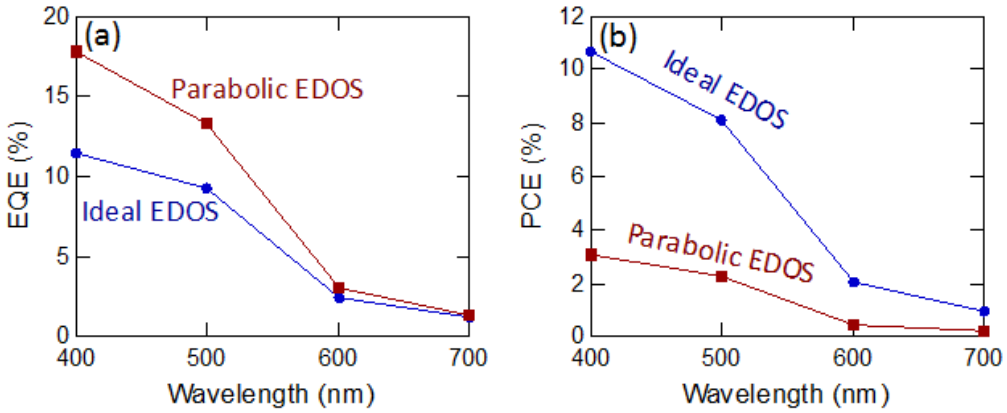


Figure 2.5: Effect of EDOS modification on EQE and PCE. Two models of the electron density of states, EDOS, were used to calculate (a) the external quantum efficiency, EQE, and (b) the power conversion efficiency, PCE. The first model assumes a parabolic EDOS and the second model (denoted Ideal EDOS) assumes a peaked EDOS distribution 0.15 eV below the Fermi level.

2.6(b)), as expected. Further, hot carrier generation is shown to be a single photon-hot carrier interaction by the linearity of the photocurrent with incident light power for both white light and monochromatic light illumination. (Figure 2.6(c), 2.7(c)).

### 2.4.3 Wavelength-Dependent Hot Carrier Generation and Collection

The $I$-$V$ characteristic under monochromatic illumination is determined, showing both voltage independent photoresponse for small bias ($|V| < 0.2\,\mathrm{V}$) and, for larger bias, an open circuit voltage ($\mathrm{V}_{OC}$) that varies with incident photon energy, as expected for an M-I-M hot carrier device (Fig. 2.7(a), 2.7(b)). The experimental photoresponse is found to be in good agreement with the model presented here (Fig. 2.7(b)) throughout the $\pm 0.2\,\mathrm{V}$ bias range. Under larger bias, the measure-

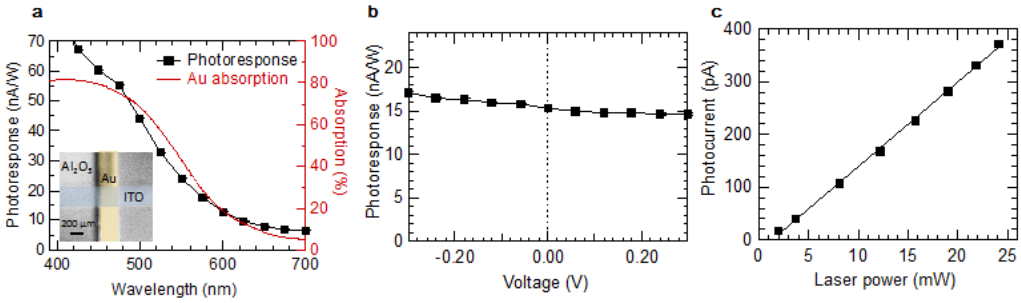


Figure 2.6: Experimental characterization of the hot carrier device. (a) Photoresponse of the device with respect to the incident wavelength. The photoresponse (left axis) mimics the absorption spectrum (right axis), but the peaks occur at different wavelengths due to the internal carrier emission efficiency, which increases as the wavelengths gets shorter. Inset shows the device cross-junction under 5× optical magnification using a monochrome CCD (false colored for clarity). (b) Photoresponse under biased white light illumination. (c) Photocurrent changes linearly with incident white light power, indicating that the hot carrier generation is a linear process.

ments were unstable due to increased noise and electrical device breakdown. When the theoretical model is extended to higher bias, a wavelength dependent $V_{OC}$ is predicated, which is an order of magnitude larger than previous results, suggesting improved application as a wavelength sensitive hot carrier detector [108].

The stable photoresponse under bias variation ($\pm 0.2\,\mathrm{V}$) shows that this device can also be used in situations where the voltage changes due to: (i) variation in potential during operation, (ii) source fluctuations or noise, or (iii) power interruptions. This voltage stability has not been observed in previous M-I-M hot carrier devices.

In order to achieve the idealized photoresponse shown in Figure 2.1(d), several additional considerations need to be made. First, the barrier height $\Phi_B \sim 0.4\,\mathrm{eV}$

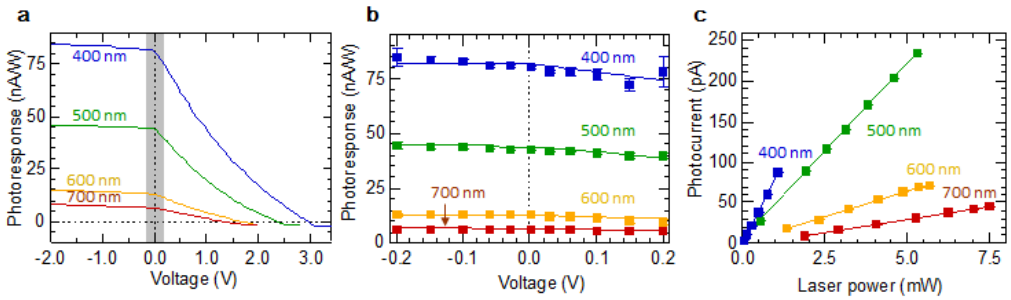


Figure 2.7: Photoresponse under monochromatic light illumination. (a) Calculated photoresponse showing the Voc increase with incident photon energy, as expected for a hot carrier device. (b) Zoom of the photoresponse-voltage relation (between -0.2 V to +0.2 V, shaded region in (a)) of the device under monochromatic illumination (400 nm, 500 nm, 600 nm and 700 nm). Markers represent experimental data, while solid lines represent fits from the hot carrier device model. (c) Photocurrent changes linearly with incident power for each illumination wavelength, further confirming the linearity of hot carrier generation process.

in our simulation is optimized. In reality, the barrier height and the bandgap of the $Al_2O_3$ film strongly depend on the details of the interface, which may vary significantly with the fabrication methods and surface treatment even for similar interfaces [92, 105]. The barrier height extracted from our dark $I$-$V$ measurements by applying the Fowler-Nordheim model [109] is found to be 20 meV (see the following subsection). The much lower barrier height, which probably arises from interface effects such as surface traps, defects and interface dipoles [110–112], dramatically increases thermionic emission from the bottom electrode, reducing the overall current and the ultimate efficiency [92]. Second, surface recombination [110, 111] at the interface on both sides due to trap states would significantly increase the loss of the carriers, which necessitates the incorporation of loss of carriers in the calculation to fit the experimental data (Fig. 2.7(b)). Third, the inelastic scattering with the

Fermi gas could cause additional energy loss of the hot carriers, allowing fewer of them to reach the interface with sufficient energy.

### 2.4.4 Dark Current Measurement and Modeling

The energy barrier height for the excited carriers is determined from the dark current measurement of the M-I-M device based on the Fowler-Nordheim equation [109]. The emission rate of electrons from a metal surface through a barrier is given by:

$$J(V) = \frac{C_1 V^2}{d^2 \Phi_B} \exp\left(\frac{-C_2 \sqrt{m^*/m_0} d \Phi_B^{3/2}}{V}\right) \tag{2.18}$$

where $V$ is the applied voltage, $d$ is the barrier thickness, $\Phi_B$ is the barrier height, $m^*$ is the effective mass of the electrons in the oxide, assumed to be the electron rest mass $m_0$. $C_1$ and $C_2$ are material independent constants given by:

$$C_1 = \frac{2.2q^2}{8\pi h}$$

$$C_2 = \frac{23\pi\sqrt{qm_0}}{6h} \tag{2.19}$$

where $q$ is the electron charge, $m_0$ is the electron rest mass, and $h$ is the Planck constant. Figure 2.8 shows the experimentally measured dark current-voltage relation and the fitted curve based on the above model.

### 2.4.5 Device Dependence on Incident Illumination Angle

The absorption of the device is found to be nearly independent of illumination angle over the entire visible spectrum (Fig. 2.9). This is because the absorption

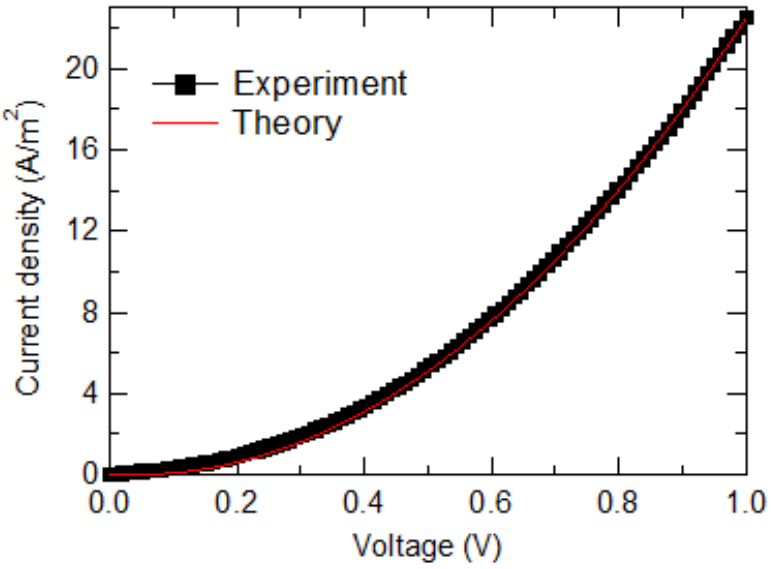


Figure 2.8: Dark current-voltage characteristic for the device. The experimental data is fitted to the Fowler-Nordheim model. The barrier height is found to be 20 meV from this fit.

mechanism does not rely on surface plasmon coupling, which critically depends on the incident angle of illumination. Instead the absorption is determined by the skin-depth the metal. An integrating sphere setup is used to determine the angular dependence of the absorption for each wavelength. Large absorption occurs at short wavelengths, with Au absorbing most of the light. The broad range angular response shows the devices advantage over structures that require additional coupling mechanisms (*e.g.* prism coupling), which depend on illumination angle and wavelength.This angular independence is beneficial for solar illumination because light is incident from all angles throughout the course of a day. This device could also be used under concentrated solar light where sunlight is focused with a lens or mirror. Slight differences between the experimental and simulated results (using

FDTD) are likely due to differences in the optical properties of the ITO between the experiment and the simulation.

## 2.5 Conclusion

In summary, we have demonstrated hot carrier generation and collection in a simple, planar metal-insulator-TCO configuration. The device has an angle-independent response and is shown to function as a wavelength dependent detector in terms of photocurrent and $V_{OC}$ over the entire visible range. Hot carrier generation and collection is verified experimentally under monochromatic and white light illumination, and the device is shown to operate as a photodetector that is insensitive to applied bias over a range of -0.2 V to 0.2 V. As a power conversion device, $V_{OC}$'s in the range of 1.5-3.0 V are expected. Device simulations are in agreement with experimental results and provide a pathway to power conversion efficiencies >10%.

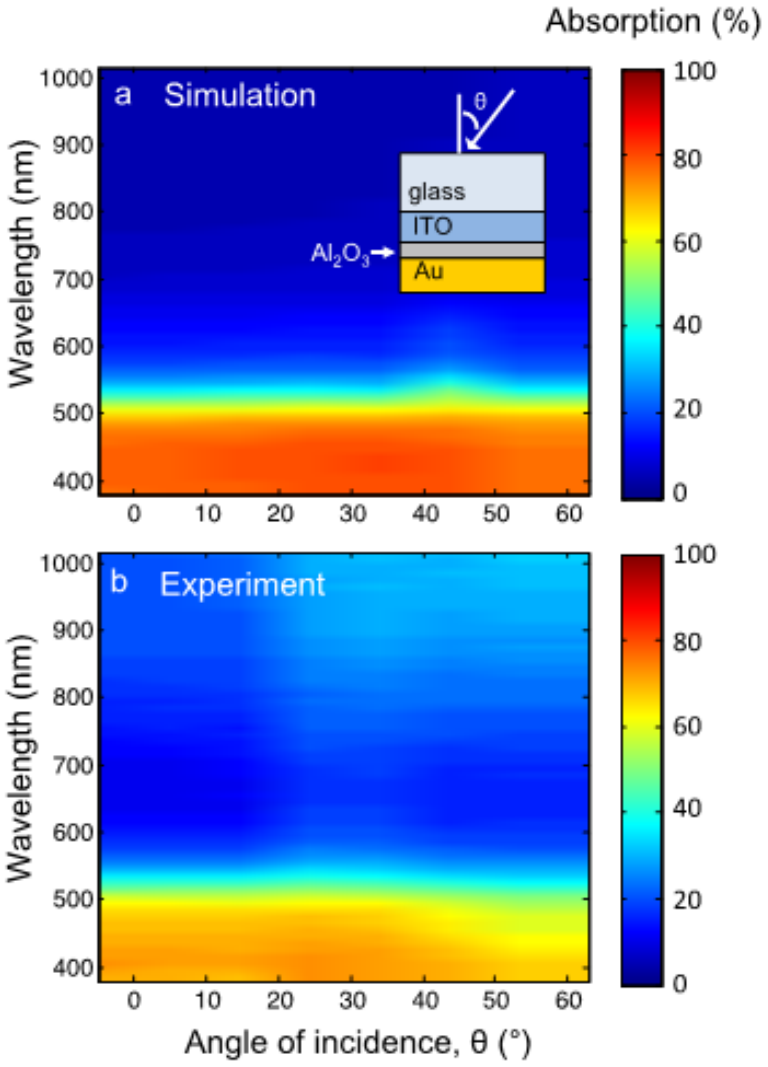


Figure 2.9: Light absorption spectrum of the device for different incident angles. Simulation (a) and experimental results (b) show a nearly angular-independent absorption of the device, indicating omnidirectional photoresponses. The inset shows a schematic of the device under oblique angle illumination.

# Chapter 3: Aluminum Hot Carrier Plasmonics

## 3.1 Overview

Hot carrier effects in metals have recently drawn significant attention due to their potential application as fast, frequency dependent detectors and power converters. Most of the devices, however, have employed noble metals such as gold and silver as the hot carrier generator and emitter and thus have limitations for scalability and device integration with current CMOS fabrication techniques. Here we present an aluminum-based hot electron device and experimentally demonstrate energetic electron generation and collection. The device shows a responsivity of $\sim$240 nA/W for short wavelengths and a clear dependence of the open-circuit voltage on incident photon energy. Furthermore, we show that by coupling to plasmonic modes of a metal-insulator-metal structure composed of a nanowire array adjacent to a thin aluminum film, the light absorption can be increased by a factor of $\sim$3, enabling tunability of the hot carrier response and improved device performance.

Hot carrier-based devices, which take advantage of the excess kinetic energy of carriers (electrons or holes) excited directly from incident photons or by plasmon decay, have been drawing increasing interest over the recent years. They have extensive applications in photodetection [79, 82, 105, 114, 139], photovoltaics [92, 94, 134],

photochemistry [16, 31, 39], hot carrier-induced phase transitions [38], and luminescence [40]. Most of the devices consist of a metal-semiconductor Schottky junction or a metal-insulator-metal junction. Hot carriers are generated in the metal upon excitation and are subsequently injected into the counter-electrode to form the photo-generated current. A nanostructured metal layer is usually employed to couple the incident light into localized surface plasmonic resonances (LSPRs) or surface plasmon polaritons (SPPs), *i.e.* oscillations of free electrons near the metal surface. The surface plasmon effect substantially enhances the field intensity and results in significantly boosted light absorption and hot carrier excitation inside the metal.

From a materials perspective, noble metals such as gold and silver are broadly utilized in plasmonic and hot carrier-based devices due to the efficient surface plasmon coupling at long wavelengths and their stability in air. However, recently aluminum-based plasmonics has become more attractive because of aluminums broadband tunable plasmon response through the entire UV-VIS-NIR spectrum, especially in UV range because of its low loss [15, 65]. Moreover, aluminum is a low-cost, naturally abundant material that can be fabricated on a large-scale with the mature fabrication technology in microelectronics fabrication [10]. Yet, despite the increasing attention to aluminum plasmonics, few papers have explored aluminum-based hot-electron devices. Part of the reason is that aluminum oxidizes quickly upon exposure to air [15, 54], which prohibits the hot electron extraction from inside the aluminum layer.

Here we present a simple device structure in which an Al thin film is employed for generating hot electrons upon photon excitation. The excited hot electrons are

subsequently injected into a counter-electrode made of a transparent conducting oxide (ITO). The two electrodes are separated by an ultra-thin layer of alumina formed by direct native oxidation of the surface of the Al film and subsequent oxygen plasma treatment. The device shows a photoresponse at short wavelength near the UV region, indicating its potential application in short-wavelength photodetection. A shift of open-circuit voltage ($V_{OC}$) with respect to incident photon energy and linearly increased photocurrent with increasing incident power are observed to further confirm the hot electron effect. In addition to these experimental results, we propose a design that can further improve the performance by placing nanowire arrays on top of the Al-insulator-ITO structure, which couples incident light into plasmon modes in the Al film. This design significantly increases the light absorption in the near-IR wavelength regime. The combination of Al plasmonics and hot carrier effects will be advantageous for applications in photodetection, energy harvesting, etc.

## 3.2 Device Fabrication and Experimental Setup

Devices are made via thermal evaporation of a 30 nm Al film on a glass slide through a shadow mask with aligned strips to form the bottom electrodes. The samples are then exposed to air to form a 2∼4 nm native oxide layer (*i.e.* alumina), followed by oxygen plasma treatment under 100 W power and 5 Torr pressure in an oxygen plasma chamber. The ITO counter electrodes are sputtered onto the alumina film forming cross-junctions with the Al strips. Finally, a thin metallic

wire is attached to the Al electrode with Epoxy CW2400 glue.

Optical absorption is measured in a 6 inch Labsphere integrating sphere with a Thermo Oriel Xenon lamp as the light source. For photocurrent measurements, the light source is a Fianium WhiteLase Supercontinuum laser. A SR830 Digital lock-in amplifier, in conjunction with a Keithley 2400 Source Meter, is used for probing the photo-generated current with a bias voltage across the junction.

## 3.3 Results

The schematic of the device junction is shown in Fig. 3.1(a). The incident light illuminates the Al-$Al_2O_3$ interface after passing through the ITO film, because ITO is nearly transparent throughout the visible spectrum. An exponential decay of the electric field at the Al surface leads to strong absorption at the interface and excitation of hot electrons. This exponential absorption profile is beneficial for the subsequent injection of the hot electrons across the oxide barrier, because most of the excited hot electrons are spatially distributed at the Al-$Al_2O_3$ interface and will not lose much energy during the ballistic transport within the carrier mean free path (a few tens of nanometers). The injected hot electrons will be collected by the counter electrode, *i.e.* ITO, forming the photocurrent (Fig. 3.1(b)). The barrier height seen by the hot holes is much larger than that for hot electrons due to the large bandgap (6$\sim$8.3 eV) of $Al_2O_3$ [93]. Therefore, the collected photocurrent is mostly attributed to the unidirectional hot electron flow from Al to ITO. A similar transparent conducting oxide-based structure using gold has been shown

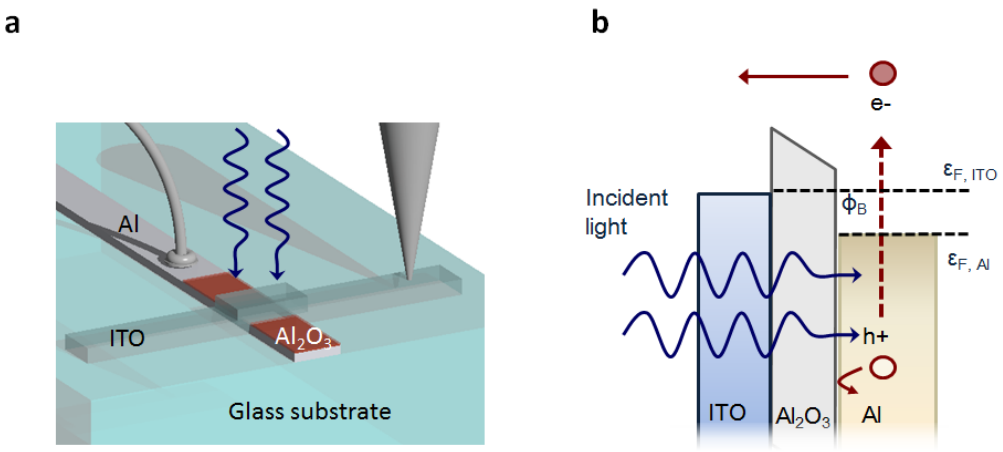


Figure 3.1: Junction structure and its working principle. (a) Schematic of the Al-$Al_2O_3$-ITO junction. Light illuminates the junction through the transparent ITO layer, exciting hot electrons at the Al-$Al_2O_3$ interface. (b) Schematic of the hot electron generation and transport through the oxide barrier.

to outperform the pure metal-insulator-metal (M-I-M) counterpart for the above reasons [92, 139].

Figure 3.2 shows the calculated and experimental absorption spectrum of the device. A finite-difference-time-domain (FDTD) simulation was performed to calculate the light absorption in each layer of the stack at normal incidence, as shown in Fig. 3.2(a). It is the absorption difference between the two electrodes that determines the hot electron injection efficiency. As shown in the inset of Fig. 3.2(a), the absorption difference does not vary much over the visible wavelength range. The total absorption also shows little variation under oblique illumination over a broad range of incident angles (Fig. 3.2(b)). This angular independence is a great advantage for both photodetectors and solar light harvesting, where there is a large

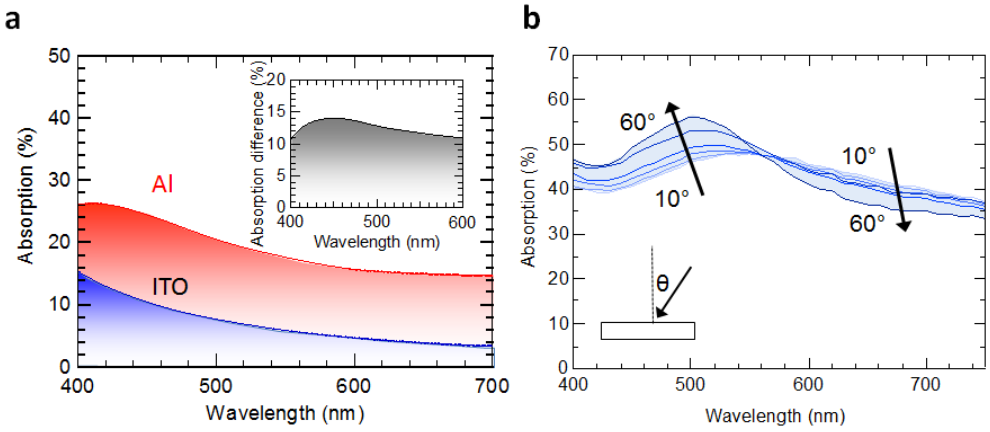


Figure 3.2: Absorption spectrum of the device. (a) Calculated absorption in Al (red) and ITO (blue). Inset shows the absorption difference between Al and ITO does not vary much with wavelength. (b) Experimental total absorption versus wavelength for different incident illumination angles (10° to 60° in 10° steps). The absorption is nearly independent of incident angle.

portion of solar power coming from diffuse light due to the atmospheric scattering.

The generated photocurrent depends not only upon the absorption of light, but also upon the internal injection efficiency of the excited hot electrons. Upon excitation, the hot electrons will redistribute their energy based on their initial energy states in the metal. Recent studies of hot carrier generation in various materials and nanostructures have explored their hot carrier energy redistribution and carrier dynamics [26, 27, 87, 118, 140]. As the hot electrons travel toward the Al-$Al_2O_3$ interface, electron-electron scattering further redistributes their energy and momentum [93, 94], which can reduce their probability of reaching the interface. Upon reaching the interface, the probability of injection through the barrier is mainly dependent on the barrier height and the energy and momentum of the hot electrons

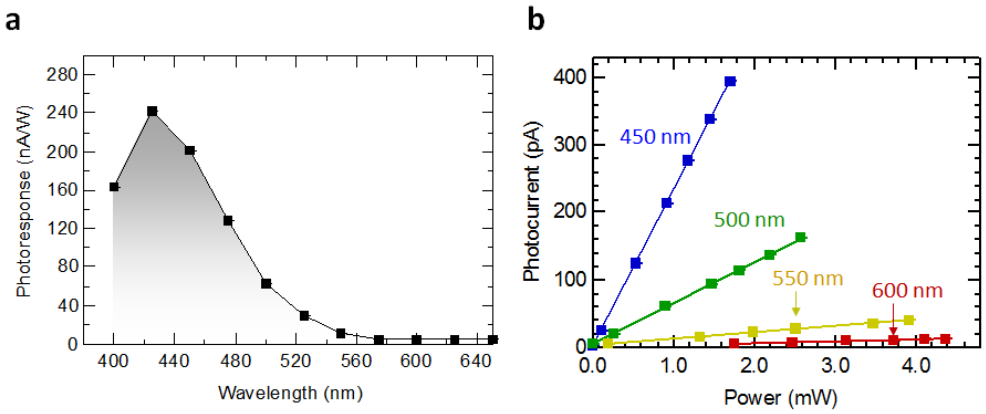


Figure 3.3: Photocurrent changes with wavelength and illumination power. (a) Photoresponse of the device under monochromatic illumination. The device shows much higher response at short wavelengths because more hot electrons are excited to high energy states, which leads to higher injection efficiency. (b) Photocurrent scales linearly with incident light power.

[94, 134]. All of the above effects act together to determine the injection efficiency and the final photoresponse. As shown in Fig. 3.3(a), although the absorption difference does not vary much with the illumination of different energy photons, the photoresponse peaks at short wavelength. This is because hot electrons are promoted to higher energy states when excited by higher energy photons, therefore a larger proportion of them are injected to form the photocurrent. The high sensitivity to short-wavelength incident illumination makes the device an excellent candidate for applications in photodetection. Hot electron generation and extraction is a linear process, *i.e.* one absorbed photon excites only one hot electron. This is confirmed by the linear relation between the photocurrent and the incident light power (Fig. 3.3(b)).

The photoresponse of the device also depends on the bias voltage across it as

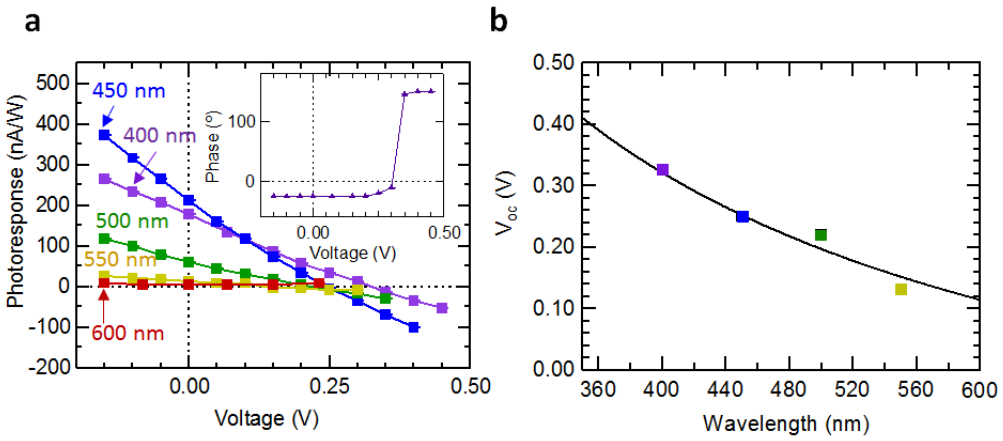


Figure 3.4: Photocurrent-voltage relation. (a) Photoresponse under monochromatic illumination with bias. The open-circuit voltage $V_{OC}$ ranges from 0.10 V to 0.35 V. Inset: The lock-in detector shows a 180° phase change of the measured photocurrent near $V_{OC}$. This behavior indicates that the photocurrent flow is reversed from ITO to Al under bias $>V_{OC}$. (b) $V_{OC}$ varies with incident illumination wavelength. Higher energy photon yields a higher $V_{OC}$, because a larger number of hot electrons with higher energy are injected through the barrier.

a result of the changing barrier height at the Al-$Al_2O_3$ interface under bias (Fig. 3.4(a)). An approximately linear decrease of photocurrent is observed with increasing bias voltage. The linearity indicates a nearly uniform energy distribution of hot electrons above the Fermi energy in Al. This uniform energy distribution has also been demonstrated theoretically [118, 140]. Unlike many noble metals, such as Au and Ag, in which the hot carrier energy distribution has peaks due to d-band transitions, the d-band in Al lies above its Fermi level. This allows for the direct intraband transitions to states with energies ranging continuously from the Fermi level to one photon energy above the Fermi energy [82, 87, 95].

The open-circuit voltage $V_{OC}$, *i.e.* the voltage at which the total photocurrent

reaches zero while the device is illuminated, increases with incident photon energy (Fig. 3.4(b)). This agrees with the approximation [92, 108]:

$$V_{OC} \simeq \frac{E_{ph} - \Phi_B}{e}\left(1 - \frac{I_{SC}^{btm}}{I_{SC}^{top}}\right) \tag{3.1}$$

where $E_{ph}$ is the photon energy, $\Phi_B$ is the barrier height, $I_{SC}^{btm}$ is the short-circuit current from bottom to top (ITO to Al) and $I_{SC}^{top}$ is the short-circuit current from top to bottom (Al to ITO). The barrier height is estimated to be ∼1.5 to 1.6 eV by this equation. The surface quality, which is affected by pinholes, traps, interlayer dipoles, etc., all influence the actual barrier height [112] and is heavily dependent upon the oxide growth and treatment process. A photocurrent phase change of ∼180° is observed in the measurement with a lock-in amplifier. This indicates the photocurrent transitions from positive to negative when the photocurrent from ITO exceeds that from Al (Fig. 3.4(a) inset).

To further enhance the light absorption, and hence the hot electron generation, we propose a device structure where a well-aligned nanowire array is placed on top of the planar Al-$Al_2O_3$-ITO device separated by a 20 nm insulating layer of $Al_2O_3$ (inset in Fig. 3.5(a)). This insulating layer prevents hot electrons from being directly extracted from the nanowires. Light is illuminated from above the nanowire arrays with electric field parallel to the wires (TM polarization). With the nanowire array (diameter 150 nm and period 650 nm) on top, the absorption in Al is significantly enhanced in the near IR region with an absorption peak of ∼70% at wavelength 783 nm (Fig. 3.5(a)), nearly 3 times larger than that of the planar structure (absorption <25%). The enhanced absorption occurs in the Al at the Al-

$Al_2O_3$ interface (Fig. 3.5(b)), which is beneficial for the traversal of the generated hot electrons before losing much energy. To study the cause of the enhancement, a dispersion-relation contour plot (Fig. 3.5(c)) is obtained by plotting the calculated absorption spectrum in the Al film while varying the period of the array. The three branches where the absorption enhancement scales with array period indicates that they are the Bragg-SPP modes, which depends on the diffraction condition imposed by the lattice parameter, *i.e.* the period of the array in our case [53, 115]. The FDTD mode simulation of the SPP modes (white solid lines) agrees well with the absorption enhancement. On the other hand, an absorption enhancement that is nearly independent of the nanowire array period occurs at a wavelength of ∼850 nm. This period-independent absorption indicates a localized plasmon mode of the individual unit cell [115]. However, the most intense absorption (70% at 783 nm) results from the strong interaction between the SPP modes and the localized mode when the two coincide, leading to the hybrid mode (Fig. 3.5(c)) [115]. This hybrid mode boosts the absorption significantly and therefore enhances the hot electron generation. Another advantage of this design is that the resonance intensity and wavelength can be tuned by modifying the coupling of these modes through further optimization of the period and diameter of the nanowires.

## 3.4 Conclusions

In conclusion, we fabricated an aluminum-based hot electron device and demonstrated efficient hot electron excitation and collection in a planar structure. An open-

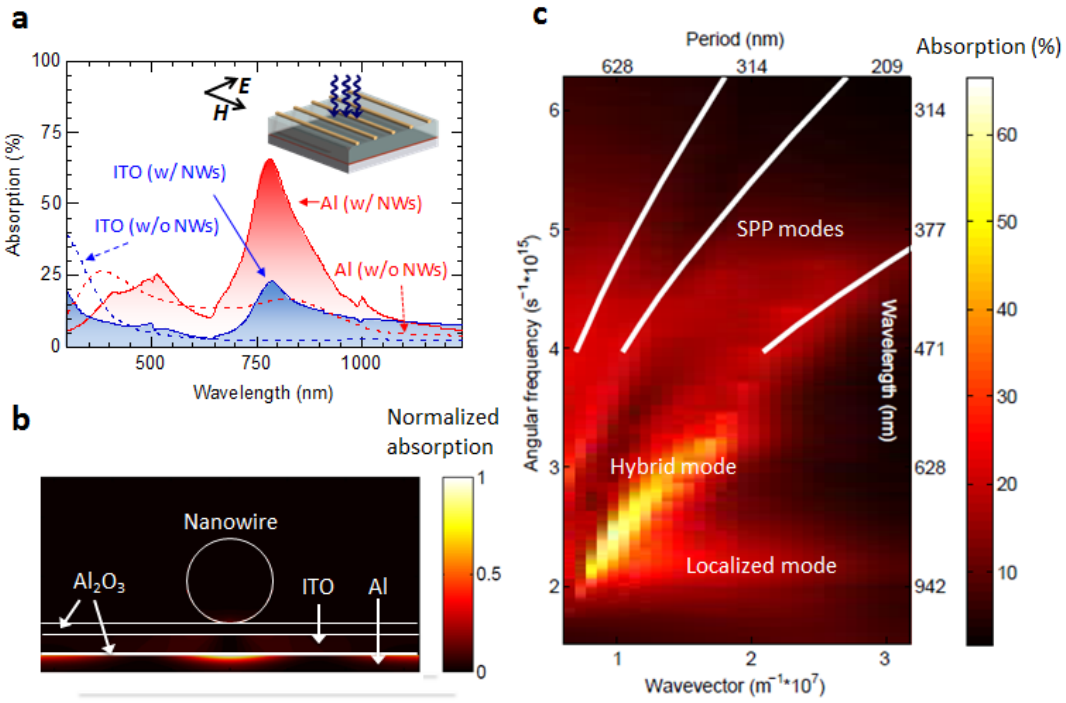


Figure 3.5: Plasmon-induced performance enhancement. (a) Absorption in the Al (red) and ITO (blue) films in the devices with Au nanowires (solid lines) and without Au nanowires (dashed lines). The absorption is boosted at about 783 nm wavelength due to the coupling of incident light into plasmon modes. Inset shows the schematic of the device structure and the incident light polarization. (b) Absorption profile of the device (cross-section). The enhanced absorption is confined in the vicinity of the Al-oxide interface. (c) Absorption contour plot with varying wavelength and nanowire period. The SPP modes (white solid lines) are simulated with the FDTD mode solution. The most intensive absorption occurs where the SPP modes and the localized modes coincide and interact, which results in the hybrid mode.

circuit voltage shift with incident photon energy is also observed. These results are promising for applications of hot electron effects in aluminum for photodetection and photovoltaics. Furthermore, we showed that nanowires can be used to couple the incident light into plasmonic modes leading to strong absorption enhancements, enabling tunability of the resonance throughout the VIS-NIR.

# Chapter 4: Alternative Materials for Hot Carrier Plasmonics

## 4.1 Overview

While the field of plasmonics has grown significantly in recent years, the relatively high losses and limited material choices have remained a challenge for the development of many device concepts. The decay of plasmons into hot carrier excitations is one of the main loss mechanisms; however, this process offers an opportunity for the direct utilization of loss if excited carriers can be collected prior to thermalization. From a materials point-of-view, noble metals (especially gold and silver) are almost exclusively employed in these hot carrier plasmonic devices; nevertheless, many other materials may offer advantages for collecting these hot carriers. In this chapter, we present results for sixteen materials ranging from pure metals and alloys to nanowires and graphene and show their potential applicability for hot carrier excitation and extraction. By considering the expected hot carrier distributions based on the electron density of states for the materials, we predict the preferred hot carrier type for collection and their expected performance under different illumination conditions. By considering materials not traditionally used in plasmonics, we find many promising alternative materials for the emerging field of hot carrier plasmonics.

Hot carrier effects in metals have drawn significant attention recently because of their promising applications in photodetection, energy-harvesting, hot-carrier-induced chemistry, etc. [79, 81, 82, 114]. Hot carrier collection enables utilization of energy that is usually lost in a conventional semiconductor device due to thermalization (*i.e.* phonon generation and heat dissipation resulting from absorption of high energy photons) and sub-bandgap photon loss (*i.e.* lack of absorption of low energy photons). This energy can be extracted through the hot carrier generation in a metal and the subsequent injection of the carrier into a semiconductor (M-S) [80, 81, 83, 84, 115] or a counter-electrode (M-I-M) [92, 105, 139]. In order to achieve high efficiency hot carrier injection, significant light absorption is required in the metal, which is achievable by coupling incident light into surface plasmons (SP)the collective oscillation of free electrons near the metal surface [114, 116, 117]. The improved absorption contributes greatly to the enhancement of hot carrier generation and consequently increases the device efficiency. Therefore, surface plasmons effects are often employed for hot carrier generation.

While most hot carrier devices to-date have used Au or Ag nanostructures, due to their chemical stability and well-studied plasmonic properties, other materials might have potential advantages from the perspective of hot carrier generation following absorption. The hot carrier injection efficiency depends not only on the light absorption, which is made possible by surface plasmon excitation, but also on the hot carrier energy distribution upon excitation, resulting from the decay of the surface plasmons [94, 118]. The hot carrier energy distribution is critical for the collection of carriers because only the hot carriers with sufficiently high energy

and momentum are able to traverse the barrier established at the interface between the metal and the semiconductor or oxide. The hot carrier energy distribution immediately after photon absorption is determined by the initial states of electrons in the Fermi gas and the incident photon energy. Here we present the hot carrier energy distributions in various materials (including metals, alloys, and nanostructures) based on the electron density of states (EDOS) determined by first principle calculations or experiments from the literature. We compare these distributions to the idealized distributions that would optimize the hot carrier injection. These results are meant to outline materials and nanostructures that might be more suitable for hot carrier collection and to provide an alternative perspective on choosing plasmonic materials when the goal is hot carrier generation.

In this chapter we present the hot carrier distributions for electrons and holes in a variety of pure metals (Au, Ag, Cu, Al, Fe, Pt, Ti, and Y), alloys (Ag-Cu, Al-Ga, Au-Pt, and Al-Cu), and nanostructures (Ag and Au nanowires, carbon nanotubes, and graphene). In order to determine the expected hot carrier distributions, we first assume complete absorption within the material through perfect coupling of the incident light into surface plasmons. This assumption serves to eliminate the influence of the optical absorption on the resulting carrier distribution and allows us to focus solely on the influence of the EDOS. Further, nearly perfect absorption has been experimentally achieved in a number of plasmonic and metamaterial structures [81,83,119,120]. Secondly, EDOS data are taken from the literature [121–133]. Combining the EDOS with the Fermi distribution function yields the transition probability and hence the resulting hot carrier distribution. Alternatively, the tran-

sition probability under illumination can be calculated from first principles using Fermis golden rule for the transition, governed by quantum mechanical selection rules. However, the EDOS method turns out to have worked well to describe the performance of previous hot carrier devices [92,105] and will be used here to evaluate the potential of different materials for hot carrier devices.

## 4.2 Simple Models for the Hot Carrier Energy Distribution

The simple model of a metal consists of free electrons moving through a metallic ion lattice, resulting in the well-known parabolic electron density of states (Fig. 4.1(a)), $D(E) \propto \sqrt{E}$, where $D(E)$ is the electron density of states as a function of the electron energy. Upon photon excitation with energy $E_{ph}$, an electron in the Fermi gas is promoted from $E - E_F$ to a higher energy state $E$, where $E_F$ is the Fermi energy. The transition probability is proportional to the multiplication of the joint density of states, which is the product of the densities of states at the initial and final energies, and their respective distribution functions:

$$P(E) \propto D(E - E_{ph}) f(E - E_{ph}) D(E)(1 - f(E)) \tag{4.1}$$

where $f(E)$ is the Fermi distribution function.

Upon monochromatic illumination ($\lambda$=600 nm), a nearly uniform hot carrier distribution is generated based on the parabolic EDOS (Fig. 4.1(b)). This uniform distribution is not ideal for hot carrier collection, because many of the carriers will not have enough energy to overcome the interface barrier, $\Phi_B$. Hence a large fraction of hot carriers with low energy would be lost.

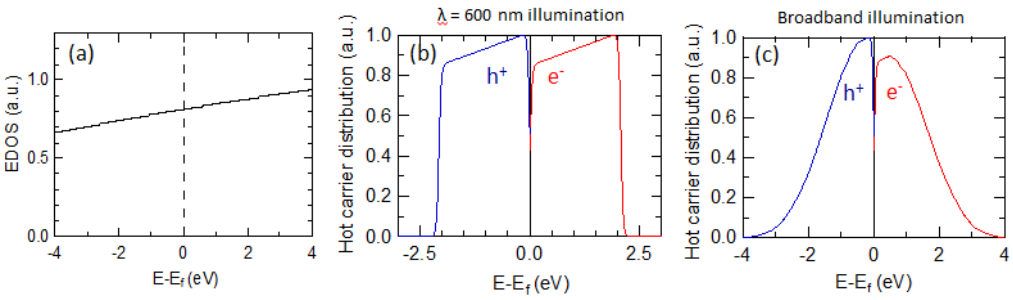


Figure 4.1: Calculations of hot carrier distributions based on the ideal free electron model. (a) Parabolic EDOS as a function of energy (electron energy minus Fermi energy) where EF is ∼11.7 eV for a metal like Al. EDOS is relatively flat for carriers with energies within ±4 eV of the Fermi energy. (b) Hot carrier energy distribution upon excitation by 600 nm illumination (2.07 eV). Nearly uniform distributions for both hot electrons and holes are obtained. (c) Hot carrier energy distribution under broadband illumination (*i.e.* AM1.5G solar spectrum). The distribution is centralized near the Fermi level for both carriers, which is less favorable for hot carrier injection.

Under broadband AM1.5G solar illumination, both the hot electron and hole distributions are concentrated close to the Fermi energy, $E_F$ (Fig. 4.1(c)). The resulting distribution is obtained because all incident photons (regardless of energy) can yield hot carrier distributions near the Fermi energy; however, only high energy photons result in hot carrier distributions far from the Fermi energy. Thus, this distribution profile is even less favorable for hot carrier injection than the distribution yielded by monochromatic light, because a smaller fraction of the carriers have the required high energy needed for injection.

While the parabolic EDOS model is often used to describe an ideal metal, real materials usually do not exhibit the ideal parabolic EDOS behavior owing to band overlapping, various crystallographic orientations, nanoscale confinement, etc. In-

stead, a more complicated EDOS is commonly observed, which may contain peaks in the hot carrier distributions. Because different materials depart from the parabolic EDOS in different ways, it is important to understand how these changes effect the resulting hot carrier distributions.

To improve the hot carrier distributions, we consider a shifted parabolic EDOS model, where a parabolic EDOS is still used; however, the band edge is assumed to be just below the Fermi level ($\sim$0.15 eV below, see Fig. 4.2(a)). This model was first presented to describe experimental photoemission results obtained from thin metallic films on Ge [99] and results in an excited electron energy distribution with a single peak for hot carriers, arising from the excitation of electrons close to the Fermi energy. This model results in a high concentration of Fermi gas electrons within an extremely narrow energy range close to the Fermi level at thermal equilibrium. Thus, the excited hot electrons are also distributed within a narrow energy range (Fig. 4.2(b)). The peaked distribution is beneficial for hot electron injection, provided the barrier height $\Phi_B$ is appropriately chosen for the input illumination spectrum. For example, for $\Phi_B < 3\,\text{eV}$, the hot electrons excited by 400 nm photons will be able to get over the barrier and create photocurrent, as they possess energy greater than 3 eV (Fig. 4.2(b)).

Under broadband AM1.5G illumination, the modified EDOS model also yields a better distribution than the parabolic EDOS. As shown in Fig. 4.2(d), the distribution is more highly weighted towards higher energies rather than centralized near the Fermi level. Moreover, this distribution can be further improved by additional modifications to the EDOS profile. Specifically, it is desirable to have an EDOS in-

crease more steeply as a function of energy. As mentioned in the above analysis, the large concentration of Fermi gas electrons very close to the Fermi level is modeled by an effective conduction band edge just below the Fermi energy; however, the resulting hot electron energy distribution also relies on the density of the unoccupied energy states one photon energy above the Fermi level. Therefore, if the density of the unoccupied states is larger, the final distribution would be pushed further into the higher energy range under broadband illumination. Thus, we consider two additional EDOS models that increase more steeply with energy than the parabolic model ($\sim \sqrt{E}$): $\sim E^2$ and $\sim \exp(E)$. Figure 4.2(c) shows two other EDOS models, both of which yield a narrowband equilibrium electron distribution just below the Fermi level; however, above the Fermi level, the density of vacant states increase faster with energy than $\sim \sqrt{E}$ (*i.e.* as $\sim E^2$ or $\sim \exp(E)$). Though the peaked distributions under monochromatic light illumination for the three models are expected to be similar, the much larger number of vacant states in the latter two models further increases the probability of transitions into higher energy states, pushing the energy distribution of hot electrons further into the higher energy range when under broadband solar illumination (Fig. 4.2(d)). While the above EDOS models have been described for the hot electron distributions, similar expressions hold for hot hole distributions; however, for the ideal hole case, a narrowband of occupied electron states exist below the Fermi level and few vacant states exist above it.

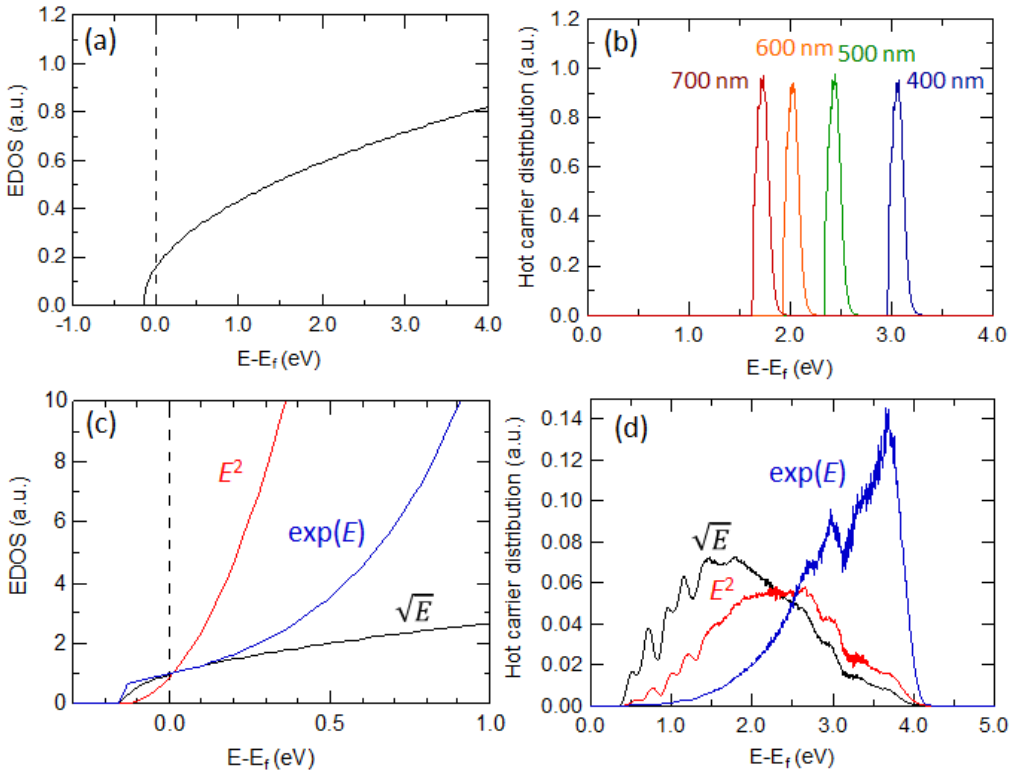


Figure 4.2: Calculation of hot carrier distributions based on the modified EDOS models. (a) Ideal parabolic EDOS with the Fermi level extremely close to the band edge, leaving a large concentration of Fermi gas electrons within a narrow energy range below the Fermi energy. (b) Hot electron energy distribution under illumination by monochromatic light using the EDOS of (a). The hot carrier distribution has a peak that shifts toward higher energy as the energy of the absorbed photon increases. (c) Alternative EDOS distributions yielding higher densities of vacancy states above the Fermi level. Three models (EDOS varies as $\sim \sqrt{E}$, $\sim E^2$, or $\sim \exp(E)$ ) are considered for the modified EDOS. (d) The resulting hot electron distributions under AM1.5G illumination shift toward higher energies for EDOS functions that increase more rapidly with $E$. Distributions with a larger fraction of high energy carriers are more favorable for hot electron extraction under broad-band illumination.

## 4.3 Hot Carrier Distributions in Real Metals

The hot carrier distributions for real metals may vary significantly from the simple models presented in the above section. Metals are the most commonly used materials for exciting surface plasmons to generate hot carriers due to their high free carrier densities, and Ag [121], Al [122], Au [123] and Cu [124] are among the most extensively studied metals for plasmonics. However, with the exception of Al, the EDOS profiles for these metals do not resemble either the ideal parabolic EDOS or any of the modified EDOS. Instead, large numbers of occupied states are found below the Fermi level (Fig. 4.3). The departure of the EDOS from the simple models suggests that the hot carrier distributions generated from photo-excitation may also vary significantly from the idealized models.

The generated hot carrier distribution depends not only on the EDOS, but also on the energy of the incident photons. Usually in a silicon-based M-S hot carrier device, the sub-bandgap photons are in the near-IR range with relatively low energy. As shown in Fig. 4.3(b), the 0.83 eV (1.5 $\mu$m) photons generate both hot electron and hole distributions almost uniformly above and below the Fermi energy. This nearly uniform response is because close to the Fermi level (*i.e.* within one photon energy), the EDOS is relatively flat in these metals. However, a higher photon energy of 1.78 eV (700 nm) yields a different distribution for Au and Cu because the relatively large density of states far below the Fermi energy comes into play, contributing significantly to the electron transition process. For these metals, the large concentration of Fermi gas electrons about one photon energy below the

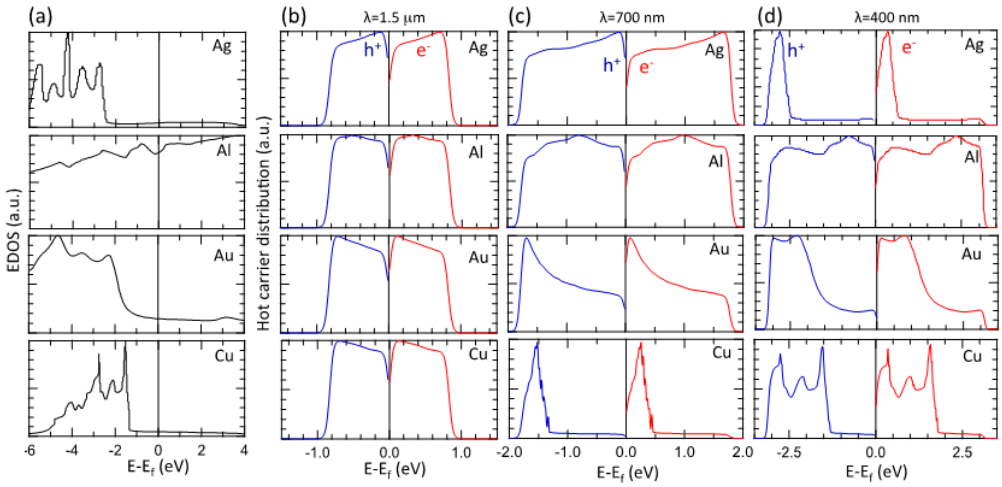


Figure 4.3: EDOS and hot carrier distributions for common plasmonic materials: Ag, Al, Au and Cu. (a) EDOS for these four materials. Except Al, all of these materials exhibit a much higher density of states below the Fermi level. Under monochromatic illumination, hot carrier distributions are created from incident photons with wavelengths: (b) 1.5 $\mu$m (0.83 eV), (c) 700 nm (1.78 eV), and (d) 400 nm (3.11 eV). Low photon energies yield relatively uniform hot carrier distributions for all four metals; however, upon higher energy illumination, peaks begin to appear due to high densities of occupied states below the Fermi level for Ag, Au, and Cu. Under 700 nm illumination Au and Cu are more efficient in hole extraction than electron extraction because the distribution of hot holes is peaked further from the Fermi level.

Fermi level is a result of band overlapping (d-band) [118, 134]. Therefore, a distinct peak occurs in the hot electron distribution just above the Fermi level (Fig. 4.3(c)). Similarly, a peak in the hot carrier distribution also appears in Ag (Fig. 4.3(d)) if the photon energy is much higher (>3 eV), but the 1.78 eV photons do not have enough energy to excite this transition (Fig. 4.3(c)). Al, on the contrary, has an EDOS that is closest to an ideal parabola, resulting in a uniform hot carrier distribution for all wavelengths considered.

Because the EDOS is not symmetric about the Fermi energy for many materials, different materials will perform better for electron or hole extraction. For Au and Cu, the peaks in the hot carrier distributions are much further from the Fermi level for hot holes than for hot electrons. Thus, hot hole extraction is much more favorable because they are more likely to have enough energy to traverse the energy barrier and be collected in the counter-electrode. This observation agrees with the results derived from first principles calculations [118].

Although the above metals are most widely used in plasmonics, they might not be the best for the purpose of hot carrier generation. Here we explore several other metals and demonstrate their potential for hot carrier effects (Fig. 4.4). Included are transition metals and rare-earth metals, which involve more complicated EDOS profiles due to their complex band structures. For Pt [125], due to the large number of occupied states below the Fermi level, the peak for hot holes is still much further from the Fermi level than that for hot electrons, making it better suited for hot hole collection than hot electron collection. For the other metals listed here, a high EDOS appears on both sides of the Fermi level. Ti [126] works fairly well for

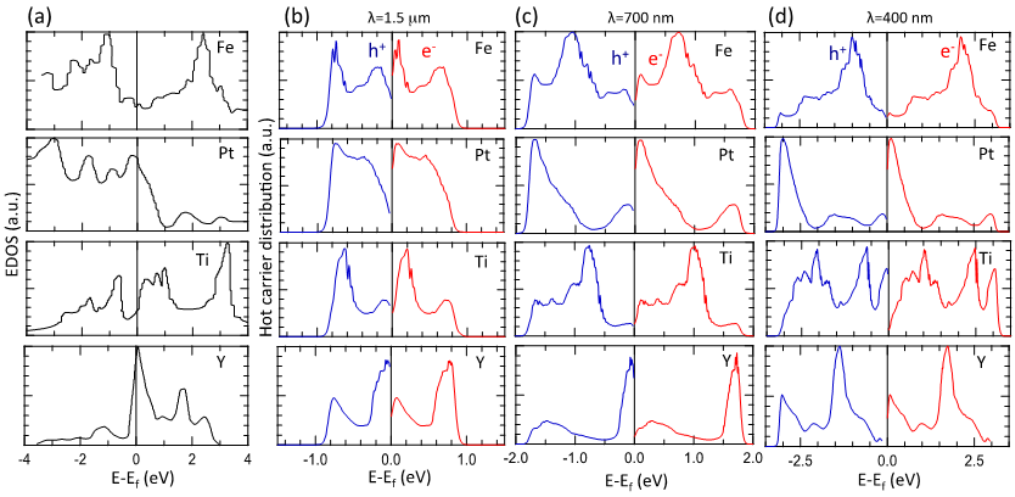


Figure 4.4: EDOS and hot carrier distributions for Fe, Pt, Ti and Y. (a) More complex EDOS profiles are obtained for these metals as a result of their more complicated band structures. Hot carrier distributions are excited by (b) 1.5 $\mu$m (0.83 eV), (c) 700 nm (1.78 eV), and (d) 400 nm (3.11 eV) illumination. More complex patterns in the hot carrier distributions are observed, and the relative positions of peaks (and hence the preferred carrier collection types) depend on the incident photon energy.

both carrier types. Y [127] appears better for hot electron collection under 700 nm illumination but generates similar distributions for hot electrons and holes under 400 nm illumination. A different effect occurs in Fe [122], where hot electrons are more easily collected under 400 nm illumination, but 700 nm illumination favors the hot hole collection. In general, one needs to consider both the EDOS profile and the photon excitation energy to determine which carrier type is most efficiently injected/collected.

## 4.4 Hot Carrier Distributions in Alloys

Unlike pure metals, alloys enable the engineering the EDOS through the control over synthesis conditions. The compositions and crystallographic orientations can be varied, enabling more complexity and tunability than pure metals. Figure 4.5 show the EDOS of an Ag-Cu alloy ($Ag_{27}Cu_7$) [128], which is very different than the EDOS of either Ag or Cu individually (Fig. 4.3). Thus, the hot carrier distributions of the alloy are also significantly different than either of the pure metals. When excited by 700 nm wavelength light, the Ag-Cu alloy better supports hot electron collection because the hot electron distributions peak is further away from the Fermi level. This behavior is in contrast to the uniform hot carrier distribution of Ag or the preferred hot hole collection in Cu at this illumination wavelength. For the Al-Ga alloy (equiatomic composition) [129], the distributions are relatively flat but slightly favor hot hole collection. For Au-Pt alloy (Au atoms sitting in the most stable hollow FCC positions on the Pt (111) lattice) [125], the EDOS is close to the ideally modified profile for holes, where there is high density for occupied states below the Fermi level, but low density for vacant states above the Fermi level. This profile would best facilitate hot hole extraction regardless of the photon energy because the hot hole distribution peak will always be as far as possible from the Fermi energy.

The biggest advantage of using alloys is that it provides tunability of hot carrier generation, so one can engineer the EDOS of an alloy according to ones needs. For instance, in Al-Cu alloy ($AlCu_3$) [130], the occupied states with large density are

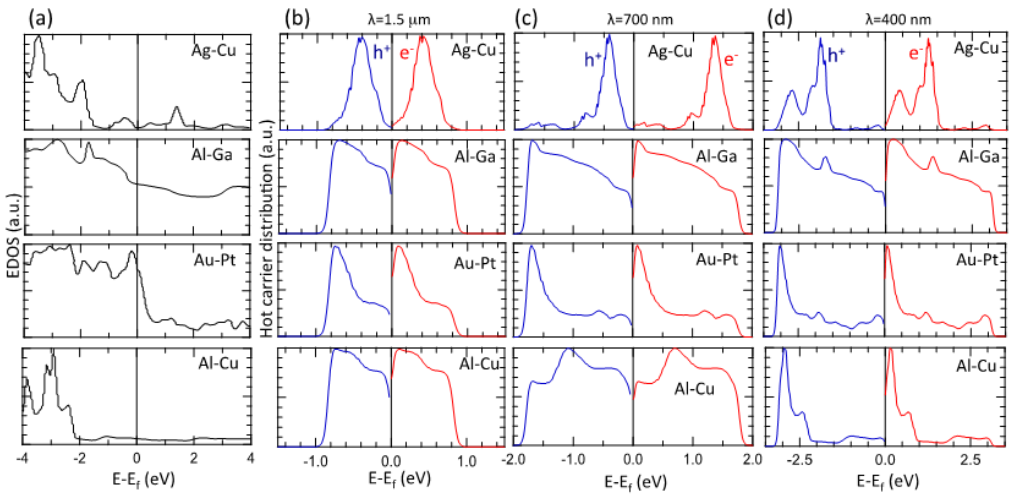


Figure 4.5: EDOS and hot carrier distributions for various alloys. (a) The EDOS of alloys can be engineered so that they differ significantly from their component metals. Hot carrier energy distribution upon excitation by (b) 1.5 $\mu$m, (c) 700 nm, and (d) 400 nm illumination. As in pure metals, the peaks in the distribution vary with both material chose and photon excitation energy. By varying the alloy composition, a range of EDOS possibilities is expected for each of the alloys.

pushed further away from the Fermi level in the EDOS profile compared with the Cu EDOS. Though this distribution is not beneficial for broadband illumination, it favors the hot hole extraction for higher energy photons than Cu, which might prove useful for short wavelength photodetection if the barrier height is appropriately chosen.

## 4.5 Hot Carrier Distributions in Nanostructures

Nanostructure confinement is an alternative approach to modifying the EDOS of a metal. As the dimensions of the structure are reduced to the nanometer scale or even smaller, the electron wavefunctions change dramatically, consequently changing

the EDOS [87]. A recent theoretical work using the kinetic DFT method has also systematically studied the influence of the metal nanocrystal confinement on the plasmonic absorption and hot carrier generation [135]. This effect provides another possibility for tuning hot carrier generation. Figure 4.6 shows the EDOS of Ag and Au nanowires (monoatomic wires anchored on a $MoS_2$ monolayer) [131], which is dramatically different from their bulk counterparts. 700 nm illumination, which yields a uniform hot carrier distribution in Ag, gives rise to distinctive peaks in the distribution of both carrier types for the Ag nanowire, as a result of a new peak induced close to the Fermi level in its EDOS profile. For the Au nanowire, a more complex EDOS is found below the Fermi level resulting in multiple peaks in the hot carrier distribution, for both electrons and holes. Compared to bulk Au, more occupied states exist just below the Fermi level in the nanowire structure, which enables lower energy photons to excite the carriers into the peak distribution. Generally, the nanoscale confined metals behave completely differently than bulk metals in terms of hot carrier generation, and specific designs should be considered independently.

In addition to nanostructured metals, some non-metallic nanostructures could also be a promising option for hot carrier generation. Carbon-nanotubes (CNTs) and graphene have been extensively studied for various applications, and interest has recently emerged in hot carrier effects [136–138]. Through the modification of geometry, dimensions, and doping, CNTs and graphene are able to transform their EDOS profile to a great extent, showing promise for applications in hot carrier generation.

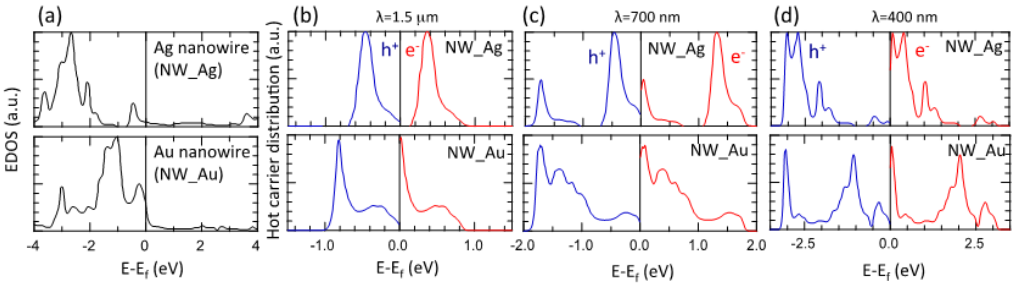


Figure 4.6: EDOS and hot carrier distributions for monoatomic nanowires of Ag and Au. (a) Nanowire EDOS show more complicated behavior than their bulk counterparts. Similarly, the generated hot carrier distributions upon excitation by (b) 1.5 $\mu$m, (c) 700 nm, and (d) 400 nm illumination show multiple peaks instead of a more uniform distribution or a single peak, as is found in the bulk. Generally, nanoscale confined metals have differently hot carrier distributions, and specific designs should be considered for different applications.

As shown in Fig. 4.7(a), the CNTs (zig-zag single-wall CNT (11,0) with a single vacancy) [132] have an EDOS that exhibits a narrowly peaked density of states around the Fermi energy, resulting in one peak in the hot carrier distribution at an energy of 2.49 eV (under 500 nm illumination, Fig. 4.7(d)) and another very close to the Fermi level. Because the central peak concentrates nearly half of the total excited carriers in a very small energy range, this distribution is not as favorable for hot carrier extraction; however, it is still more advantages than a uniform distribution from the perspective of the flexibility of barrier height choice. In this particular case, as long as $\Phi_B < 2.49\,\text{eV}$, the hot carriers in the main peak would all be collected, independent of the barrier height; whereas with a uniform distribution, the barrier height would significantly influence the extraction efficiency. Graphene [133], on the contrary, has almost no states at the Fermi level, but has narrow peaks in the

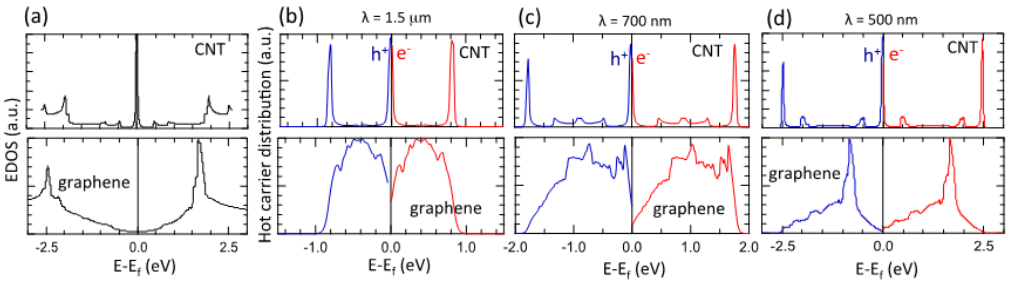


Figure 4.7: EDOS and hot carrier distributions for CNT and graphene. (a) EDOS are nearly symmetric for both materials and have distinctive narrow peaks. Hot carrier energy distribution upon excitation by (b) 1.5 $\mu$m, (c) 700 nm, and (d) 500 nm illumination show narrow peaks, which are favorable for hot carrier injection. We note that the EDOS of CNT and graphene are extremely sensitive to changes in geometry, dimensions, doping, etc., which add additional flexibility to tuning the EDOS profile.

EDOS on both sides of the Fermi level when illuminated at 500 nm. Consequently, a distinct narrow peak distribution is yielded for both hot electrons and holes, which facilitates the extraction of both carriers.

## 4.6 Hot Carrier Distributions Under Broadband Illumination

We have shown hot carrier distributions in various materials and nanostructures under monochromatic illumination. These results are summarized in Table 4.1 for illumination wavelengths of 400 nm, 700 nm, and 1.5 $\mu$m. If both carrier types show a relatively flat distribution, both carrier types are considered suitable for collection. If there are peaks in the distribution, we compare the separation between the main peak and the Fermi level to determine which carrier type is better suited for extraction. Of course, the actual collection efficiencies will also depend upon the

interface barrier height, which depends on the details of the device under consideration. This table is meant to provide rough guidance for the choice of the preferred carrier type for extraction.

Under broadband illumination, the hot carrier distributions are similarly varied depending on the material choice. As indicated in Fig. 4.1(c), the ideal parabolic EDOS model does not yield a preferable distribution because both carriers will be predominantly concentrated near the Fermi level. The modified EDOS models (Fig. 4.2(d)) extend the generated hot electron distributions to a higher energy range due to the concentrated electrons in the Fermi gas close to the Fermi level and large density of vacant states above the Fermi level (or vice versa for hot holes generation). But for real materials, the EDOS is much more complicated. Figure 4.8 demonstrate the hot carrier distributions in several of the materials presented in this manuscript under broadband solar illumination. For Cu, Al-Cu alloy and Au nanowires (Figs. 4.8(a)-4.8(c)), hot electrons are still predominantly generated close to the Fermi level, as in the ideal parabolic EDOS case. However, hot holes are shifted further from the Fermi level, which results from the much larger EDOS below the Fermi level than above the Fermi level. The hot hole collection is hence more favorable in these materials. For Fe and Ag-Cu alloys (Figs. 4.8(d) and 4.8(e)), both carriers spread into the higher energy range due to the relatively symmetric and large EDOS profile about the Fermi level. These materials can thus be utilized equally well for collection of both carrier types. For graphene and Y (Figs. 4.8(f) and 4.8(g)), hot electrons are distributed further from the Fermi level, owing to the larger EDOS above the Fermi level in the two materials, which renders slightly more efficient hot

| Illumination wavelength: | 400 nm | | 700 nm | | 1.5 µm | |
|---|---|---|---|---|---|---|
| **Carriers efficiently collected:** | **Hot electrons** | **Hot holes** | **Hot electrons** | **Hot holes** | **Hot electrons** | **Hot holes** |
| **Pure metals** | | | | | | |
| Ag | | ✓ | ✓ | ✓ | ✓ | ✓ |
| Al | ✓ | ✓ | ✓ | ✓ | ✓ | ✓ |
| Au | | ✓ | | ✓ | ✓ | ✓ |
| Cu | | ✓ | | ✓ | ✓ | ✓ |
| Fe | ✓ | | ✓ | ✓ | ✓ | ✓ |
| Pt | | ✓ | | ✓ | ✓ | ✓ |
| Ti | ✓ | ✓ | ✓ | ✓ | | ✓ |
| Y | ✓ | ✓ | ✓ | | ✓ | |
| **Alloys** | | | | | | |
| Ag-Cu | | ✓ | ✓ | | ✓ | ✓ |
| Al-Ga | ✓ | ✓ | ✓ | ✓ | ✓ | ✓ |
| Au-Pt | | ✓ | | ✓ | | ✓ |
| Al-Cu | | ✓ | ✓ | ✓ | ✓ | ✓ |
| **Nanostructures** | | | | | | |
| Ag nanowire | | ✓ | ✓ | | ✓ | ✓ |
| Au nanowire | ✓ | ✓ | | ✓ | | ✓ |
| CNT | ✓ | ✓ | ✓ | ✓ | ✓ | ✓ |
| Graphene | ✓ | ✓ | ✓ | ✓ | ✓ | ✓ |

Table 4.1: Summary of expected hot carrier collection efficiencies for electrons and holes under illumination (400 nm, 700 nm, or 1.5 $\mu$m) for the materials considered in this chapter. Checkmarks suggest, as a rough guide, that a particular carrier type is preferred for collection. If both electrons and holes have a checkmark, both carrier types are expected to be collected. The actual collection efficiencies will also depend upon the interface barrier height, which depends on the details of the device under consideration.

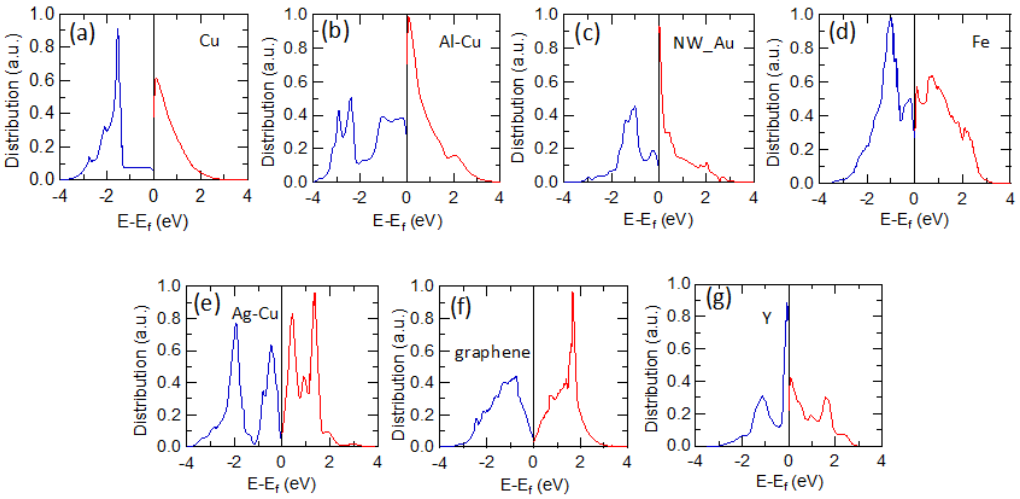


Figure 4.8: Hot carrier distributions for different materials under AM1.5G illumination. In (a), (b) and (c), hot holes distributions are weighted further from the Fermi level, indicating suitability for hot hole extraction. In (d) and (e), comparable distributions for both carriers are found. In (f) and (g), hot electrons are slightly preferred due to an overall larger fraction of excited electrons further from the Fermi level.

electron extraction.

## 4.7 Conclusions

In conclusion, we have described a variety of alternative materials that can be used in hot carrier plasmonics. We have calculated the excited hot carrier energy distributions for a variety of materials and nanostructures based on their EDOS and have compared these results with simplified cases that are commonly used in the literature. We have shown preferred hot carrier extraction for electrons or holes depends on the chosen material and illumination wavelength. As expected, these materials have demonstrated great variability in their hot carrier generation profiles,

showing the usefulness of different materials for specific applications. The design principles for hot carrier plasmonics are indeed different from those in traditional plasmonics and alternative material choices will be important as the field progresses.

# Chapter 5: Theory of Sub-Bandgap Enhanced Solar Cell

## 5.1 Overview

The maximum solar power conversion efficiency of a *p*-*n* junction device was first derived by Shockley and Queisser (SQ) using the principle of detailed balance [143]. This model is now considered the standard by which new photovoltaic technologies are compared. To surpass this limit, various attempts have been suggested including: semiconductor hot carrier extraction [76–78], carrier multiplication [70, 72, 74, 144], the addition of an intermediate band within the semiconductor bandgap [145, 146], thermophotonic up-conversion [147], and the use of multi-junction configurations [67, 69, 148]. These concepts are often referred to as the third-generation photovoltaics [149]. While multi-junction solar cells have surpassed the efficiency of single-junction devices, they require the union of different semiconductor materials that must be lattice-matched, strain-compensated, or formed into multiple adjacent devices (*e.g.* using spectrum splitting concepts) [68]. All other third-generation devices have been confined to efficiencies well below the single-junction limit based on real-world difficulties that are unique to each technology. Here we present an alternative approach that is able to beat the SQ limit by employing a photon-absorbing Ohmic back contact in a conventional *p*-*n* junction solar

cell. This device configuration enables sub-bandgap photon absorption in the back contact and the subsequent hot electron injection into the $p$-$n$ junction, resulting in additional photocurrent in excess of that generated solely through the above-bandgap photon absorption in the $p$-$n$ junction, enabling a new third-generation technology.

The hot carrier injection solar cell can be described in terms of a traditional solar cell with an absorbing Ohmic back contact. The absorbing contact serves to provide additional photocurrent by absorbing the sub-bandgap photons and subsequently exciting and injecting hot electrons into the semiconductor. The band diagrams for a conventional $p$-$n$ junction solar cell and the proposed hot carrier injection solar cell are shown in Fig. 5.1. In the ideal, conventional $p$-$n$ junction cell (Fig. 5.1(a)), the Ohmic back contact is a perfect reflector for all photons and merely collects carriers generated within the semiconductor. However, for the hot carrier injection cell (Fig. 5.1(b)), a photon-absorbing Ohmic contact, which is nanostructured appropriately and rendered highly absorptive [83–85, 119, 150], is attached to the $p$-region. This nanostructured metal layer absorbs sub-bandgap photons and excites hot carriers (both electrons and holes). The barrier height $\Phi_B$ for the hot electrons at the interface depends on the details of the device (*e.g.* the metal work function, p-region doping, surface preparation and treatment, etc [112, 151, 152]), but can simply be treated as an additional optimization parameter when determining the maximum efficiency of the device, as discussed below. A fraction of the hot electrons will be injected from the back contact, and therefore result in the generation of additional carriers in the semiconductor.

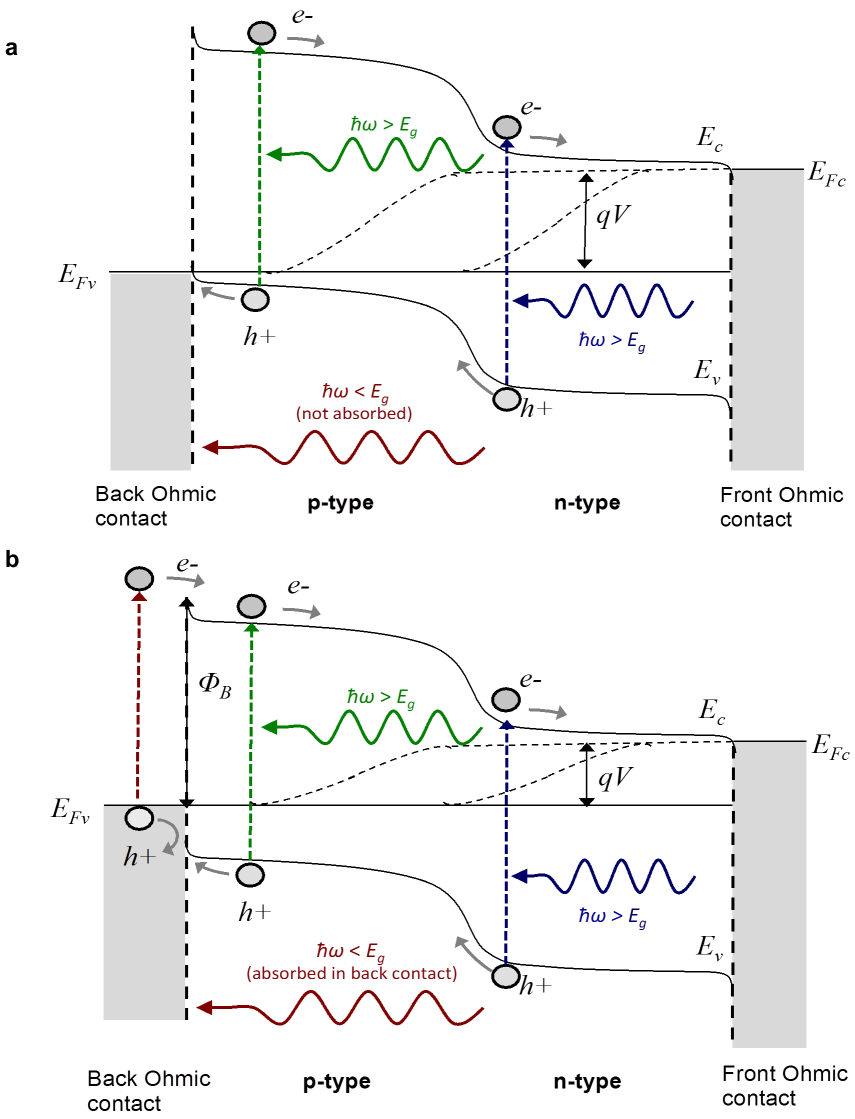


Figure 5.1: Energy band diagrams. (a) A conventional single-junction cell and (b) the hot carrier injection cell. In the semiconductor region of the hot carrier injection cell, all above-bandgap photons are absorbed and generate a single electron-hole pair per photon. In the back metal Ohmic contact, all sub-bandgap photons are absorbed and excite hot electrons. A fraction of them are injected into the semiconductor, providing additional current to the $p$-$n$ junction. The resultant device efficiency depends on both the semiconductor energy bandgap, $E_g$, and the barrier height for the hot electron injection, $\Phi_B$.

The SQ limit depends solely on the semiconductor bandgap, $E_g$ , which determines the absorbed and emitted photon fluxes, and not on the specific doping concentrations, *i.e.* it does not depend on the actual band diagram. Similarly, the limiting efficiency of the hot carrier injection device can be determined as a function of the semiconductor bandgap; however, the barrier height $\Phi_B$ is an additional parameter that limits both the hot carrier injection current and the maximum operating voltage. The operating voltage is constrained because if the bias is too large ($V > \Phi_B/q$), the band bending is reversed and the generated carriers cannot be collected (note: the carrier mobility is assumed be to infinitely large, and a tiny reverse field would block the carriers). Therefore, in the following model for the hot carrier injection solar cell, the method of detailed balance is used, which not only takes into account the photon fluxes based on the semiconductor bandgap, but also the effect of the barrier height. The resulting model is then compared the SQ limit and is shown to exceed it for appropriate values of the $\Phi_B$.

## 5.2 Theoretical Model

As in the SQ model, the maximum conversion efficiency is achieved under several assumptions. First, all above-bandgap photons are absorbed within the semiconductor and generate electron-hole pairs; whereas all sub-bandgap photons are absorbed within the nanostructured Ohmic back contact and excite hot carriers (hot electrons and holes). Second, we assume high-quality materials with no non-radiative recombination within the semiconductor. Third, carrier mobility is

infinitely large. This assumption enables perfect collection of the photo-generated carriers (*i.e.* internal quantum efficiency is unity), because the internal electric field will cause the generated electrons and holes to be separated and collected at the appropriate contacts before they recombine (Fig. 5.1). Fourth, an ordinary Ohmic front contact is applied on the n-side with the Fermi level very close the conduction bandedge, so that the generated electrons are collected without further energy loss. Fifth, a fraction of the generated hot electrons at the back contact will traverse the barrier and be injected into the semiconductor; thereafter, the hot electrons thermally relax down to the conduction bandedge in the same way as the above-bandgap photon-generated electrons in the semiconductor. In other words, the excited hot electrons in the metal are cooled after injection into the semiconductor. From this perspective, the photo-generated electrons in the semiconductor and the injected electrons are treated similarly in terms of their contribution to photocurrent and to Fermi-level splitting. Similarly, any generated hot holes that are injected into the semiconductor will cool and be swept toward the back contact due to the internal field, analogous to the holes generated by the above-bandgap photons. However, if the Fermi-level splitting (or the applied operating bias voltage) exceeds the barrier height $\Phi_B$, the generated carriers cannot be collected due to the inversion of the internal field.

To determine the photon fluxes, we use the method of detailed balance [143, 153]. The absorption and emission fluxes of photons can be written in terms of the

generalized Planck expression [154]:

$$N(T,V,E_{min},E_{max},\theta_{max}) = 2\pi \int_0^{\theta_{max}} \sin\theta\cos\theta \mathrm{d}\theta \int_{E_{min}}^{E_{max}} \frac{2}{h^3c^2} \frac{E_{ph}^2}{\exp\left(\frac{E_{ph}-qV}{kT}\right)-1} \mathrm{d}E_{ph} \tag{5.1}$$

The semiconductor absorbs all above-bandgap photons from the sun, and the number of photons absorbed per unit area and time is denoted as $N_{abs}^{pn}(T_s) = N(T = T_s, V = 0, E_{min} = E_g, E_{max} = \infty, \theta_{max} = \theta_s)$, where we have treated the sun as a blackbody with temperature $T_s = 5760\,\mathrm{K}$ incident from a half angle of $\theta_s = 0.267°$. The absorbed photons generate electron-hole pairs to be extracted as photocurrent $J_L^{pn} = qN_{abs}^{pn}(T_s)$. Meanwhile, the metal absorbs all sub-bandgap photons from the sun, given by $N_{abs}^{m}(T_s) = N(T = T_s, V = 0, E_{min} = 0, E_{max} = E_g, \theta_{max} = \theta_s)$, and hot electrons are excited. However, only a fraction of these hot electrons will have sufficient energy and momentum to traverse the barrier and eventually form the photocurrent $J_L^{m} = PqN_{abs}^{m}(T_s)$, where $P$ is the fraction of the total excited hot electrons that traverse the barrier. $(1-P)$ of the generated hot electrons are not injected and eventually thermalize with the Fermi gas through electron-electron interaction and electron-phonon interaction [76, 87, 94]. This unavoidable non-radiative loss in the metal is given by $N_{non-rad}^{m} = (1-P)N_{abs}^{m}(T_s)$. In addition, both the semiconductor and metal absorb light from the ambient surroundings at temperature $T_c = 300\,\mathrm{K}$, represented by $N_{abs}^{pn}(T_c) = N(T = T_c, V = 0, E_{min} = E_g, E_{max} = \infty, \theta_{max} = \pi/2)$ and $N_{abs}^{m}(T_c) = N(T = T_c, V = 0, E_{min} = 0, E_{max} = E_g, \theta_{max} = \pi/2)$, respectively. As a consequence, the total incoming absorbed photon flux is:

$$N_{in} = N_{abs}^{pn}(T_s) + N_{abs}^{m}(T_s) + N_{abs}^{pn}(T_c) + N_{abs}^{m}(T_c) \tag{5.2}$$

Next, we consider the photon flux emitted from the cell. The semiconductor emits above-bandgap photons as a blackbody with temperature $T_c$, given by $N^{pn}_{emit}(T_c, V) = N(T = T_c, V, E_{min} = E_g, E_{max} = \infty, \theta_{max} = \pi/2)$; whereas the photon emission from the metal is given by $N^{m}_{emit}(T_c) = N(T = T_c, V = 0, E_{min} = 0, E_{max} = E_g, \theta_{max} = \pi/2)$. Note that the metal temperature is still assumed to be $T_c$, because the generated hot carriers are injected into the semiconductor before they begin to cool. Further, the given expression for $N^{m}_{emit}(T_c)$ is only valid when the voltage across the metal-semiconductor interface approaches zero, which is true for this device structure because we are considering an Ohmic contact and the entire applied voltage drop occurs across the semiconductor region. Thus, the total outgoing photon flux is:

$$N_{out} = N^{pn}_{emit}(T_c, V) + N^{m}_{emit}(T_c) \tag{5.3}$$

The difference between absorbed and emitted photon fluxes contains two terms: the non-radiative loss $N^{m}_{non-rad}$ mentioned above and the total extracted current density $J(V)$ when the device is connected to an external load, yielding:

$$N_{in} - N_{out} = N^{m}_{non-rad} + \frac{J(V)}{q} \tag{5.4}$$

By substituting Eq. (5.2) and Eq. (5.3) into Eq. (5.4), we obtain the current-voltage relation:

$$J(V) = J^{pn}_{L} + J^{m}_{L} + qN^{pn}_{emit}(T_c, 0) - qN^{pn}_{emit}(T_c, V) \tag{5.5}$$

Compared to the current-voltage relation of a conventional $p$-$n$ junction cell, Eq. (5.5) contains only one additional term, $J^{m}_{L}$, resulting from the additional hot electron injection.

Because we have used a detailed balance model for determining the maximum power conversion efficiency, the above calculations are agnostic to the specific device parameters (doping concentration, junction depth, etc.); however, a device model can also be used if photon recycling effects are included [153]. Both models yield the same dark current when the minority carrier lifetimes, $\tau_e$ and $\tau_h$ for electrons and holes respectively, are related to the radiative recombination constant, $B$, (from the detailed balance model) by:

$$\tau_e = \frac{1}{BN_A}$$
$$\tau_h = \frac{1}{BN_D} \tag{5.6}$$

where $N_A$ and $N_D$ are the doping concentrations in the $p$-region and $n$-region, respectively. Therefore, to avoid loss of generality, we use the detailed balance model to calculate the dark current within the semiconductor (rather than device specific parameters), which depends on $E_g$. Similarly, the barrier height for hot carrier injection can also be determined in terms of the doping concentration and the work function of the metal contact; however, to avoid the need to specify particular material choices, we use the parameter $\Phi_B$ to describe the barrier height at the contact. These considerations allow for the determination of the device efficiency based on two parameters, $E_g$ and $\Phi_B$, and the assumption listed above.

## 5.3 Maximum Power Conversion Efficiency

To evaluate the performance of an ideal hot carrier injection solar cell, we need the current supplied by hot carrier injection, *i.e.* $J_L^m$. Upon photo-excitation,

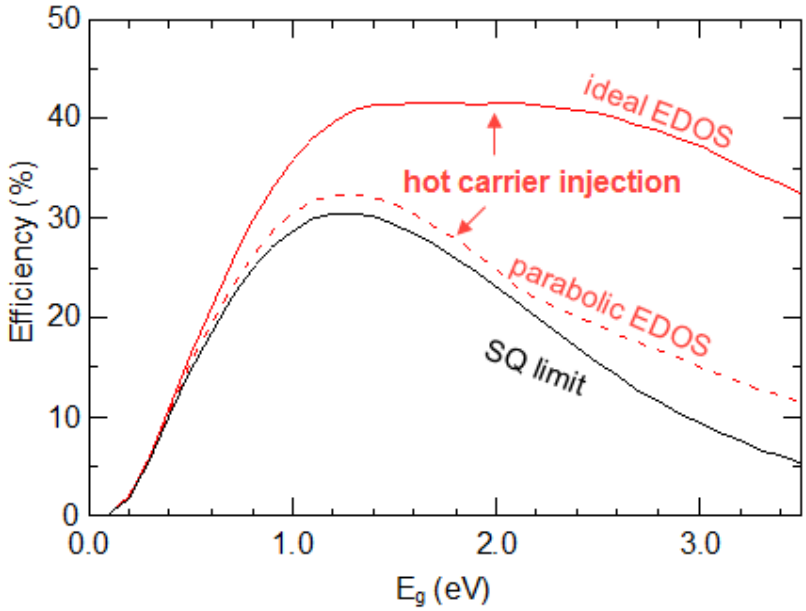


Figure 5.2: Efficiency limit for the hot electron injection device. The optimized efficiency of the hot carrier injection solar cell surpasses the Shockley-Queisser limit under 1-sun spectral illumination for all semiconductor bandgap energies, $E_g$, for both the parabolic EDOS model (red dashed line) and the ideally modified EDOS model (red solid line). For a given energy bandgap, the efficiency improvement is a result of the increased short-circuit current density $J_{SC}$ due to the hot electron injection. The ideal EDOS model yields the largest enhancement, resulting from the injection of hot electrons from a narrowband energy distribution.

the hot electrons attain an energy distribution determined by the band structure of the metal. A simple assumption of free electrons in the metal would yield a parabolic electron density of states (EDOS), $\rho \propto \sqrt{E}$. However, in real materials, the EDOS usually exhibits multiple peaks [94, 95, 99, 118, 140] due to overlapping bands, nanostructure confinement, and various crystallographic orientations. In our calculations, we consider two models for the EDOS: a simple parabolic model and a modified model where the effective conduction band edge is very close to the Fermi level so that hot electrons are promoted to a narrow energy range, enabling a nearly ideal EDOS for hot carrier injection [94, 99, 139, 155]. This distribution is represented by the electron distribution joint density of states (EDJDOS) [94]: $D(E, E_{ph}) = \rho(E - E_{ph})\rho(E)$, where $E$ is the energy of the generated hot electron and $E_{ph}$ is the absorbed photon energy. The energy distribution of the hot electrons reaching the interface can deviate from the initial distribution due to electron-electron collisions (300∼500 fs) and thermal relaxation (∼1 ps) during the transport [119, 154]. However, if the metal layer is sufficiently thin compared to the mean free path (MFP), $l_e \sim$ 30-50 nm [92, 93], the energy distribution will not be changed significantly.

The probability of injection through the barrier depends on both the energy and momentum of the hot electron at the interface. Only when the momentum normal to the interface is sufficiently large will the hot electron be able to directly traverse the barrier. This restriction defines an injection cone of the hot electron with a given energy [79, 94, 134]. However, if the metal layer is extremely thin, the hot electrons will experience multiple reflections and ultimately be brought back to

the interface with its momentum re-directed (minimizing the effect of the injection cone), thus increasing the injection probability [96,99,134,156]. In the ideal case, the traversing probability reaches unity as long as $E > \Phi_B$. Therefore the probability of injection under illumination with photons of energy $E_{ph}$ is:

$$p(E_{ph}) = \frac{\int_{\Phi_B}^{E_{ph}} D(E, E_{ph}) \mathrm{d}E}{\int_{0}^{E_{ph}} D(E, E_{ph}) \mathrm{d}E} \tag{5.7}$$

Because the hot electron injection current depends on the incident photon energy, the total hot electron injection current is:

$$J_L^m = \int_0^{E_g} p(E_{ph}) n_{abs}^m(T_s, E_{ph}) \mathrm{d}E_{ph} \tag{5.8}$$

where $n_{abs}^m(T_s, E_{ph})$ is the absorbed photon flux per unit energy,

$$n_{abs}^m(T_s, E_{ph}) = 2\pi \int_0^{\theta_s} \sin\theta \cos\theta \mathrm{d}\theta \frac{2}{h^3 c^2} \frac{E_{ph}^2}{\exp\left(\frac{E_{ph}}{kT}\right) - 1} \tag{5.9}$$

Using the method described above (from the current-voltage characteristic of Eq. (5.5)), we find that the limiting power conversion efficiency (PCE) using hot carrier injection exceeds the single-junction SQ limit (∼30.4%). Figure 5.2 shows the limiting efficiency assuming either (i) a parabolic EDOS or (ii) the nearly ideal EDOS model under 1-sun blackbody spectral illumination. For the parabolic and modified EDOS cases, the maximum PCE reaches 32.4% and 41.5%, respectively. The decrease in efficiency for higher bandgap materials is because the barrier height is constrained to $\Phi_B \geq E_g/2$ due to Fermi-level alignment at the metal and $p$-region interface, and so the optimal barrier height of $\Phi_B \simeq 1.1\,\mathrm{eV}$ (see discussion below) is not reached for higher bandgap materials ($E_g > 2.2\,\mathrm{eV}$).

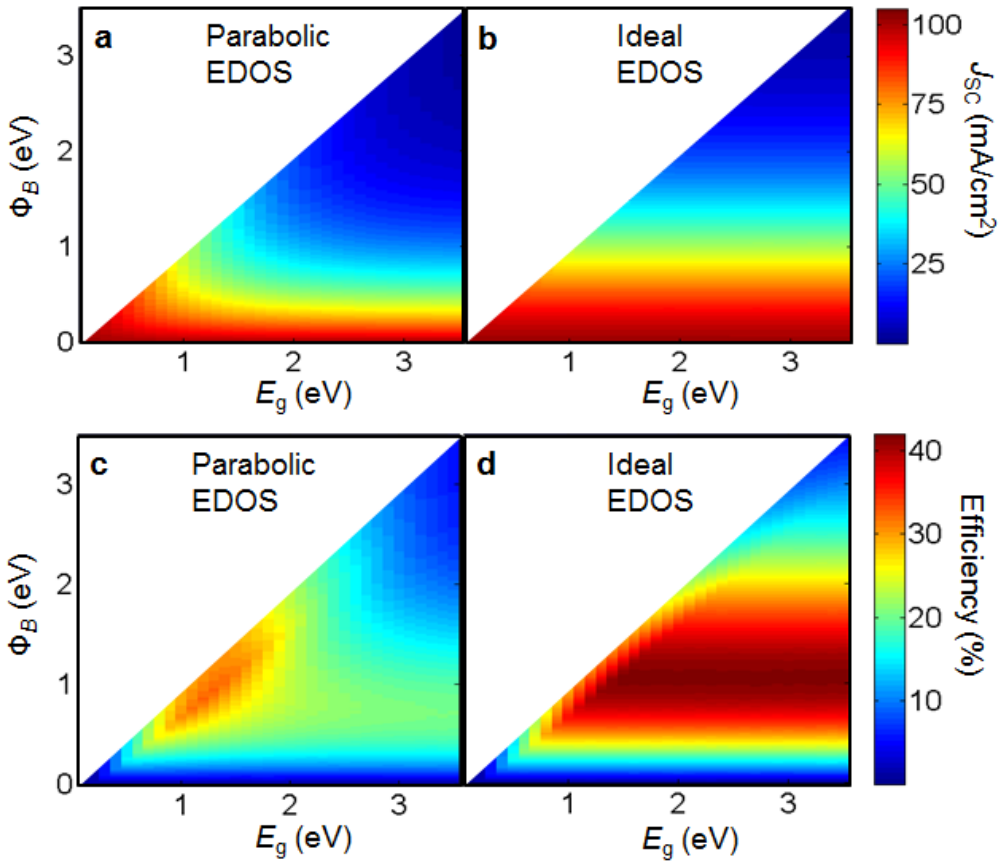


Figure 5.3: Optimization of the short-circuit current density and efficiency of the hot carrier injection device for different parameters. The short-circuit current density $J_{SC}$ and efficiency of the hot carrier injection solar cell depend on the barrier height $\Phi_B$ and the bandgap $E_g$. Contour plots of $J_{SC}$ for (a) the parabolic EDOS model and (b) the ideal EDOS model. Contour plots of efficiency for (c) the parabolic EDOS model and (d) the ideal EDOS model. The efficiency is proportional to the product of $J_{SC}$ and $\Phi_B$, because $\Phi_B$ limits the operating voltage.

Figure 5.3 shows the dependence of the short-circuit current density $J_{SC}$ and the power conversion efficiency on $\Phi_B$ and $E_g$. Figure 5.3(a) and 5.3(b) indicate that for a given bandgap energy $E_g$, the current density $J_{SC}$ decreases as the barrier height $\Phi_B$ increases because of the reduced hot electron injection. For the ideal EDOS (Fig. 5.3(b)), $J_{SC}$ is nearly independent of $E_g$ and only depends on $\Phi_B$, which determines the minimum energy for photocurrent generation (due to absorption in both the metal contact and the semiconductor). The efficiency of the device is proportional to both $J_{SC}$ and $\Phi_B$, because $\Phi_B$ limits the operating voltage, as discussed above. Using Eq. (5.5), the maximum efficiency for the ideal EDOS model is found to occur at $\Phi_B \simeq 1.1\,\mathrm{eV}$ regardless of $E_g$, for $E_g > 1.4\,\mathrm{eV}$.

Compared to a single-junction cell that has the same semiconductor bandgap, the hot carrier injection cell leads to a higher efficiency as a result of increased current with minimal voltage loss. The total current of the hot carrier cell is larger due to the additional carrier injection, but the operating voltage is limited by $\Phi_B/q$; whereas for the single-junction cell, its operating voltage is limited by $E_g$ (*i.e.* it must be less than the open-circuit voltage [42, 157], $\sim \frac{E_g}{q} - 0.28\,\mathrm{V}$) rather than $\Phi_B$. However, the optimized efficiency of the hot carrier cell is higher because the enhancement in current outweighs the loss of operating voltage.

Figure 4 shows a comparison of the performances between the hot carrier injection cell and the other third-generation cells under 1-sun blackbody spectral illumination. The efficiency of the hot carrier injection cell is comparable to the intermediate-band (IB) cell, but has an advantage over all other cells for higher bandgap materials ($E_g \geq 1.8\,\mathrm{eV}$), which could open the door to alternative semi-

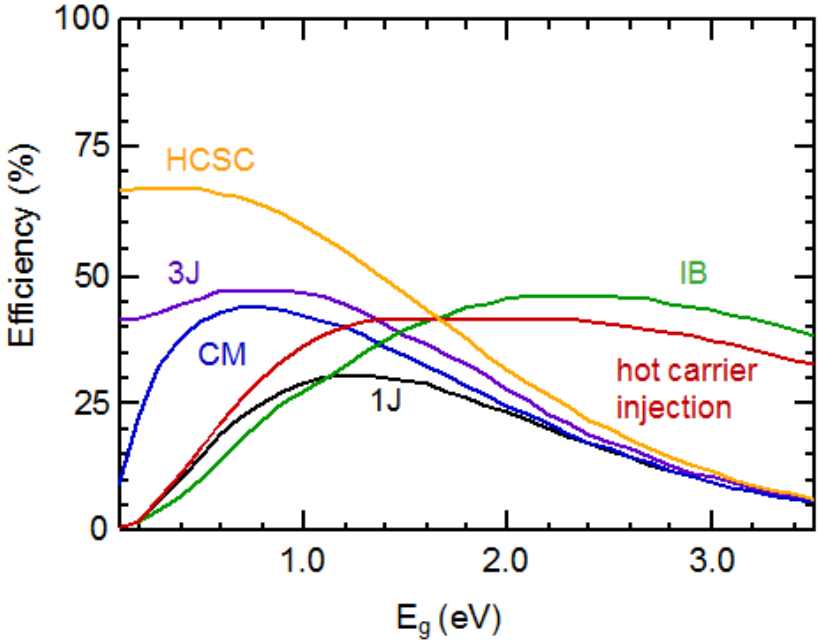


Figure 5.4: Limiting efficiencies of the hot carrier injection cell and other third-generation concepts under 1-sun blackbody spectral illumination. The comparison includes: single-junction (1J), triple-junction (3J), intermediate band (IB), carrier multiplication (CM), and the hot carrier semiconductor solar cell (HCSC). The proposed hot carrier injection cell performs well for most bandgap materials (>1.0 eV).

conductor materials in photovoltaics (*e.g.* $TiO_2$, GaN, etc.). In addition, the hot carrier injection cell is comparable to most of the other third-generation devices for commonly used materials with bandgaps of about 1.1∼1.5 eV (*e.g.* Si and GaAs).

## 5.4 Numerical Demonstration

In order to implement the proposed hot carrier injection cell concept, one needs both significant light absorption within the Ohmic contact and efficient hot electron injection. Recent work on absorbing metal layers employing surface plasmon resonances or metamaterials have shown great promise for the development of absorbing metal contacts by coupling the incident light into surface plasmons that boost the field and absorption in the metal [83, 88, 119, 120, 158, 159].

### 5.4.1 Methods

The Finite Difference Time Domain (FDTD) method was used to calculate the electric field profiles within the device in order to determine absorption in both the semiconductor and the metal contact. A linearly polarized plane wave source was used. The simulation region consisted of the nanostructured metal contact, silicon and air. Spatially dependent absorption in each material was calculated numerically using the equation:

$$abs(\mathbf{r},\omega) = \frac{1}{2}\varepsilon_i\omega|\mathbf{E}(\mathbf{r},\omega)|^2$$

where $\mathbf{E}(\mathbf{r},\omega)$ is the local electric field and $\varepsilon_i$ is the imaginary part of the materials permittivity. The total absorption in the metal was calculated from the integration

of all absorption in the simulation region. The simulated absorption spectrum within the structure is used as an input for the calculation of the hot carrier generation and injection, the photocurrent and power conversion efficiency, and the optimization of bandgap and barrier height, as described elsewhere [93, 94, 139].

### 5.4.2 Results

Here we provide a numerical demonstration of a nanostructured plasmonic array on the back of a *p*-*n* junction solar cell (Fig. 5.5). Simulations were performed for a Si solar cell with square plasmonic arrays for two different metals (Au and Al) (see Fig. 5.5(a) inset). The absorption of sub-bandgap photons within the metal is calculated using the Finite Difference Time Domain (FDTD) method (see Methods). For the Au-coated structure, a ridge width of $w = 190\,\text{nm}$, a height of $h = 135\,\text{nm}$, and a period of $p = 290\,\text{nm}$ are used to achieve relatively broadband absorption. The Al-coated structure has dimensions of $w = 220\,\text{nm}$, $h = 135\,\text{nm}$, and $p = 300\,\text{nm}$ to achieve a nearly perfect absorption just beyond the semiconductor band edge. A metal thickness of 15 nm was used for all structures. Figure 5.5 shows the spectral power density resulting from both the above-bandgap photon absorption and the sub-bandgap photon absorption within the devices under 1-sun blackbody illumination (calculated using the Au and Al EDOS data [140]). The power conversion efficiencies for the Si-Au device and the Si-Al device surpass the Shockley-Queisser limit by 4.7% (yielding 31.2% compared to 29.8%) and by 5.0% (yielding 31.3% compared to 29.8%), respectively. For a metal with a modified

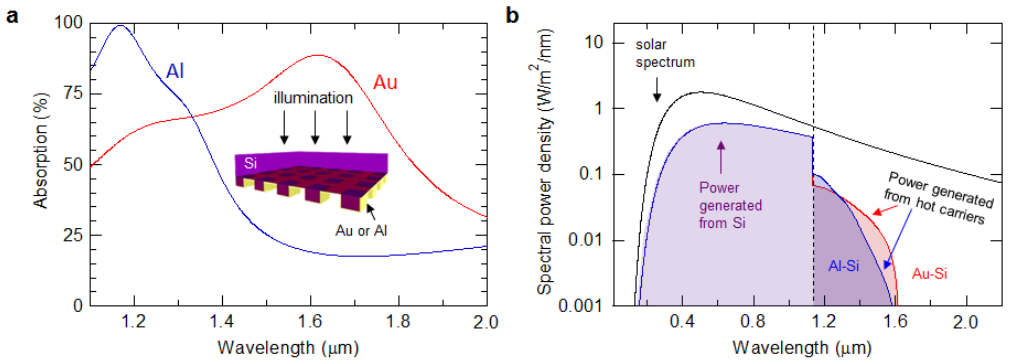


Figure 5.5: Spectral power density for the hot carrier injection device. The device is based on a Si $p$-$n$ junction with an Au or Al nanostructured Ohmic back contact, yielding an efficiency above the Shockley-Queisser limit. The improvement arises from sub-bandgap absorption within the metal and subsequent hot carrier injection, resulting in additional power generation from $\lambda > 1.1\,\mu$m. Inset: Schematic of device under illumination.

EDOS, as described above, with the optical properties of Au, the resulting device efficiency reaches 35.7%, exceeding the SQ limit by 19.8%. Additional improvements are possible through the further optimization of the metallic nanostructures so that the absorption is larger over a broader spectrum.

### 5.4.3 Discussion

In conclusion, we have proposed a novel solar cell architecture that surpasses the SQ limit using sub-bandgap absorption in a nanostructured Ohmic back contact and subsequent hot carrier injection into a conventional $p$-$n$ junction-based device. We have demonstrated feasible designs based on well-studied semiconductors and metals, which will allow for both significant light absorption within the back contact and efficient hot electron injection. Recent experimental results have

shown significant hot carrier current collection for thin metal films and nanostructures [80,81,84,85,92,105,160], which should enable such devices. Further improvements come from engineering the EDOS of the metallic structure from parabolic to narrowly peaked. Employing alloys and quantum confined structures may provide a realistic route toward such modifications [106, 107, 140]. This design paves the way for a new third-generation technique to achieve high power conversion efficiency, in excess of the SQ limit.

# Chapter 6: Conclusions and Future Outlook

## 6.1 Conclusions

This thesis first introduced the basic concepts and the recent advancement of plasmonics and hot carrier effect as well as their potential applications in solar energy harvesting and photodetection. In particular, the solar spectrum can be split into distinct regimes where different materials and devices respond differently. By combining the conventional solar cell with hot carrier-based devices, the solar spectrum can be most efficiently utilized to generate power. Specifically, two hot-carrier device structures were considered here: metal-insulator-metal (M-I-M) for the visible wavelength range and metal-semiconductor (M-S) for near-IR wavelength range.

In Chapters 2 and 3, a TCO-based planar hot carrier device structure was introduced and the working principle were detailed. This structure leverages the high transparency and conductivity of the TCO layer to excite the exponential decay of the electric field at the metal-oxide interface, maximizing the hot carrier injection efficiency. Gold was used as the counter-electrode due to its chemical stability in air and its good absorption of light at the visible wavelengths arising from the inter-band transitions. We also employed aluminum as an alternative counter-electrode

for easy fabrication (and possibly improved interface quality) because a thin layer of native oxide is naturally formed on top of the aluminum surface, serving as the ultra-thin insulator layer between the two electrodes. For both devices, the theoretical and experimental performances were studied systematically. They both exhibited high photoresponse at short wavelengths, and a wavelength dependent $V_{OC}$ was observed. The gold-based device absorbed the incident spectrum well, but surface recombination was large due to the oxide pinholes and surface traps. Further, the complex electron density of states (EDOS) of gold makes the light absorption mechanisms more complicated. The low interface barrier height results in a relatively flat photocurrent-bias voltage relation. The aluminum-based device, however, has a better surface quality at the interface, and performs as well as the gold-based device despite having less absorption. In addition, the EDOS of aluminum is close to an ideal parabola, which gives rise to a linear dependence of photocurrent on bias voltage. To further improve the light absorption in aluminum, we proposed incorporating an additional nanowire-array layer to couple the incident light into surface plasmon modes in the device. The high field enhancement, and hence enhanced absorption, improves the performance at the resonant wavelength.

In Chapter 4, we discussed the application of alternative materials and nanostructures in hot carrier plasmonics. Noble metals, other metals and alloys, some nanostructures including nanowires, graphene and carbon nanotubes (CNT) were investigated based on their EDOS. Depending on the incident photon energy, different materials showed different preferences to either hot electron or hot hole collection. Chapter 4 also provided a rough guideline for choosing materials on the basis

of which hot carrier collection mechanism is more favorable.

To demonstrate the actual benefits of the hot carrier effect for photovoltaics, a novel device structure was proposed in Chapter 5, which integrates the hot carrier injection nanostructures to a traditional single junction semiconductor solar cell. We theoretically investigated the efficiency of the device using a detailed balance model and have shown that the upper limit of the efficiency exceeds the SQ limit of a single junction, non-concentrated device. We also provided a numerical demonstration of the effect, suggesting several nanostructures to achieve improvement in the power conversion efficiency, which paves the way for a new third-generation photovoltaic concept.

## 6.2 Future Outlook

Further research on hot carrier plasmonics in photovoltaics and photodetection could focus on how to improve the performance, *e.g.* the efficiency. The efficiency of hot carrier devices generally relies on two aspects: light absorption and internal hot carrier injection. Chapter 4 explored many different alternative materials and structures in terms of extracting the excited hot carriers efficiently upon excitation of these carriers. Given a specific interface barrier height, choosing the material with an appropriate hot carrier energy distribution would significantly increase the hot carrier injection efficiency. However, to increase the overall efficiency, a much better absorption of the incident energy is necessary. In the following section, we will mainly focus on several strategies to achieve better absorption using surface

plasmons, metamaterials, etc.

### 6.2.1 Planar Metal/Dielectric Stacks

In the previous chapters, we used simple planar metal films as the light absorber. Although gold absorbs well at short wavelengths (below 600 nm), most metals absorb light poorly in the visible and near-IR wavelength ranges due to large reflection arising from the large value of the real part of the dielectric function. The simplest approach to increasing the absorption in metal films is using metal/dielectric stacks [161]. As shown in Fig. 6.1(a), a typical structure consists of a top and a bottom planar metal film, as well as an intermediate dielectric layer. The bottom metal layer should be sufficiently thick (∼100 nm) to avoid transmission, but the top metal layer needs to be thin (∼10s nm) to allow the incident light to get into the cavity. This structure is essentially a Fabry-Perrot (F-P) cavity, with the resonance condition approximately given by:

$$2nd = j\lambda \tag{6.1}$$

where $d$ is the dielectric layer thickness, $n$ is the refractive index of the dielectric layer, $j$ is a positive integer, and $\lambda$ is the incident light wavelength. The field is strongly localized in the cavity between the two metal layers when the resonance condition is satisfied. The absorption has been shown to reach 95% in a cavity structure made up of silver and gold films [161, 162], and a near-IR photodetector has also been reported for the F-P cavity-based hot carrier device [162]. Thus, the near unity absorption at the cavity resonance makes the metal/dielectric stack an

excellent candidate for a hot carrier-based photodetector, and the peak response frequency can be easily tuned by adjusting the cavity thickness; whereas it is not very suitable for photovoltaic applications, because a broadband absorption cannot be obtained within the cavity structure.

### 6.2.2 Metallic Gratings for Coupled Surface Plasmon Polariton (SPP)

As stated in Chapter 2, a surface plasmon polariton (SPP) is a surface wave travelling at the metal-dielectric interface induced by the interaction of light with the free electron oscillation in the metal. While the SPP is excited, the resulting field enhancement at the interface significantly increases the absorption in the metal. Because of the discrepancy between the momentum ($k$ vector) of the SPP and that of the incident light, there has to be a momentum compensation mechanism to excite the SPP. A metallic grating is one of the most common ways to excite an SPP mode in a planar structure. Light incident on the grating (Fig. 6.1(b)) is diffracted and coupled into the SSP mode when the momentum matching condition is met with the aid of the grating periodicity:

$$k_{spp} = k_0 \sin\theta + \frac{2j\pi}{a} \tag{6.2}$$

where $k_{spp}$ and $k_0$ are the momenta of the SPP and the incident light, respectively. $\theta$ is the incident angle, and $a$ is the period of the grating. Note that the SPP mode propagating on the surface of the shallow grating is slightly changed from that on the surface of a planar metal surface [161]. The field is tightly confined near the surface, and the field enhancement naturally results in significantly enhanced absorption.

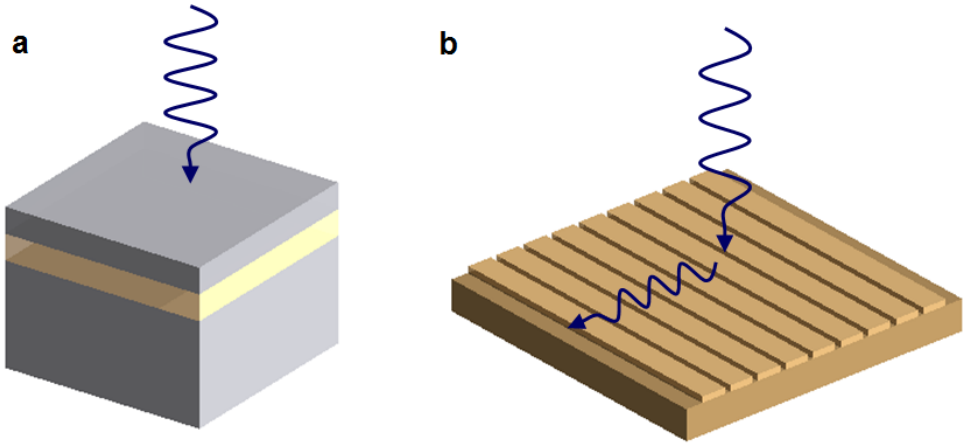


Figure 6.1: Two structures to achieve nearly perfect absorption in a narrow wavelength range. (a) A metal-dielectric-metal Fabry-Perrot resonance cavity. (b) A shallow metallic grating to couple incident light into a SPP mode through the momentum compensation available from the periodicity of the grating.

In fact nearly perfect absorption due to the SPP coupling in gold gratings has been reported [161] and can be utilized as a key component in a narrow-band hot carrier-photodetection device [81]. The resonance frequency can also be adjusted freely by changing the dimensions of the gratings, which is very appealing for hot carrier-based applications.

### 6.2.3 Metallic Nanostructures for Localized Surface Plasmon Resonance (LSPR)

A localized surface plasmon is distinct from an SPP in that once excited, the energy will be localized in an isolated region rather than propagating along the surface. It is the individual metallic nano-component that induces the reso-

nance; whereas the interaction between the neighboring absorbing components is usually weak. The excited LSPR is dissipated through heat when the size of the nano-element is much smaller than the wavelength [20]. The geometry, size and the constituting material of the nanostructure will act together to determine the resonant wavelength and absorption cross-section of the LSPR. Metallic nanorods, nanowires, nano-disks, nanospheres, etc. are the most common structures for the LSPR excitation and many of the structures have been incorporated in hot carrier devices [79, 84–86]. Figure 6.2 shows that a LSPR is excited in gold nano-spheres and nano-disks, resulting in a narrow absorption peak at the resonant wavelength. We also fabricated a gold nano-disk array sample with a $Si_3N_4$ thin film template, with a diameter of 100 nm and a period of 200 nm. The 30 nm gold film was directly deposited through the nano-pores on the thin film template, forming the gold disk array on the ITO-coated glass substrate. The transmission spectrum of the sample was measured using an optical microscope. As shown in Fig. 6.2(c), a transmission dip appears at about 710 nm, which arises from the excited surface plasmon resonance. Generally for a given nano-element, the larger the size of an individual element, the lower the resonance frequency and the longer the resonance wavelength.

However, it is rather challenging to achieve perfect absorption in a single nano-element because of the limited absorption cross-section. The losses get higher when the size is much smaller than the wavelength owing to the increased free electron-surface damping, and the radiation damping starts to dominate when the size is large [20]. Nevertheless by combining a number of nano-elements with different dimensions in a single device, multiple resonance peaks of each individual component

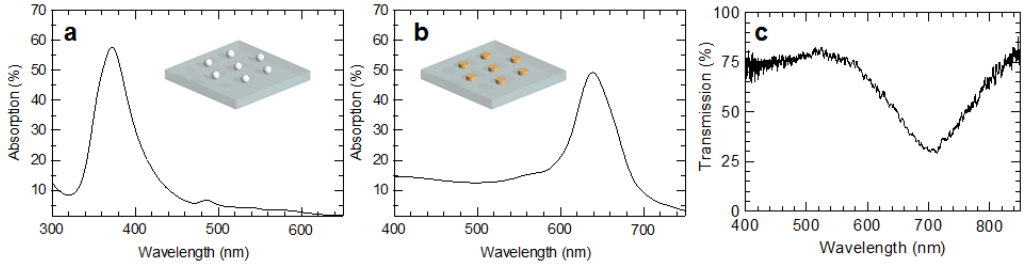


Figure 6.2: Enhanced narrow-band absorption due to the induced LSPR. (a) silver nanospheres (diameter is 40 nm, period is 80 nm) and (b) gold nanodisks (diameter is 80 nm, period is 250 nm). The LSPR depends on the geometry and the size of the nano-element. (c) Transmission spectrum of a gold disk array (diameter is 100 nm, period is 200 nm) measured by the optical microscope. The transmission dip at about 710 nm corresponds to the surface plasmon resonance and hence the absorption peak.

overlap, forming a broadband absorption spectrum. This is very important for solar energy harvesting because the solar spectrum spans widely from near-UV to IR [195].

### 6.2.4 Metamaterial Absorber

Metamaterials (MM) are artificially-engineered materials composed of artificial atoms. Some unique properties, such as a negative refractive index and perfect absorption [163–166] can be obtained using MMs. The artificial atoms are usually comprised of metallic structures in combination with dielectrics, and the resonance in the structures gives rise to unique properties described by effective parameters (*e.g.* electric permittivity $\varepsilon$, magnetic permeability $\mu$, impedance $Z$) of the MM. On the other hand, the spacing between these atoms, *e.g.* lattice constant, has little influence on the macroscopic properties of MM, implying that the material properties are homogeneous. The responses of metamaterials to the incident electromagnetic

waves are similar to those of continuous materials as long as the free space wavelength is much longer than the size of the constituent resonators [164, 167–169]. The tuning of the effective parameters is performed through the modulation of the resonances of the atoms by adjusting the geometric parameters of the structures, rendering the possibility of perfect absorption.

To achieve perfect absorption, a material should be opaque and non-reflective, according to the relation:

$$A = 1 - R - T \tag{6.3}$$

where $A$, $R$, and $T$ denote the absorption, reflection, and transmission of the MM, respectively. Most MM perfect absorbers consist of three layers. The top layer is a periodically arranged metallic structure. The bottom layer is a continuous planar metal. A dielectric layer is sandwiched between the two metal layers [166, 170]. The bottom planar metal layer should be sufficiently thick (thicker than the skin depth of the metal) to prevent light from being transmitted through the structure. The specific design of the top layer is required to match the impedance of free space so that the incident radiation enters the structure without reflection, and the energy is strongly confined within the structure, which is ultimately absorbed by the lossy medium (*e.g.* Ohmic loss and surface plasmon decay in metals within the visible and near-IR frequency ranges).

The radiation incident on the metamaterial can excite resonances of both an electric dipole and a magnetic dipole at certain frequencies. The top plasmonic layer acts as an electric resonator driven by the electric field of the incident light.

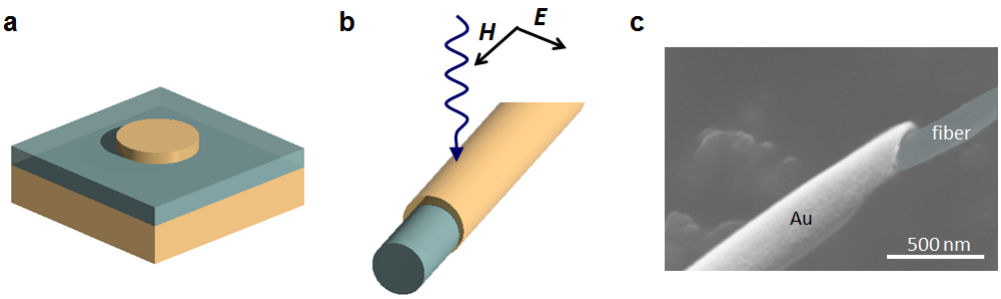


Figure 6.3: Schematics of metamaterial-based perfect absorbers. (a) A perfect absorber consisting of a top layer of nano-patterned metal, an intermediate dielectric layer, and a bottom layer of continuous metallic film. (b) A fiber-based split ring resonator (SRR) for exciting a magnetic resonance. (c) SEM image of SRR fibers fabricated using an electrospinning technique.

The electric dipole resonance is essentially the LSPR because it arises from the oscillation of free charges at the metal surfaces and consequently the fields are confined and significantly enhanced. The resonant behavior can be observed in the effective permittivity $\varepsilon$. Similarly, the magnetic field components of the incident light excite a resonance with anti-parallel currents across the top and bottom metal layers, which form a current loop together with the displacement field in the dielectric [170]. The current loop induces a magnetic field, yielding the magnetic-dipole resonance with a magnetic permeability $\mu$. The effective parameters can be expressed as [165, 171, 172]:

$$\varepsilon(\omega) = 1 - \frac{\omega_{ep}^2 - \omega_{e0}^2}{\omega^2 - \omega_{e0}^2 + i\gamma\omega}$$
$$\mu(\omega) = 1 - \frac{\omega_{mp}^2 - \omega_{m0}^2}{\omega^2 - \omega_{m0}^2 + i\gamma\omega} \tag{6.4}$$

where $\omega_{ep}$, $\omega_{mp}$ are the electric and magnetic plasma frequency, respectively, and

$\omega_{e0}$, $\omega_{m0}$ are the electric and magnetic resonance frequency, respectively, and $\gamma$ is the damping rate (loss). The structure can be optimized to yield perfect impedance matching to free space based on setting the impedance, $Z = \sqrt{\frac{\mu}{\varepsilon}}$, to equal the impedance of vacuum.

The relative strengths and frequencies of the electric and magnetic resonances are tunable by adjusting the geometric sizes of the MM structure. In particular, changing the dimensions of the top plasmonic structure shifts the electric resonance; and changing the thickness of the dielectric layer alters the magnetic resonance [173, 174]. If the electric and magnetic resonances occur at the same frequency, the electromagnetic field will be strongly localized, resulting in high absorption.

In addition to the metal-dielectric-metal structure, a split-ring-resonator (SRR) is another common component that can excite a magnetic dipole resonance. The SRR is a metallic ring with open-gaps. Most of the reported SRRs are fabricated on top of a planar substrate, leaving the ring plane oriented perpendicular to the incident light. The problem with the planar SRR is that the electric field of incident light indirectly couples into the magnetic dipole resonance as a result of the excitation of the current loop, but the magnetic field cannot directly couple into the magnetic resonance, and hence a resonance in the effective permeability cannot be obtained for this angle of incidence. Only when the SRR plane is oriented such that it is parallel with the propagating direction of the incident light, as shown in Fig. 6.3(b), will the direct coupling of the magnetic field into a magnetic dipole resonance give rise to a resonant permeability.

Cylindrical SRR fibers can easily be fabricated using an electro-spinning tech-

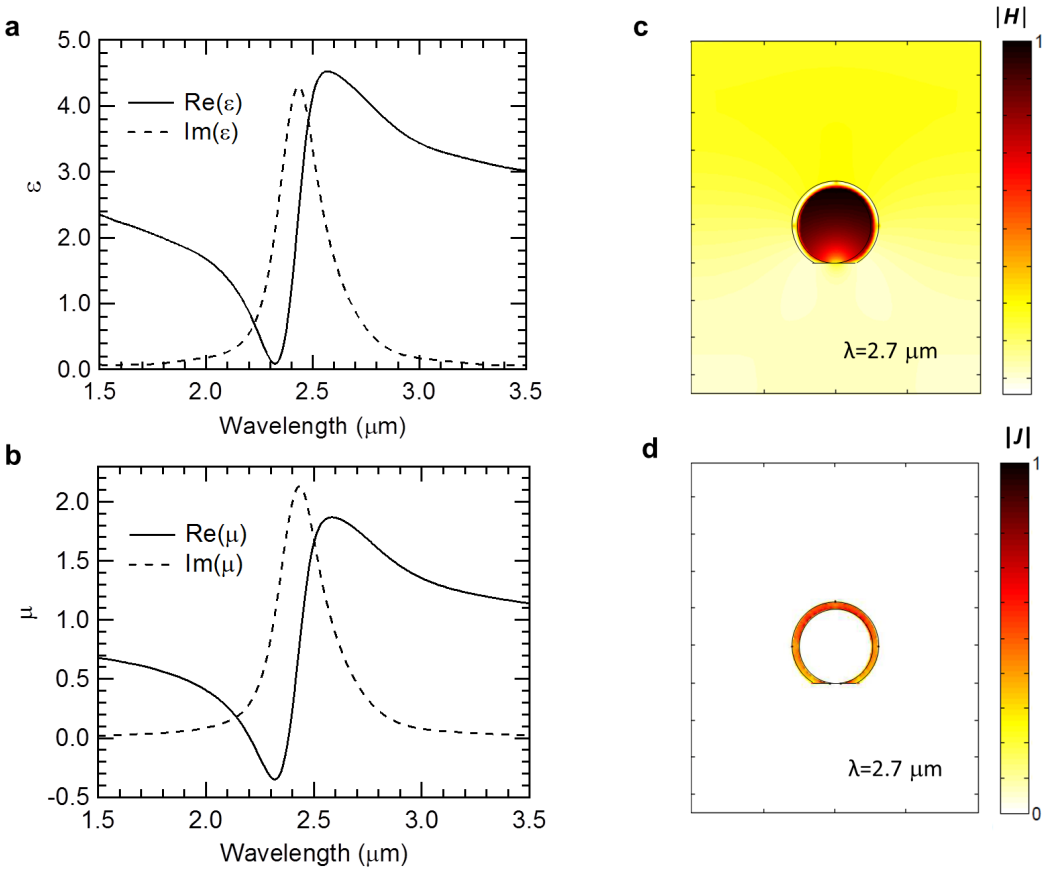


Figure 6.4: Calculated performances of the fiber-based SRR. The diameter of the fiber is 200 nm, exhibiting a strong resonance (2.4 $\mu$m in wavelength for (a) and (b), with a metal coating of 50 nm; and 2.7 $\mu$m in wavelength for (c) and (d), with a thinner metal coating of 20 nm). The extracted parameters are: (a) electric permittivity $\varepsilon$, and (b) magnetic permeability $\mu$. (c) Magnetic field is strongly confined within the ring structure on resonance. (d) The induced current loop is distributed uniformly in the metallic ring, yielding a strong magnetic dipole resonance.

nique. Electro-spinning is a low-cost and scalable technique to make long fibers, either random networks or well oriented fibers, depending on how the fiber collector is designed [175]. In the electro-spinning process, a bias voltage is preferentially applied in one direction to facilitate the alignment of the fibers across an air gap opened in an aluminum foil, making the fibers free-standing. After a subsequent metal deposition, the top edge of the fiber is coated with an open-ended ring of metal (Fig. 6.3(c)). A Transfer Matrix method is used to extract the effective parameters [167, 169, 196] of the SRR fibers (diameter is 200 nm, coated with 50 nm thick gold), and the result is shown in Fig. 6.4. The magnetic field is strongly localized within the ring and a resonant current loop is induced as expected, with the effective permeability showing a strong resonance. The resonance frequency and its strength are tunable by modifying the fiber size and metal coating thickness during the electro-spinning process.

As mentioned above, one big advantage of metameterial perfect absorbers is that broadband perfect absorption is achievable by combining different geometries and sizes to excite distinct, overlapping dipole resonances. The broadband absorption has been investigated recently in different structures and over different wavelength ranges [83, 161, 166, 176], providing a very promising way to improve the performance of hot carrier-based plasmonics devices.

### 6.2.5 Alternative Materials for Hot Carriers

We have detailed various materials in Chapter 4 and discussed their potential applications in hot carrier generation and extraction by considering the hot carrier energy distribution upon excitation. Before the actual hot carrier excitation, as much incident radiation as possible should be absorbed to achieve high efficiency. According to Eq. (2.4), incident energy absorption is proportional to both the imaginary part of the permittivity, which ties into the intrinsic loss of a material, and the field intensity, which can be strongly enhanced through surface plasmon excitation. In other words, direct photon absorption and surface plasmon excitation are the main absorption mechanisms [159]. For most metals, direct photon absorption is intrinsically not efficient because of the low electron-photon interaction cross-section. On the other hand, due to the significant local field enhancement, plasmonic nanostructures can exhibit high absorption cross-sections and hence usually result in more efficient hot carrier generation [159] in spite of the low intrinsic loss. Therefore, the following discussion will mainly focus on a number of approaches to achieving better surface plasmon excitation.

Despite the extensive use of conventional metals in plasmonics, intrinsic problems are associated with them. First of all, conventional metals exhibit relatively high losses at optical frequencies that arise largely from electronic transitions (interband or intraband transitions) and scattering losses [142,177]. In many applications, a small imaginary part of the metal's dielectric function ($\varepsilon$") is required. Further, the optical properties of the conventional metals cannot be easily tuned, which

is a desired feature for many advanced applications. Moreover, noble metals are expensive, and are not compatible with the existing standard semiconductor fabrication and integration processes [178–180]. Lastly, ultra-thin metal films grown by common techniques are often semi-continuous or even discontinuous and consist of many small grains, which increase the losses resulting from grain-boundary scattering and surface roughness [142]. Therefore, seeking alternative materials for hot carrier plasmonics is necessary and important.

According to Eq. (2.3), in order to minimize losses in a plasmonic material, we need to either reduce the damping rate $\gamma$ by growing materials with better crystallinity and cooling them to very low temperatures [181], or reduce the plasma frequency $\omega_p$ by decreasing the carrier concentration. In conventional plasmonic materials, the carrier concentration is very large ($\sim 10^{23}\,\mathrm{cm}^{-3}$), such that losses in visible and IR ranges are intrinsically high. However in recent years, several alternative materials have been proposed and investigated both theoretically and experimentally for implementing low-loss plasmonics.

**Semiconductors.** Semiconductors can be heavily doped to increase the carrier concentration and to achieve optical properties like a metal ($\varepsilon' < 0$) in the desired frequency range [197]. A high carrier concentration ($\sim 10^{21}\,\mathrm{cm}^{-3}$) is required for a common semiconductor (Si) to behave like a metal in the telecommunication wavelength range ($\sim 1.55\ \mu$m) [142]. However, ultra-high doping brings more crystal defects and results in larger losses due to trap states and increased impurity scattering. As a result, optimizing the doping concentration is critical in semiconductor plasmonics. On the other hand, interband transitions are another main loss source

for high-energy photons in a semiconductor. So a relatively wide bandgap is desired for semiconductor-based plasmonics.

Silicon is widely used in the micro-electronics and photonics industries. However, it requires a very high doping concentration to achieve plasmonic properties in the NIR frequency range, rendering it rather challenging. However, highly-doped silicon has been reported to exhibit plasmonic behavior in the mid-IR range (8-10 $\mu$m) [142]. Germanium has an intrinsically higher electron mobility with a smaller Drude damping loss [182]. However, it is even more challenging to get high doping concentrations in germanium. In addition, larger losses arise from the interband transitions in the NIR wavelength regime due to the small bandgap. III-V semiconductors are promising candidates with their tunable bandgaps. GaAs and InP have very high electron mobilities, but doping them heavily is likewise very challenging due to the low solid solubility of the dopants [183]. As for InAs, a carrier concentration of $7.5 \times 10^{19}\,\mathrm{cm}^{-3}$ has been reported and a metal-like plasmonic behavior at wavelengths longer than 6 $\mu$m has been obtained [184] but pushing the plasmonic wavelength further down is also very difficult. GaN has a wide bandgap (3.3 eV) and hence a low interband loss in the visible and IR wavelength regime. Reports have shown that an ultrahigh doping of $3 \times 10^{21}\,\mathrm{cm}^{-3}$ can be achieved with Ge doping [185], which promises its applications in low-loss plasmonics and hot carrier devices for the NIR wavelength range.

**Transparent Conducting Oxides (TCOs).** TCOs usually have large bandgaps, and therefore they are transparent to visible light. Furthermore, the interband transition losses are naturally small, and they can be heavily doped to have metal-like

optical properties [142,178], which make them good candidates for NIR plasmonics. Yet the optical and electrical properties of TCO films depend on the deposition techniques and the thickness of films, which are affected by interfacial defects at the TCO/substrate interface. The aluminum-doped ZnO (AZO) has proved to have the lowest losses when heavily doped due to better crystallinity [142, 179, 186], but it cannot achieve as high of a doping concentration as gallium-doped ZnO (GZO) and ITO. Both the nano-patterned ITO and ZnO have been found to exhibit surface plasmon resonances in the NIR wavelength range, and the losses in the TCOs for the NIR wavelength range are much smaller than those in conventional metals [178,186].

**Dilute Metals.** A dilute metal is a metal that is doped with non-metallic elements to reduce the carrier concentration. However, sometimes the electronic band structures are also altered by those non-metallic elements, so optimizing the doping is critical. Metal silicides and germanides are good candidates in that they exhibit metal-like optical properties in a wide spectral range (visible, NIR and MIR) [187], but compared to noble metals, their optical losses are high due to interband transitions [188]. Metal nitrides also show metallic optical properties in the visible and NIR ranges [179, 189]. Similarly, the interband transitions result in high losses in the frequency regime of interest. The optical properties can also be altered when the deposition conditions are changed, which necessitates accurately tuning the fabrication conditions. Surface plasmon resonances have been reported for wavelengths from 700-900 nm [190]. Although none of the nitrides perform better than silver in the near UV region, some of them (*e.g.* TiN, ZrN) exhibit similar optical properties to gold in the visible region. With their much better tunability, mechanical

durability, and the compatibility with the standard semiconductor fabrication technologies, as well as the much longer carrier relaxation times [191–193], the metal nitrides have very promising applications in the NIR hot carrier plasmonics as long as the properties can be further optimized by exploring more combinations of the compounds.

**Metal Alloys.** Recently, metal alloys have received attention within the plasmonics community [198]. Alloying a noble metal with another metal can change the Fermi level and also shift the transition bands (*e.g.* d-band), which would consequently change the optical properties, such as the plasma frequency and the losses [177]. It was reported that gold-cadmium alloy exhibits larger optical losses in the NIR and visible ranges with a higher carrier concentration, but the transition band is also blue-shifted, moving the loss peak towards the shorter wavelengths [177]. Potassium-gold alloys exhibit extremely small losses below its plasma frequency of 1.54 eV, which seems an excellent candidate for the low-loss plasmonics, but the fabrication of alkali-noble metal compound is very challenging [194].

**Carbon Nanotubes.** Carbon nanotubes (CNTs) are cylindrical nanostructure consisting of carbon. With different structures (single-walled, multi-walled, zigzag, chiral, etc.) and doping conditions, they exhibit unique mechanical, electrical, thermal and optical properties [199–203]. In particular, photodetectors based on single-walled CNT has been reported before, and different absorption spectra are obtained with different CNT structures [204, 205]. Figure 6.5(a) shows the topography of a thin film made of multi-layered conductive CNTs on ethanol-cleaned thin glass slides. The thin film appears black because it has a broadband and nearly

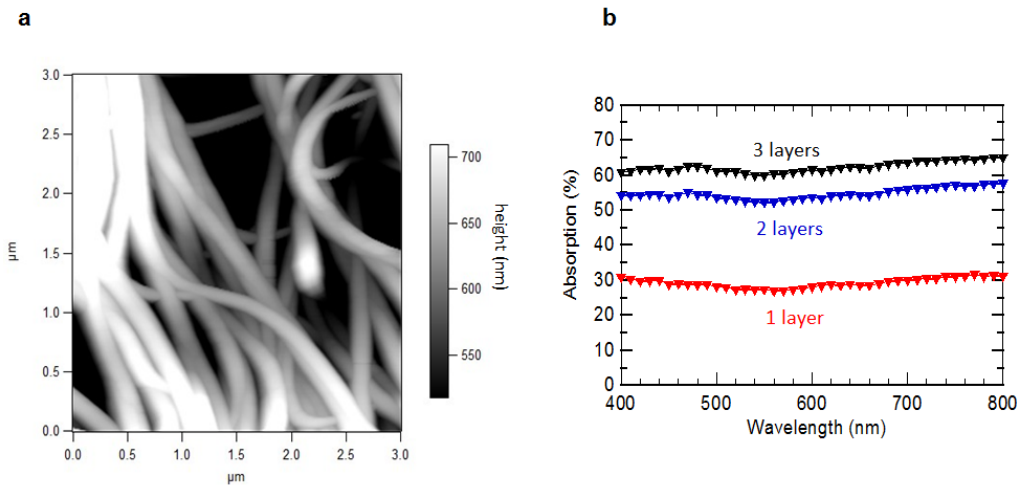


Figure 6.5: Thin films consisting of conductive CNTs. (a) Topography of the multi-layer stacks of CNTs, as determined by atomic force microscopy. (b) Absorption spectrum of the thin films with different layers of CNTs. The absorption is over 60% for all visible wavelengths for the 3-layer stack.

uniform absorption, as shown in Fig. 6.5(b). For 3 layers of CNTs, the absorption is over 60% for all wavelengths in the visible regime, which makes it an ideal candidate for hot carrier excitation and extraction under solar illumination. Further optimization of the growth conditions and the thickness of the film are perhaps needed to improve the performance in order to reach the balance between optical absorption and hot carrier extraction.

In summary, these alternative materials provide a much broader range of possibilities for hot carrier plasmonic materials. When selecting the materials, the potential application and wavelength range are crucial to deciding which material and deposition process to choose. Here, we have taken the first steps in this new field by fabricating the first hot carrier devices based on TCOs, proposed new high efficiency

solar power devices based on these concepts, and have proposed new directions to stimulate further exploration in this exciting field.

# Appendix A: Useful Codes for the Theoretical Modeling and Calculation

In this Appendix chapter, we provide the codes used to calculate the hot carrier device performances, including the light absorption, hot carrier generation, transport, injection in a metal-oxide-TCO device; including the method to compute the upper limit of the hybrid cell using detailed-balance model; including the calculation of the hot carrier redistribution in different materials; and including the effective parameters retrieval for metamaterials.

## A.1 Metal-insulator-TCO Based Hot Carrier Device

### A.1.1 Optical Simulation Using Lumerical FDTD

```
%% get optical data from the simulation %%
select("::model");
d1=get("d1");   % get the thickness of the bottom metal layer
d0=get("d0");   % get the thickness of the oxide layer
height=get("height");   % get the thickness of the top metal (set
    voltage to be 0)
run;   % run the simulation
```

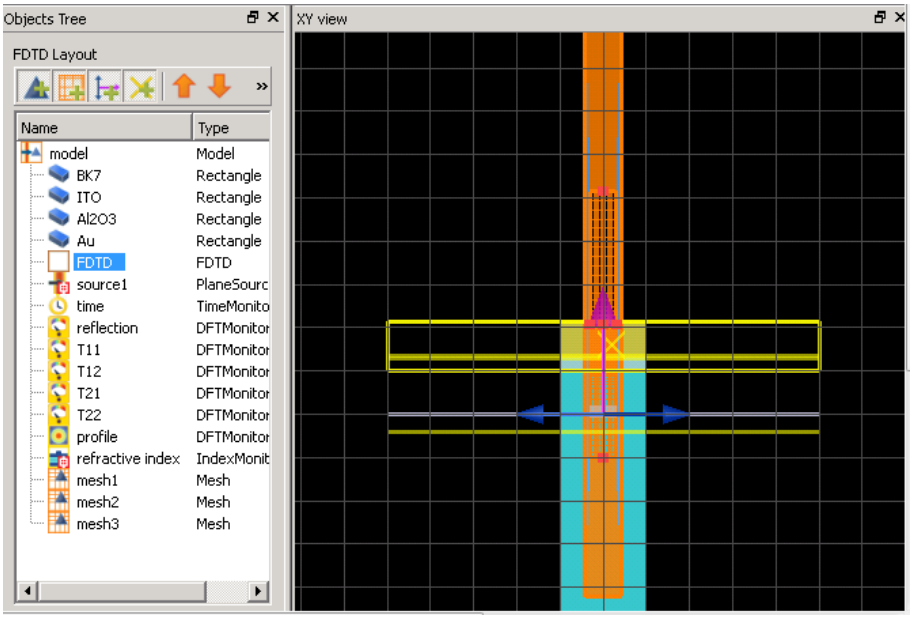


Figure A.1: Lumerical FDTD simulation structure design.

```
reflection=-transmission("reflection");
abs_Au=transmission("T21")-transmission("T22");
abs_ITO=transmission("T11")-transmission("T12");  % Absorption spectrum
x=getdata("profile","x");
y=getdata("profile","y");    % x and y coordinates
f=getdata("profile","f");    % source light frequency
%%%%%%%%%%%%%%% analysis %%%%%%%%%%%%%%%
source_power=sourcepower(f)*(300e-9);  % assume 300 nm long in the z
    direction, the actual length does not mater
E2=pinch(getelectric("profile"),3,1);  % Field intensity
if(havedata("refractive index","index_x")) {
  n=getdata("refractive index","index_x");    % refractive index
}
else {
```

```
  n=getdata("refractive index","index_z");
}
W=meshgrid3dz(x,y,f*2*pi);
SP=meshgrid3dz(x,y,source_power);
epsilon=pinch(eps0*n^2,3,1);  % dielectric function
Pabs=0.5*W*E2*imag(epsilon)*(300e-9)/SP;    % absorption power density
    per unit incident power profile
image(x*1e9,y*1e9,pinch(Pabs,3,1)/max(pinch(Pabs,3,1)),"x(nm)","y(nm)
    ","normalized absorption profile");  % contour image of the
    absorption power density
matlabsave("simulation_variables",d1,d0,height,reflection,abs_Au,
    abs_ITO,x,y,f,source_power,E2,Pabs);  % save data for following
    calculations in MATLAB
%%%%%%%%%%%%%%%%%%%%%%%%%%%%%%%%%%%%%%%%%%%%%%%%%%%%%%%%%%%%%%%%
switchtolayout;  % switch to the original simulation mode to save
    memory space
```

### A.1.2 Main Function in MATLAB for Calculating the Device Performance

```
%%%%%%%% load parameters from FDTD simulation %%%%%%%%%
all=load('simulation_variables.mat');
d0=all.d0; d1=all.d1;
height=all.height;
reflection=all.reflection;
abs_Au=all.abs_Au; abs_ITO=all.abs_ITO;
x=all.x; y=all.y; f=all.f;
```

```
source_power=all.source_power;
E2=all.E2; Pabs=all.Pabs;
%%%
```

```
nx=length(x); ny=length(y); nf=length(f);
Eph=h*f;  % photon energy at different frequencies
Npht=source_power/Eph;  % number of incident photons at different
    frequencies
[variable_1,variable_2,Npht_mtx]=ndgrid(x,y,Npht);
etatotal=Pabs.*Npht_mtx;  % total absorbed photon numbers with all
    frequencies summed up at different positions
E=linspace(Eph/500,Eph,200)';  % hot electron(hole) energy relative to
    Ef
ytopindex=find(y>=d1+d0);  % find the Au layer position
ytop=y(ytopindex);
ybottomindex=find((y<=d1)&(y>=0));  % find the oxide layer position
ybottom=y(ybottomindex);
ymidindex=find((y<=d1+d0)&(y>=d1));  % find the ITO layer position
ymid=y(ymidindex);
etatop=etatotal(1:nx,ytopindex);
[variable_1,variable_2,Eph_mtx1]=ndgrid(x,ytop,Eph);
etabottom=etatotal(1:nx,ybottomindex);
[variable_1,variable_2,Eph_mtx2]=ndgrid(x,ybottom,Eph);
%%%%%%%%%%%%%%%%%%%%%%%%%%%%%%%%%%%%%%%%%%%%%%%%%%%%%%%%%%%%%%%%%%%%%%%
%%% call other m files to complete the calculation %%%
I_tope=curve_1(UT,Ef,V1,delta_B,ymid,ytop,d1,d0,Eg,E,Eph,etatop,x,y,m,
    hbar);
I_bottome=curve_2(UT,Ef,V1,delta_B,ymid,ybottom,d1,d0,Eg,E,Eph,
    etabottom,x,y,m,hbar);
I_toph=curve_3(UT,Ef,V1,V2,delta_B,ymid,ytop,d1,d0,Eg,E,Eph,etatop,x,y,
    m,hbar);
```

```
I_bottomh=curve_4(UT,Ef,V1,V2,delta_B,ymid,ybottom,d1,d0,Eg,E,Eph,
    etabottom,x,y,m,hbar);
%%%%%%%%%%%%%%%%%%%%%%%%%%%%%%%%%%%%%%%%%%%%%%%%%%%%%%%%%%%%%%%%%%%%
total_I=I_tope-I_bottome-I_toph+I_bottomh;  % total photocurrent
I_per_W=total_I/source_power;  % normalized current
product=-total_I.*UT;
total_eff=max(product)/source_power;  % power conversion efficiency
EQE=total_I(find(abs(UT)==min(abs(UT))))/(1.6*10^(-19))/Npht;  % EQE at
     this frequency
plot(UT,I_per_W);
xlabel('voltage (V)');
ylabel('photoresponse (A/W)');
fprintf(fid,'%s\n','PCE='); fprintf(fid,'%f\n',total_eff);
fprintf(fid,'%s\n','Voc=');
fprintf(fid,'%f\n',UT(find(abs(total_I)==min(abs(total_I)))));
fprintf(fid,'%s\n','EQE='); fprintf(fid,'%f\n',EQE);
fprintf(fid,'%s\n','bias(V)'); fprintf(fid,'%f\n',UT);
fprintf(fid,'%s\n','photoresponse(A/W)'); fprintf(fid,'%f\n',I_per_W);
```

### A.1.3 Subfunction I for Calculating Photocurrent

```
%%%%%%%%%%%% top electron current %%%%%%%%%%%%%%
function I_tope=curve_1(UT,Ef,V1,delta_B,ymid,ytop,d1,d0,Eg,E,Eph,
    etatop,x,y,m,hbar)
%%%% In the following analysis, top and 1 mean Au, bottom and 2 mean
    ITO %%%%
I_tope=zeros(length(UT),1);  % top always means the reference metal
N=zeros(length(E),1);  % number of carriers collected with energy E
```

```
for count=1:length(UT)
    Ef1=Ef;  % top layer Fermi level
    Ef2=Ef-1.6*10^(-19)*UT(count);  % bottom layer Fermi level
    U1=V1-1.6*10^(-19)*UT(count)+delta_B+(ymid-d1)/d0*(1.6*10^(-19)*UT(
    count)-delta_B);  % conduction bandedge across the insulator
    U2=U1-Eg;
    U1_max=max(U1);
    for i=1:length(E)
      le=3.267*10^(-9)*(E(i)+Ef1)*Ef1/(E(i)^2);  % mean free path of Au
      if UT(count)~=delta_B/1.6*10^19
        yturning=d1+(E(i)+Ef1+1.6*10^(-19)*UT(count)-V1-delta_B)*d0
    /(1.6*10^(-19)*UT(count)-delta_B);
        if yturning>=d1+d0 yturning=d1+d0;
        elseif yturning<=d1 yturning=d1;
        end  % turning point at the conduction band
      else yturning=d1;
      end
      Po=1/Eph/2;
      if UT(count)>=delta_B/1.6*10^19
        ymidindex1=find((y<=d1+d0)&(y>=yturning));
        if isempty(ymidindex1) ymidindex1=find(abs(y-d1-d0)==min(abs(y-
    d1-d0)));  % cannot find the index
        end
      else
        ymidindex1=find((y>=d1)&(y<=yturning));
        if isempty(ymidindex1) ymidindex1=find(abs(y-d1)==min(abs(y-d1)
    ));
```

```
29          end
30        end
31        ymid1=y(ymidindex1);  % the effective tunneling region
32        U1_prime=interp1(ymid,U1,ymid1);
33        U2_prime=interp1(ymid,U2,ymid1);
34        integrand_0=Po*etatop;
35        pexc=trapz(x,integrand_0,1)';
36        Ey=linspace(0.005*(Ef1+E(i)),Ef1+E(i),100)';
37        [Pexc,variable_1,variable_2]=ndgrid(pexc,ymid1,Ey);
38        [Ytop,variable_1,variable_2]=ndgrid(ytop,ymid1,Ey);
39        [variable_1,Ymid1,variable_2]=ndgrid(ytop,ymid1,Ey);
40        [variable_1,variable_2,EY]=ndgrid(ytop,ymid1,Ey);
41        [variable_1,U1_mtx,variable_2]=ndgrid(ytop,U1_prime,Ey);
42        [variable_1,U2_mtx,variable_2]=ndgrid(ytop,U2_prime,Ey);
43        costheta=sqrt(EY/(E(i)+Ef1));
44        integrand_1=Pexc.*exp(-(Ytop-d1-d0)/le./costheta);
45        Nint=trapz(ytop,integrand_1,1);
46        Nint=squeeze(Nint(:,1,:));
47        if E(i)>-1.6*10^(-19)*UT(count)  % considering the Pauli
    principle when calculating tunneling
48          if E(i)+Ef1<U1_max
49            ky2=2*m/(hbar^2)*((E(i)+Ef1-U1_mtx).*(E(i)+Ef1-U2_mtx)/Eg-(E(
    i)+Ef1-EY));
50            integrand_2=sqrt(-ky2);
51            Ptun=exp(-2*trapz(ymid1,integrand_2,2));  % tunneling
    probability with energy E(i) and Ey
52            Ptun=squeeze(Ptun(1,:,:));
```

```
53          else Ptun=1;
54          end
55        else Ptun=0;
56        end
57        integrand=0.5*1./sqrt(Ey)/sqrt(E(i)+Ef1).*Nint.*Ptun;
58        N(i)=trapz(Ey,integrand,1);
59      end
60      I1=1.6*10^(-19)*trapz(E,N,1);
61      I_tope(count)=I1;
62  end
```

### A.1.4 Subfunction II for Calculating Photocurrent

```
1  function I_bottome=curve_2(UT,Ef,V1,delta_B,ymid,ybottom,d1,d0,Eg,E,Eph
       ,etabottom,x,y,m,hbar)
2  %%%%%%%%%%%%%%%% bottom electron current %%%%%%%%%%%
3  I_bottome=zeros(length(UT),1);
4  N=zeros(length(E),1);  % number of carriers collected with energy E
5  for count=1:length(UT)
6    Ef1=Ef;  % top layer Fermi level
7    Ef2=Ef-1.6*10^(-19)*UT(count);  % bottom layer Fermi level
8    U1=V1-1.6*10^(-19)*UT(count)+delta_B+(ymid-d1)/d0*(1.6*10^(-19)*UT(
       count)-delta_B);  % voltage inside the insulator layer
9    U2=U1-Eg;
10   U1_max=max(U1);
11   for i=1:length(E)
12     le=12*10^(-9);  % mean free path of ITO
13     if UT(count)~=delta_B/1.6*10^19
```

```
14      yturning=d1+(E(i)+Ef2+1.6*10^(-19)*UT(count)-V1-delta_B)*d0
    /(1.6*10^(-19)*UT(count)-delta_B);
15      if yturning>=d1+d0 yturning=d1+d0;
16      elseif yturning<=d1 yturning=d1;
17      end
18    else yturning=d1;
19    end
20    Po=1/Eph/2;
21    if UT(count)>=delta_B/1.6*10^19
22      ymidindex1=find((y<=d1+d0)&(y>=yturning));
23      if isempty(ymidindex1) ymidindex1=find(abs(y-d1-d0)==min(abs(y-d1
    -d0)));
24      end
25    else
26      ymidindex1=find((y>=d1)&(y<=yturning));
27      if isempty(ymidindex1) ymidindex1=find(abs(y-d1)==min(abs(y-d1)))
    ;
28      end
29    end
30    ymid1=y(ymidindex1);
31    U1_prime=interp1(ymid,U1,ymid1);
32    U2_prime=interp1(ymid,U2,ymid1);
33    integrand_0=Po*etabottom;
34    pexc=trapz(x,integrand_0,1)';
35    Ey=linspace(0.005*(Ef1+E(i)),Ef1+E(i),100)';
36    [Pexc,variable_1,variable_2]=ndgrid(pexc,ymid1,Ey);
37    [Ybottom,variable_1,variable_2]=ndgrid(ybottom,ymid1,Ey);
```

```
    [variable_1 ,Ymid1, variable_2]=ndgrid(ybottom ,ymid1 ,Ey);
    [variable_1 , variable_2 ,EY]=ndgrid(ybottom ,ymid1 ,Ey);
    [variable_1 ,U1_mtx, variable_2]=ndgrid(ybottom ,U1_prime ,Ey);
    [variable_1 ,U2_mtx, variable_2]=ndgrid(ybottom ,U2_prime ,Ey);
    costheta=sqrt(EY/(E(i)+Ef1));
    integrand_1=Pexc.*exp(-(d1-Ybottom)/le./costheta);
    Nint=trapz(ybottom ,integrand_1 ,1);
    Nint=squeeze(Nint(:,1,:));
    if E(i)>1.6*10^(-19)*UT(count)
      if E(i)+Ef2<U1_max
        ky2=2*m/(hbar^2)*((E(i)+Ef2-U1_mtx).*(E(i)+Ef2-U2_mtx)/Eg-(E(i)
  +Ef1-EY));
        integrand_2=sqrt(-ky2);
        Ptun=exp(-2*trapz(ymid1 ,integrand_2 ,2));
        Ptun=squeeze(Ptun(1,:,:));
      else Ptun=1;
      end
    else Ptun=0;
    end
    integrand=0.5*1./sqrt(Ey)/sqrt(E(i)+Ef1).*Nint.*Ptun;
    N(i)=trapz(Ey,integrand ,1);
  end
  I2=1.6*10^(-19)*trapz(E,N,1);
  I_bottome(count)=I2;
end
```

### A.1.5 Subfunction III for Calculating Photocurrent

```
%%%%%%%%%%%%%%%% top hole current %%%%%%%%%%%%%%%%%%%
function I_toph=curve_3(UT,Ef,V1,V2,delta_B,ymid,ytop,d1,d0,Eg,E,Eph,
    etatop,x,y,m,hbar)
I_toph=zeros(length(UT),1);
N=zeros(length(E),1);  % number of carriers collected with energy E
for count=1:length(UT)
  Ef1=Ef;  % top layer Fermi level
  Ef2=Ef-1.6*10^(-19)*UT(count);  % bottom layer Fermi level
  U1=V1-1.6*10^(-19)*UT(count)+delta_B+(ymid-d1)/d0*(1.6*10^(-19)*UT(
    count)-delta_B);
  U2=U1-Eg;
  U2_min=min(U2);
  for i=1:length(E)
    le=3.267*10^(-9)*(E(i)+Ef1)*Ef1/(E(i)^2);
    if UT(count)~=delta_B/1.6*10^19
      yturning=d1+(-E(i)+Ef1+1.6*10^(-19)*UT(count)-V2-delta_B)*d0
    /(1.6*10^(-19)*UT(count)-delta_B);
      if yturning>=d1+d0 yturning=d1+d0;
      elseif yturning<=d1 yturning=d1;
      end
    else yturning=d1;
    end
    Po=1/Eph/2;
    if UT(count)<=delta_B/1.6*10^19
      ymidindex1=find((y<=d1+d0)&(y>=yturning));
```

```
23        if isempty(ymidindex1) ymidindex1=find(abs(y-d1-d0)==min(abs(y-d1
    -d0)));
24        end
25     else
26        ymidindex1=find((y>=d1)&(y<=yturning));
27        if isempty(ymidindex1) ymidindex1=find(abs(y-d1)==min(abs(y-d1)))
    ;
28        end
29     end
30     ymid1=y(ymidindex1);
31     U1_prime=interp1(ymid,U1,ymid1);
32     U2_prime=interp1(ymid,U2,ymid1);
33     integrand_0=Po*etatop;
34     pexc=trapz(x,integrand_0,1)';
35     Ey=linspace(0.005*(Ef1-E(i)),Ef1-E(i),100)';
36     [Pexc,variable_1,variable_2]=ndgrid(pexc,ymid1,Ey);
37     [Ytop,variable_1,variable_2]=ndgrid(ytop,ymid1,Ey);
38     [variable_1,Ymid1,variable_2]=ndgrid(ytop,ymid1,Ey);
39     [variable_1,variable_2,EY]=ndgrid(ytop,ymid1,Ey);
40     [variable_1,U1_mtx,variable_2]=ndgrid(ytop,U1_prime,Ey);
41     [variable_1,U2_mtx,variable_2]=ndgrid(ytop,U2_prime,Ey);
42     costheta=sqrt(EY/(Ef1-E(i)));
43     integrand_1=Pexc.*exp(-(Ytop-d1-d0)/le./costheta);
44     Nint=trapz(ytop,integrand_1,1);
45     Nint=squeeze(Nint(:,1,:));
46     if E(i)>1.6*10^(-19)*UT(count)
47        if -E(i)+Ef1>U2_min
```

```
48          ky2=2*m/(hbar^2)*((-E(i)+Ef1-U1_mtx).*(-E(i)+Ef1-U2_mtx)/Eg-(-E
    (i)+Ef1-EY));
49          integrand_2=sqrt(-ky2);
50          Ptun=exp(-2*trapz(ymid1,integrand_2,2));
51          Ptun=squeeze(Ptun(1,:,:));
52        else Ptun=1;
53        end
54      else Ptun=0;
55      end
56      integrand=0.5*1./sqrt(Ey)/sqrt(-E(i)+Ef1).*Nint.*Ptun;
57      N(i)=trapz(Ey,integrand,1);
58    end
59    I3=1.6*10^(-19)*trapz(E,N,1);
60    I_toph(count)=I3;
61  end
```

### A.1.6 Subfunction IV for Calculating Photocurrent

```
1  function I_bottomh=curve_4(UT,Ef,V1,V2,delta_B,ymid,ybottom,d1,d,Eg,E,
       Eph,etabottom,x,y,m,hbar)
2  %%%%%%%%%%%%%%%% bottom hole current %%%%%%%%%%%%%%%%
3  I_bottomh=zeros(length(UT),1);
4  N=zeros(length(E),1);  % number of carriers collected with energy E
5  for count=1:length(UT)
6    Ef1=Ef;  % top layer Fermi level
7    Ef2=Ef-1.6*10^(-19)*UT(count);  % bottom layer Fermi level
8    U1=V1-1.6*10^(-19)*UT(count)+delta_B+(ymid-d1)/d0*(1.6*10^(-19)*UT(
       count)-delta_B);
```

```
U2=U1-Eg;
U2_min=min(U2);
for i=1:length(E)
  le=12*10^(-9);  % mean free path of ITO
  if UT(count)~=delta_B/1.6*10^19
    yturning=d1+(-E(i)+Ef2+1.6*10^(-19)*UT(count)-V2-delta_B)*d0/(1.6
 e-19*UT(count)-delta_B);
    if yturning>=d1+d0 yturning=d1+d0;
    elseif yturning<=d1 yturning=d1;
    end
  else yturning=d1;
  end
  Po=1/Eph/2;
  if UT(count)<=delta_B/1.6*10^19
    ymidindex1=find((y<=d1+d0)&(y>=yturning));
    if isempty(ymidindex1) ymidindex1=find(abs(y-d1-d0)==min(abs(y-d1
-d0)));
    end
  else
    ymidindex1=find((y>=d1)&(y<=yturning));
    if isempty(ymidindex1) ymidindex1=find(abs(y-d1)==min(abs(y-d1)))
;
    end
  end
  ymid1=y(ymidindex1);
  U1_prime=interp1(ymid,U1,ymid1);
  U2_prime=interp1(ymid,U2,ymid1);
```

```
33      integrand_0=Po*etabottom;
34      pexc=trapz(x,integrand_0,1)';
35      Ey=linspace(0.005*(Ef1-E(i)),Ef1-E(i),100)';
36      [Pexc,variable_1,variable_2]=ndgrid(pexc,ymid1,Ey);
37      [Ybottom,variable_1,variable_2]=ndgrid(ybottom,ymid1,Ey);
38      [variable_1,Ymid1,variable_2]=ndgrid(ybottom,ymid1,Ey);
39      [variable_1,variable_2,EY]=ndgrid(ybottom,ymid1,Ey);
40      [variable_1,U1_mtx,variable_2]=ndgrid(ybottom,U1_prime,Ey);
41      [variable_1,U2_mtx,variable_2]=ndgrid(ybottom,U2_prime,Ey);
42      costheta=sqrt(EY/(Ef1-E(i)));
43      integrand_1=Pexc.*exp(-(d1-Ybottom)/le./costheta);
44      Nint=trapz(ybottom,integrand_1,1);
45      Nint=squeeze(Nint(:,1,:));
46      if E(i)>-1.6*10^(-19)*UT(count)
47        if -E(i)+Ef2>U2_min
48          ky2=2*m/(hbar^2)*((-E(i)+Ef2-U1_mtx).*(-E(i)+Ef2-U2_mtx)/Eg-(-E
    (i)+Ef1-EY));
49          integrand_2=sqrt(-ky2);
50          Ptun=exp(-2*trapz(ymid1,integrand_2,2));
51          Ptun=squeeze(Ptun(1,:,:));
52        else Ptun=1;
53        end
54      else Ptun=0;
55      end
56      integrand=0.5*1./sqrt(Ey)/sqrt(-E(i)+Ef1).*Nint.*Ptun;
57      N(i)=trapz(Ey,integrand,1);
58    end
```

```
59    I4=1.6*10^(-19)*trapz(E,N,1);
60    I_bottomh(count)=I4;
61  end
```

## A.2 Hot Carrier Injection Device

### A.2.1 MATLAB code for Calculating the Theoretical Efficiency

```
1  fid=fopen('result.txt','wt');  % open a text file to store the data
2  %%%%%%%%%%%%%%%%%%%%% parameters %%%%%%%%%%%%%%%%%%%
3  h=6.626*10^(-34); c=3*10^8; pi=3.1416;
4  Ts=5760; Tc=300; thetaS=0.00467;  % solar light angle
5  kB=1.381*10^(-23); q=1.6*10^(-19);
6  Eg=1.1*q;  % Bandgap of the semiconductor
7  Ef=0.15*q;  % Fermi energy of the metal contact
8  P_total=1360.8;  % incident solar power without concentration
9  %%%%%%%%%%%%%%%%%%%%%%%%%%%%%%%%%%%%%%%%%%%%%%%%%%%%%%%%
10 %%%%%%%%%%%%%%%%%%%%%%%%%%%%%%%%%%%%%%%%%%%%%%%%%%%%%%%%
11 num1=70; num2=600;
12 phi_B=linspace(Eg/2,Eg,num1)';  % The barrier height range
13 eta=zeros(num1,1);
14 J_sc=zeros(num1,1);
15 V_oc=zeros(num1,1);    % efficiency, Jsc and Voc all vary with the
       barrier height
16 V=linspace(0,Eg/q-0.15,num2)';   % vary the bias voltage
17 JL_low=zeros(num1,num2);   % sub-bandgap photocurrent
18 JL_high=zeros(num1,num2);   % above-bandgap photocurrent
19 num3=15000; num4=10000; num5=15000;
```

```
E_high=linspace(Eg,100*Eg,num3)';   % photon energy above the bandgap
E_low=linspace(Eg/1000,Eg,num4)';   % photon energy below the bandgap
y1=2/h^3/c^2*E_high.^2./(exp(E_high/kB/Ts)-1);
fun1=trapz(E_high,y1);
JL_high_t=q*pi/2*(1-cos(2*thetaS))*fun1;   % photo-generated current
    due to the p-n junction absorption
y3=2/h^3/c^2*E_high.^2./(exp(E_high/kB/Tc)-1);
fun3=trapz(E_high,y3);
J_ambient=q*pi*fun3;   % Current from ambient absorption
y5=2/h^3/c^2*E_high.^2.*exp(-E_high/kB/Tc);
fun5=trapz(E_high,y5);
J_emi=q*pi*fun5*exp(q*V/kB/Tc);  % Reverse saturation current
for i=1:num1
    ind=max(find(abs(V-phi_B(i)/q)==min(abs(V-phi_B(i)/q))));  % find
    the maximum voltage
    Prob=zeros(num4,1);  % Probability of hot carrier injection at each
     wavelength
    for j=1:num4
        if E_low(j)<=phi_B(i)   % Low energy carriers will be blocked
            Prob(j)=0;
        else
            if E_low(j)<Ef E=linspace(0,E_low(j),num5)';
            else E=linspace(E_low(j)-Ef,E_low(j),num5)';
            end
            integrand=zeros(num5,1);
            row_1=sqrt(Ef+E);   % EDOS of the initial state
            row_2=sqrt(Ef+E-E_low(j));   % EDOS of the final state
```

```
44              EDJDOS=row_1.*row_2;    % Joint EDOS
45              func_1=trapz(E,EDJDOS); point=find(E>phi_B(i));
46              integrand(point)=EDJDOS(point);
47              func_2=trapz(E,integrand); Prob(j)=func_2/func_1;
48          end
49      end
50      y2=2/h^3/c^2*E_low.^2./(exp(E_low/kB/Ts)-1).*Prob;
51      fun2=trapz(E_low,y2);
52      JL_low(i,1:ind)=q*pi/2*(1-cos(2*thetaS))*fun2;  % Photocurrent due
    to hot carrier injection
53      JL_high(i,1:ind)=JL_high_t;
54      J=JL_low(i,1:num2)'+JL_high(i,1:num2)'+J_ambient-J_emi;    % total
    current
55      eff=J.*V/P_total;
56      index=max(find(eff==max(eff))); eta(i)=eff(index);
57      J_sc(i)=JL_low(i,1)+JL_high(i,1);
58      index_1=max(find(abs(J)==min(abs(J))));
59      V_oc(i)=V(index_1);
60  end
61  eta_opt=max(eta);  % The ultimate efficiency for a given Eg
62  index_2=max(find(eta==eta_opt));
63  phi_B_opt=phi_B(index_2);
64  J_sc_opt=J_sc(index_2); V_oc_opt=V_oc(index_2);
65  J_opt=JL_low(index_2,1:num2)'+JL_high(index_2,1:num2)'+J_ambient-J_emi;
66  figure
67  plot(V,J_opt);
68  xlabel('Voltage (V)'); ylabel('Current (A/m^2)');
```

```
figure
plot(phi_B/q,eta*100);
xlabel('barrier height (eV)'); ylabel('efficiebcy (%)');
fprintf(fid,'%s\n','bandgap (eV)'); fprintf(fid,'%f\n',Eg/q);
fprintf(fid,'%s\n','Fermi level (eV)'); fprintf(fid,'%f\n',Ef/q);
fprintf(fid,'%s\n','the optimized barrier (eV)');
fprintf(fid,'%f\n',phi_B_opt/q); fprintf(fid,'%s\n','the optimized
    efficiency');
fprintf(fid,'%f\n',eta_opt); fprintf(fid,'%s\n','the optimized J_sc (A/
    m^2)');
fprintf(fid,'%f\n',J_sc_opt); fprintf(fid,'%s\n','the optimized V_oc (V
    )');
fprintf(fid,'%f\n',V_oc_opt); fprintf(fid,'%s\n','the barrier (eV)');
fprintf(fid,'%f\n',phi_B/q); fprintf(fid,'%s\n','the efficiency');
fprintf(fid,'%f\n',eta); fprintf(fid,'%s\n','the J_sc (A/m^2)');
fprintf(fid,'%f\n',J_sc); fprintf(fid,'%s\n','the V_oc (V)');
fprintf(fid,'%f\n',V_oc); fprintf(fid,'%s\n','Bias (V)');
fprintf(fid,'%f\n',V); fprintf(fid,'%s\n','Current (A/m^2)');
fprintf(fid,'%f\n',J_opt);
```

### A.2.2 MATLAB code for Calculating the Efficiency of Real Device with the Nanostructured Contact

The parameters needed are the same as the above code, so we just start with the main code. We need one xlsx file named 'data.xlsx' to store the data of the back contact material's EDOS , and another xlsx file named 'analysis.xlsx' to store the sub-bandgap absorption spectrum data before running the following scripts.

```
%%%
```

```
JL_high_t=q*pi/2*(1-cos(2*thetaS))*fun1;
y3=2/h^3/c^2*E_high.^2./(exp(E_high/kB/Tc)-1);
fun3=trapz(E_high,y3);
J_ambient=q*pi*fun3;
y5=2/h^3/c^2*E_high.^2.*exp(-E_high/kB/Tc);
fun5=trapz(E_high,y5);
J_emi=q*pi*fun5*exp(q*V/kB/Tc);
for i=1:num1
    ind=max(find(abs(V-phi_B(i)/q)==min(abs(V-phi_B(i)/q))));
    Prob=zeros(num4,1);
    for j=1:num4
        if E_low(j)<=phi_B(i) Prob(j)=0;
        else
            E=linspace(0,E_low(j),num5)'; integrand=zeros(num5,1);
            row_1=interp1(E_dos_t,dos_t,-E);  % extrapolate the EDOS
   data for the initial state
            row_2=interp1(E_dos_t,dos_t,-E+E_low(j));   % extrapolate
   the EDOS data for the final state
            EDJDOS=row_1.*row_2; func_1=trapz(E,EDJDOS);
            point=find(E>phi_B(i)); integrand(point)=EDJDOS(point);
            func_2=trapz(E,integrand); Prob(j)=func_2/func_1;
        end
    end
    y2=2/h^3/c^2*E_low.^2./(exp(E_low/kB/Ts)-1).*Prob.*abs_Au;
    fun2=trapz(E_low,y2);
    JL_low(i,1:ind)=q*pi/2*(1-cos(2*thetaS))*fun2;
    JL_high(i,1:ind)=JL_high_t;
```

```
49      J=JL_low(i,1:num2)'+JL_high(i,1:num2)'+J_ambient-J_emi;
50      eff=J.*V/P_total; index=max(find(eff==max(eff)));
51      eta(i)=eff(index);
52      J_sc(i)=JL_low(i,1)+JL_high(i,1);
53      index_1=max(find(abs(J)==min(abs(J))));
54      V_oc(i)=V(index_1);
55  end
56  eta_opt=max(eta); index_2=max(find(eta==eta_opt));
57  phi_B_opt=phi_B(index_2);
58  J_sc_opt=J_sc(index_2); V_oc_opt=V_oc(index_2);
59  J_opt=JL_low(index_2,1:num2)'+JL_high(index_2,1:num2)'+J_ambient-J_emi;
60  figure
61  plot(phi_B/q,eta*100);
62  xlabel('barrier height (eV)'); ylabel('efficiebcy (%)');
63  fprintf(fid,'%s\n','bandgap (eV)'); fprintf(fid,'%f\n',Eg/q);
64  fprintf(fid,'%s\n','Fermi level (eV)'); fprintf(fid,'%f\n',Ef/q);
65  fprintf(fid,'%s\n','the optimized barrier (eV)'); fprintf(fid,'%f\n',
        phi_B_opt/q);
66  fprintf(fid,'%s\n','the optimized efficiency'); fprintf(fid,'%f\n',
        eta_opt);
67  fprintf(fid,'%s\n','the optimized J_sc (A/m^2)'); fprintf(fid,'%f\n',
        J_sc_opt);
68  fprintf(fid,'%s\n','the optimized V_oc (V)'); fprintf(fid,'%f\n',
        V_oc_opt);
69  fprintf(fid,'%s\n','the barrier (eV)'); fprintf(fid,'%f\n',phi_B/q);
70  fprintf(fid,'%s\n','the efficiency'); fprintf(fid,'%f\n',eta);
71  fprintf(fid,'%s\n','the J_sc (A/m^2)');
```

```
fprintf(fid,'%f\n',J_sc); fprintf(fid,'%s\n','the V_oc (V)');
fprintf(fid,'%f\n',V_oc); fprintf(fid,'%s\n','Bias (V)');
fprintf(fid,'%f\n',V); fprintf(fid,'%s\n','Current (A/m^2)');
fprintf(fid,'%f\n',J_opt);
```

### A.2.3 MATLAB code for Calculating Power Generation Spectrum

Here we also leave out the declaration of those parameters since they are the same as before. Before running this script, a xlsx file named 'I_V.xlsx' is needed to store the current-voltage data obtained from the above code.

```
%%%%%%%%%%%%%%%%%%%%%%%%%%%%%%%%%%%%%%%%%%%%%%%%%%%%%%%%%%%%%%%%%%%%%%%%%%%%%%%%
V=xlsread('I_V.xlsx','Sheet1','A2:A601');
J=xlsread('I_V.xlsx','Sheet1','B2:B601');
power=J.*V; index=max(find(power==max(power)));
V_opt=V(index);   % find the voltage where the maximum power is
    generated.
factor=J(index)/max(J);
%%%%%%%%%%%%%%%%%%%%%%%%%%%%%%%%%%%%%%%%%%%%%%%%%%%%%%%%%%%%%%%%%%%%%%%%%%%%%%%%
E_dos=xlsread('data.xlsx','Sheet1','A2:A789')*q-Ef;
dos=xlsread('data.xlsx','Sheet1','C2:C789');
E_min=min(E_dos); E_max=max(E_dos);
E_dos_t=linspace(E_min,E_max,500);
dos_t=zeros(500,1);
for i=1:500
    index=max(find(abs(E_dos-E_dos_t(i))==min(abs(E_dos-E_dos_t(i)))));
    dos_t(i)=dos(index);
```

```
end
num1=10000; num2=20000;
y0=2/h^3/c^2*E_high.^3./(exp(E_high/kB/Ts)-1);
P_high_in=pi/2*(1-cos(2*thetaS)).*y0;  % incident power spectrum of
    above bandgap photons
y1=2/h^3/c^2*E_high.^2./(exp(E_high/kB/Ts)-1);
JL_high=q*pi/2*(1-cos(2*thetaS)).*y1;
P_high_out=JL_high.*V_opt*factor;  % Power generation by above bandgap
    photons
lamda_ph=xlsread('analysis.xlsx','Sheet1','A2:A435')*1e-6;   % sub-
    bangap wavelength
E_ph=h*c./lamda_ph;  % photon energy below the bandgap
num4=length(E_ph); num5=5000;
abs_Au=xlsread('analysis.xlsx','Sheet1','B2:B435');
Prob=zeros(num4,1);
for j=1:num4
    if E_ph(j)<=phi_B   Prob(j)=0;
    else
        E=linspace(0,E_ph(j),num5)'; integrand=zeros(num5,1);
        row_1=interp1(E_dos_t,dos_t,-E);
        row_2=interp1(E_dos_t,dos_t,-E+E_ph(j));
        EDJDOS=row_1.*row_2;
        func_1=trapz(E,EDJDOS); point=find(E>phi_B);
        integrand(point)=EDJDOS(point);
        func_2=trapz(E,integrand); Prob(j)=func_2/func_1;
    end
end
```

```
y2=2/h^3/c^2*E_ph.^3./(exp(E_ph/kB/Ts)-1);
P_low_in=pi/2*(1-cos(2*thetaS)).*y2;  % incident power spectrum of sub-
    bandgap photons
y3=2/h^3/c^2*E_ph.^2./(exp(E_ph/kB/Ts)-1).*Prob.*abs_Au;
JL_low=q*pi/2*(1-cos(2*thetaS)).*y3;
P_low_out=JL_low.*V_opt*factor;  % Power generated by sub-bandgap
    photons
eta_high=trapz(E_high,P_high_out)/P_total;
eta_low=trapz(E_ph,P_low_out)/P_total;
eta=eta_high+eta_low;
%%%%%%%%%%%%%%%% data extrapolation %%%%%%%%%%%%%%%%
E_ph_final=linspace(min(E_ph),max(E_high),num2)';
lamda_final=h*c./E_ph_final;
P_in_final=zeros(num2,1); P_out_final=zeros(num2,1);
index=max(find(abs(E_ph_final-Eg)==min(abs(E_ph_final-Eg))));
P_in_final(1:index)=interp1(E_ph,P_low_in,E_ph_final(1:index));
P_in_final(index:num2)=interp1(E_high,P_high_in,E_ph_final(index:num2))
    ;
P_out_final(1:index)=interp1(E_ph,P_low_out,E_ph_final(1:index));
P_out_final(index:num2)=interp1(E_high,P_high_out,E_ph_final(index:num2
    ));   % Power spectrum vs photon energy
figure
plot(E_ph_final/q,P_in_final,E_ph_final/q,P_out_final);
xlabel('Photon energy (eV)'); ylabel('Power spectrum');
P_in_lamda=P_in_final.*E_ph_final.^2/h/c;
P_out_lamda=P_out_final.*E_ph_final.^2/h/c;  % Power spectrum with
    respect to wavelength
```

```
figure
plot(lamda_final*1e6,P_in_lamda,lamda_final*1e6,P_out_lamda);
xlabel('Wavelength (um)'); ylabel('Power spectrum');
%%%%%%%%%%%%%%%%%%%%%%%%%%%%%%%%%%%%%%%%%%%%%%%%%%%%%%%%%%%%%%%%%%%%%%%%%%%%
fprintf(fid,'%s\n','bandgap (eV)'); fprintf(fid,'%f\n',Eg/q);
fprintf(fid,'%s\n','Fermi level (eV)'); fprintf(fid,'%f\n',Ef/q);
fprintf(fid,'%s\n','above bandgap total efficiency'); fprintf(fid,'%f\n
    ',eta_high);
fprintf(fid,'%s\n','sub bandgap total efficiency'); fprintf(fid,'%f\n',
    eta_low);
fprintf(fid,'%s\n','sub bandgap total efficiency'); fprintf(fid,'%f\n',
    eta);
fprintf(fid,'%s\n','wavelength (um)'); fprintf(fid,'%f\n',lamda_final*1
    e6);
fprintf(fid,'%s\n','incident power spectrum'); fprintf(fid,'%f\n',
    P_in_lamda);
fprintf(fid,'%s\n','output power spectrum'); fprintf(fid,'%f\n',
    P_out_lamda);
```

## A.3 Energy Distribution of Hot Carriers in Materials

To calculate the hot carrier energy distribution, we need a xlsx file named 'data.xlsx' to store the EDOS data of different materials. These data can be calculated by quantum mechanics first principle, or can be directly cited from literature.

```
%%%%%%%%%%%%%%%%%%%%%%%%%%%%%%%%%%%%%%%%%%%%%%%%%%%%%%%%%%%%%%%%%%%%%%%%%%%%
fid=fopen('result.txt','wt');
```

```
%%%%%%%%%%%%%%%%%%% Parameters %%%%%%%%%%%%%%%%%%%%%%
h=6.626e-34; pi=3.1416; c=3e8;
q=1.6e-19; k=1.381e-23; T=300;
Ef=-5*q;  %Fermi level, this value is not important in our calculation.
    Only the relative energy to the Fermi energy will be used.
%%%%%%%%%%%%%%%%%%%%%%%%%%%%%%%%%%%%%%%%%%%%%%%%%%%%%%%%
%%%%%%%%%%%%%%%%%%%%%%%%%%%%%%%%%%%%%%%%%%%%%%%%%%%%%%%%
E=xlsread('data.xlsx','Sheet1','A2:A789')*q-Ef;  % relative energy to
    Fermi level
dos=xlsread('data.xlsx','Sheet1','C2:C789');
E_min=max(min(E),-6*q);
E_max=min(max(E),6*q);   % restrict the energy range between -6 eV to 6
    eV.
fprintf(fid,'%s\n','electron energy (eV)'); fprintf(fid,'%f\n',E/q);
fprintf(fid,'%s\n','DOS (a.u.)'); fprintf(fid,'%f\n',dos);
num2=400;
lamda=1.5e-6;    % 1.5 um photon, this value can be changed if the
    photon energy is different
E_ph=h*c/lamda;  % photon energy
fprintf(fid,'%s\n','wavelength (um)'); fprintf(fid,'%f\n',lamda*1e6);
prob_h_e=zeros(num2,1);  % transition probability for hot electrons
prob_h_h=zeros(num2,1);  % transition probability for hot holes
if E_ph<=abs(E_min)
    E_h_e=linspace(0,E_max,num2);  % valid range of the hot electron
    energy
elseif E_ph>abs(E_min) || E_ph<(E_max-E_min)
```

```
24      E_h_e=linspace(E_min+E_ph,E_max,num2);  % valid range of the hot
    electron energy
25  end
26  if E_ph<=E_max
27      E_h_h=linspace(E_min,0,num2);   % valid range of the hot hole
    energy
28  elseif E_ph>E_max || E_ph<(E_max-E_min)
29      E_h_h=linspace(E_min,E_max-E_ph,num2);   % valid range of the hot
    hole energy
30  end
31  for j=1:num2
32      index_f=max(find(abs(E-E_h_e(j))==min(abs(E-E_h_e(j)))));
33      dos_f=dos(index_f);
34      f_f=1/(exp(E_h_e(j)/k/T)+1);   % final state for hot electron
35      index_i=max(find(abs(E-E_h_e(j)+E_ph)==min(abs(E-E_h_e(j)+E_ph))));
36      dos_i=dos(index_i);
37      f_i=1/(exp((E_h_e(j)-E_ph)/k/T)+1);   % intial state for hot
    electron
38      prob_h_e(j)=dos_i*f_i*dos_f*(1-f_f);
39      index_i=max(find(abs(E-E_h_h(j))==min(abs(E-E_h_h(j)))));
40      dos_i=dos(index_i);
41      f_i=1/(exp(E_h_h(j)/k/T)+1);   % intial state for hot hole
42      index_f=max(find(abs(E-E_h_h(j)-E_ph)==min(abs(E-E_h_h(j)-E_ph))));
43      dos_f=dos(index_f);
44      f_f=1/(exp((E_h_h(j)+E_ph)/k/T)+1);  % final state for hot hole
45      prob_h_h(j)=dos_i*f_i*dos_f*(1-f_f);
46  end
```

```
norm_e=max(prob_h_e); norm_h=max(prob_h_h);
norm=max(norm_e,norm_h); prob_h_e=prob_h_e/norm;
prob_h_h=prob_h_h/norm;   % normalize the distribution function
fprintf(fid,'%s\n','hot electron energy for 1.5 um (eV)');
fprintf(fid,'%f\n',E_h_e/q);
fprintf(fid,'%s\n','hot electron distribution for 1.5 um (a.u.)');
fprintf(fid,'%f\n',prob_h_e);
fprintf(fid,'%s\n','hot hole energy for 1.5 um (eV)');
fprintf(fid,'%f\n',E_h_h/q);
fprintf(fid,'%s\n','hot hole distribution for 1.5 um (a.u.)');
fprintf(fid,'%f\n',prob_h_h);
```

## A.4 Metamaterial Parameter Retrieval

### A.4.1 Lumerical FDTD Simulation to Obtain Scattering Parameters

```
%%%%%%%%%%%%%%%%%%%%%%%%%%%%%%%%%%%%%%%%%%%%%%%%%%%%%%%%%%%%%%%%%%%%%%%%%%%%
run;  % run the simulation
f=getdata("profile","f");   % get the frequency of the light source
nf=length(f);
select("::model");
diam_1=get("diam_1"); diam_2=get("diam_2");
d=diam_1+(diam_2-diam_1)/2;  % Effective thickness of the SRR
%source position%=getdata("source","y"); m="T_point";
refractive_index_1=getdata("R_index","index_x");
refractive_index_2=getdata("T_index","index_x");
k1=2*pi*pinch(refractive_index_1)*f/c;
```

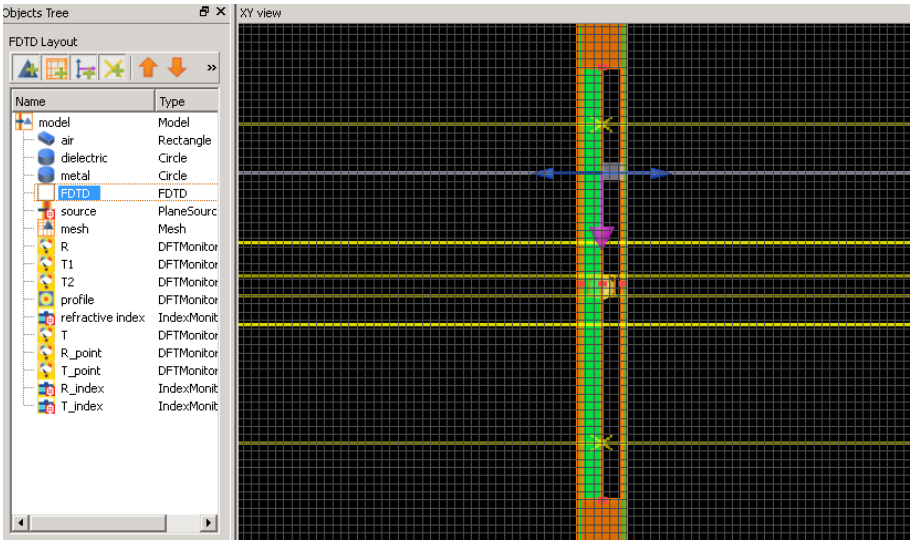


Figure A.2: Lumerical FDTD simulation region of the SRR fiber. Light is incident from above, from which the forward scattering parameters can be obtained.

```
12 k2=2*pi*pinch(refractive_index_2)*f/c;
13 k=2*pi*f/c;
14 %%% Get the largest field component, it will be used to calculate the S
       parameters %%%
15 Ex2=sum(abs(getdata("T_point","Ex"))^2+abs(getdata("R_point","Ex"))^2);
16 Ey2=sum(abs(getdata("T_point","Ey"))^2+abs(getdata("R_point","Ey"))^2);
17 Ez2=sum(abs(getdata("T_point","Ez"))^2+abs(getdata("R_point","Ez"))^2);
18 component=find([Ex2,Ey2,Ez2],max([Ex2,Ey2,Ez2]));
19 if(component==1) {field_component="Ex";}
20 if(component==2) {field_component="Ey";}
21 if(component==3) {field_component="Ez";}
22 %%%%%%%%%%%%%%%%%%%%%%%%%%%%%%%%%%%%%%%%%%%%%%%%%%%%%%%%%%%%%%%%%%%%%%%%
23 %%%%%%%%%%%%%%%%%% S parameters calculation %%%%%%%%%%%%%%%%%
24 mon_position=getdata("T_point","y");  % position of the T monitor
```

```
25 propagation_length1=%source position%-d;   % distance between source
       and the MM
26 propagation_length2=-mon_position;  % distance between the MM and T
       monitor
27 propagation_phase=k1*propagation_length1+k2*propagation_length2;   %
       calculate accumulated phase from propagation length
28
29 S11=getdata(m,field_component);  % denote represent t+ in S matrix
30 S11=pinch(S11)*exp(-1i*propagation_phase);
31 m="R_point";
32 mon_position=getdata("R_point","y");   % position of the R monitor
33 propagation_length=%source position%-d+mon_position-d;
34 propagation_phase=k1*propagation_length;  % calculate wave vector from
       length
35 S21=getdata(m,field_component);
36 S21=pinch(S21)*exp(-1i*propagation_phase);   % represent r- in S matrix
37 plot(c/f*1e6,abs(S11),abs(S21),"wavelength/um","abs(S)","S parameters")
       ;
38 legend("|S11| (t+)","|S21| (r-)");
39 write("result.txt","Re(S11)");
40 write("result.txt",num2str(real(S11)));
41 write("result.txt","Im(S11)");
42 write("result.txt",num2str(imag(S11)));
43 write("result.txt","Re(S21)");
44 write("result.txt",num2str(real(S21)));
45 write("result.txt","Im(S21)");
46 write("result.txt",num2str(imag(S21)));   % record the amplitudes and
```

```
    phases of the S-parameters
switchtolayout;
%%%%%%%%%%%%%%%%%%%%%%%%%%%%%%%%%%%%%%%%%%%%%%%%%%%%%%%%%%%%%%%%%%%%%%%%%%%%
```

Similarly, another two S-parameters (S12,S22) can be retrieved from the simulation where light is incident from the backside. The compelete S-parameters should be stored in an xlsx file named 'bianisotropic.xlsx'. The S-parameters will be used in retrieving the effective parameters of an bianisotropic SRR.

### A.4.2 MATLAB code for the Parameter Retrieval

```
fid=fopen('result.txt','wt');
lamda=xlsread('bianisotropic.xlsx','Sheet1','A2:A301')*10^(-6);
k=xlsread('bianisotropic.xlsx','Sheet1','B2:B301');
d=250*10^(-9);   % The thickness of the SRR in this case
S11=xlsread('bianisotropic.xlsx','Sheet1','D2:D301')+1i*xlsread('
    bianisotropic.xlsx','Sheet1','E2:E301');
S21=xlsread('bianisotropic.xlsx','Sheet1','G2:G301')+1i*xlsread('
    bianisotropic.xlsx','Sheet1','H2:H301');
S12=xlsread('bianisotropic.xlsx','Sheet1','J2:J301')+1i*xlsread('
    bianisotropic.xlsx','Sheet1','K2:K301');
S22=xlsread('bianisotropic.xlsx','Sheet1','M2:M301')+1i*xlsread('
    bianisotropic.xlsx','Sheet1','N2:N301');
%%%%%%%% Read the S-parameters from the xlsx file%%%%%%%%%%%%%%%
%%%%%%%%%%%%%%% Calculate the effective parameters %%%%%%%%%%%%%%%
trans=1./(2*S11).*(1-S21.*S12+S11.^2);
n1=(-1i*log(trans+1i*sqrt(1-trans.^2)))./(k*d);
n2=(-1i*log(trans-1i*sqrt(1-trans.^2)))./(k*d);
```

```
fprintf(fid,'%s\n','wavelength_um)'); fprintf(fid,'%f\n',lamda*1e6);
refra=(imag(n1)>=0).*n1+(imag(n1)<0).*n2;
ksi=-(refra./(2*sin(refra.*k*d))).*((S21-S12)./S11);
mu_eff=(1i*refra./sin(refra.*k*d)).*((2+S21+S12)./(2*S11)-cos(refra.*k*
    d)); % Permeability
eps_eff=(refra.^2+ksi.^2)./mu_eff; % Permittivity
z_plus=mu_eff./(refra+1i*ksi);
z_minus=mu_eff./(refra-1i*ksi); % The impedance in two directions are
     different
figure(1)
fprintf(fid,'%s\n','Re(n)'); fprintf(fid,'%f\n',real(refra));
fprintf(fid,'%s\n','Im(n)'); fprintf(fid,'%f\n',imag(refra));
plot(lamda*1e6,real(refra),lamda*1e6,imag(refra));
xlabel('wavelength/um'); ylabel('n');
legend('real','imag');
figure(2)
fprintf(fid,'%s\n','Re(mu)'); fprintf(fid,'%f\n',real(mu_eff));
fprintf(fid,'%s\n','Im(u)'); fprintf(fid,'%f\n',imag(mu_eff));
plot(lamda*1e6,real(mu_eff),lamda*1e6,imag(mu_eff));
xlabel('wavelength/um');ylabel('mu');
legend('real','imag');
figure(3)
fprintf(fid,'%s\n','Re(eps)'); fprintf(fid,'%f\n',real(eps_eff));
fprintf(fid,'%s\n','Im(eps)'); fprintf(fid,'%f\n',imag(eps_eff));
plot(lamda*1e6,real(eps_eff),lamda*1e6,imag(eps_eff));
xlabel('wavelength/um'); ylabel('eps');
legend('real','imag');
```

```
figure(4)
fprintf(fid,'%s\n','Re(ksi)'); fprintf(fid,'%f\n',real(ksi));
fprintf(fid,'%s\n','Im(ksi)'); fprintf(fid,'%f\n',imag(ksi));
plot(lamda*1e6,real(ksi),lamda*1e6,imag(ksi));
xlabel('wavelength/um'); ylabel('ksi');
legend('real','imag');
figure(5)
fprintf(fid,'%s\n','Re(z+)'); fprintf(fid,'%f\n',real(z_plus));
fprintf(fid,'%s\n','Im(z+)'); fprintf(fid,'%f\n',imag(z_plus));
plot(lamda*1e6,real(z_plus),lamda*1e6,imag(z_plus));
xlabel('wavelength/um'); ylabel('z+');
legend('real','imag');
figure(6)
fprintf(fid,'%s\n','Re(z-)'); fprintf(fid,'%f\n',real(z_minus));
fprintf(fid,'%s\n','Im(z-)'); fprintf(fid,'%f\n',imag(z_minus));
plot(lamda*1e6,real(z_minus),lamda*1e6,imag(z_minus));
xlabel('wavelength/um'); ylabel('z-');
legend('real','imag');
```

# Bibliography


[1] P. Berini and I. De Leon, "Surface plasmon-polariton amplifiers and lasers," Nat. Photon. **6**, 16-24 (2012).

[2] R.-M. Ma, R. F. Oulton, V. J. Sorger and X. Zhang, "Plasmon lasers: coherent light source at molecular scales," Laser Photon. Rev. **7**, 1-21 (2013).

[3] O. Hess, J. B. Pendry, S. A. Maier, R. F. Oulton, J. M. Hamm and K. L. Tsakmakidis, "Active nanoplasmonic metamaterials," Nat. Mater. **11**, 573-584 (2012).

[4] J. N. Anker, W. P. Hall, O. Lyandres, N. C. Shah, J. Zhao, R. P. Van Duyne, "Biosensing with plasmonic nanosensors," Nat. Mater. **7**, 442-453 (2008).

[5] V. Giannini, A. I. Fernandez-Dominguez, S. C. Heck and S. A. Maier, "Plasmonic nanoantennas: fundamentals and their use in controlling the radiative properties of nanoemitters," Chem. Rev. **111**, 3888-3912 (2011).

[6] J. Lin, J. P. B. Mueller, Q. Wang, G. Yuan, N. Antoniou, X.-C. Yuan and F. Capasso, "Polarization-controlled tunable directional coupling of surface plasmon polaritons," Science **340**, 331-334 (2013).

[7] N. Yu, Q. Wang and F. Capasso, "Beam engineering of quantum cascade lasers," Laser Photon. Rev. **6**, 24-46 (2012).

[8] P. Fan, C. Colombo, K. C. Y. Huang, P. Krogstrup, J. Nygrd, A. F. Morral and M. L. Brongersma, "An electrically-driven GaAs nanowire surface plasmon source," Nano Lett. **12**, 4943-4947 (2012).

[9] K. Diest, J. A. Dionne, M. Spain and H. A. Atwater, "Tunable color filters based on metal-insulator-metal resonators," Nano Lett. **9**, 2579-2583 (2009).

[10] K. Diest, V. Liberman, D. M. Lennon, P. B. Welander and M. Rothschild, "Aluminum plasmonics: optimization of plasmonic properties using liquid-prism-coupled ellipsometry," Opt. Express **21**, 28638-28650 (2013).

[11] J. A. Dionne, K. Diest, L. A. Sweatlock and H. A. Atwater, "PlasMOStor: a metal-oxide-Si field effect plasmonic modulator," Nano Lett. **9**, 897-902 (2009).

[12] S. P. Burgos, S. Yokogawa and H. A. Atwater, "Color imaging via nearest neighbor hole coupling in plasmonic color filters integrated onto a complementary metal-oxide semiconductor image sensor," ACS Nano **7**, 10038-10047 (2013).

[13] N. Engheta, A. Salandrino and A. Alu, "Circuit elements at optical frequencies: nanoinductors, nanocapacitors, and nanoresistors," Phys. Rev. Lett. **95**, 095504 (2005).

[14] A. Alu and N. Engheta, "Tuning the scattering response of optical nanoantennas with nanocircuit loads," Nat. Photon. **2**, 307-310 (2008).

[15] M. W. Knight, L. Liu, Y. Wang, L. Brown, S. Mukherjee, N. S. King, H. O. Everitt, P. Nordlander and N. J. Halas, "Aluminum plasmonic nanoantennas," Nano Lett. **12**, 6000-6004 (2012).

[16] L. Zhou *et al.*, "Aluminum nanocrystals as a plasmonic photocatalyst for hydrogen dissociation," Nano Lett. **16**, 1478-1484 (2016).

[17] C. F. Bohren and D. R. Huffman, *Absorption and Scattering of Light by Small Particles* (John Wiley and Sons, Hoboken, NJ, 1983).

[18] C. Kittel, *Introduction to Solid State Physics (8th ed.)* (John Wiley and Sons, Hoboken, NJ, 1996).

[19] M. G. Cottam, *Introduction to Surface and Superlattice Excitations* (Cambridge University Press, New York, 1989).

[20] G. V. Hartland, "Optical studies of dynamics in noble metal nanostructures," Chem. Rev. **111**, 3858-3887 (2011).

[21] E. A. Coronado and G. C. Schatz, "Surface plasmon broadening for arbitrary shape nanoparticles: a geometrical probability approach," J. Chem. Phys. **119**, 3926 (2003).

[22] R. A. Millikan, "A direct photoelectric determination of Planck's "h"," Phys. Rev. **7**, 355-388 (1916).

[23] F. W. Bubb, "Direction of ejection of photo-electrons by polarized X-rays," Phys. Rev. **23**, 137-143 (1924).

[24] J. G. Endriz and W. E. Spicer, "Surface-plasmon-one-electron decay and its observation in photoemission," Phys. Rev. Lett. **24**, 64-68 (1970).

[25] K. H. Gundlach and J. Kadlec, "Interfacial barrier height measurement from voltage dependence of the photocurrent," J. Appl. Phys. **46**, 5286-5287 (1975).

[26] A. M. Brown, R. Sundararaman, P. Narang, W. A. Goddard and H. A. Atwater, "Nonradiative plasmon decay and hot carrier dynamics: effects of phonons, surfaces, and geometry," ACS Nano **10**, 957-966 (2016).

[27] P. Narang, R. Sundararaman and H. A. Atwater, "Plasmonic hot carrier dynamics in solid-state and chemical systems for energy conversion," Nanophoton. doi:10.1515/nanoph-2016-0007 (2016).

[28] O. Demichel, M. Petit, S. Viarbitskaya, R. Mjard, F. de Fornel, E. Hertz, F. Billard, A. Bouhelier and B. Cluzel, "Dynamics, efficiency, and energy distribution of nonlinear plasmon-assisted generation of hot carriers," ACS Photon. **3**, 791-795 (2016).

[29] S. Mubeen, J, Lee, N. Singh, S. Krmer, G. D. Stucky and M. Moskovits, "An autonomous photosynthetic device in which all charge carriers derive from surface plasmons," Nat. Nanotechnol. **8**, 247-251 (2013).

[30] P. Christopher, H. Xin, A. Marimuthu and S. Linic, "Singular characteristics and unique chemical bond activation mechanisms of photocatalytic reactions on plasmonic nanostructures," Nat. Mater. **11**, 1044-1050 (2012).

[31] S. Mukherjee, F. Libisch, N. Large, O. Neumann, L. V. Brown, J. Cheng, J. B. Lassiter, E. A. Carter, P. Nordlander and N. J. Halas, "Hot electrons do the impossible: plasmon-induced dissociation of $H_2$ on Au," Nano Lett. **13**, 240-247 (2013).

[32] J. Lee, S. Mubeen, X. Ji, G. D. Stucky and M. Moskovits, "Plasmonic photoanodes for solar water splitting with visible light," Nano Lett. **12**, 5014-5019 (2012).

[33] N. Noginova, A. V. Yakim, J. Soimo, L. Gu and M. A. Noginov, "Light-to-current and current-to-light coupling in plasmonic systems," Phys. Rev. B **84**, 035447 (2011).

[34] W. Wang, A. Klots, D. Prasai, Y. Yang, K. I. Bolotin and J. Valentine, "Hot electron-based near-infrared photodetection using bilayer $MoS_2$," Nano Lett. **15**, 7440-7444 (2015).

[35] A. Giugni, B. Torre, A. Toma, M. Francardi, M. Malerba, A. Alabastri, R. Proietti Zaccaria, M. I. Stockman and E. Di Fabrizio, "Hot-electron nanoscopy using adiabatic compression of surface plasmons," Nat. Nanotechnol. **8**, 845-852 (2013).

[36] J. M. Stern, J. Stanfield, W. Kabbani, J. T. Hsieh and J. R. A. Cadeddu, "Selective prostate cancer thermal ablation with laser activated gold nanoshells," J. Urology **179**, 748-753 (2008).

[37] O. Neumann, A. S. Urban, J. Day, S. Lal, P. Nordlander and N. J. Halas, "Solar vapor generation enabled by nanoparticles," ACS Nano **7**, 42-49 (2013).

[38] Y. Kang *et al.*, "Plasmonic hot electron induced structural phase transition in a $MoS_2$ monolayer," Adv. Mater. **26**, 6467-6471 (2014).

[39] C. D. Lindstrom and X.-Y. Zhu, "Photoinduced electron transfer at molecule-metal interfaces," Chem. Rev. **106**, 4281-4300 (2006).

[40] S. Saeed, E. M. L. D. de Jong, K. Dohnalova and T. Gregorkiewicz, "Efficient optical extraction of hot-carrier energy," Nat. Commun. **5**, 4665 (2014).

[41] M. A. Green, K. Emery, Y. Hishikawa, W. Warta and E. D. Dunlop, "Solar cell efficiency tables (version 43)," Prog. Photovolt. **22**, 1-9 (2014).

[42] L. C. Hirst and N. J. Ekins-Daukes, "Fundamental losses in solar cells," Prog. Photovolt. **19**, 286-293 (2011).

[43] T. G. J. Olson and M. Al-Jassim, "$GaInP_2$/GaAs-a current- and lattice-matched tandem cell with an high theoretical efficiency," in Proc.18th IEEE Photovolt. Spec. Conf. pp.552-555, New York (1985).

[44] H. Cotal, C. Fetzer, J. Boisvert, G. Kinsey, R. King, P. Hebert, H. Yoon and N. Karam, "III-V multijunction solar cells for concentrating photovoltaics," Energy Environ. Sci. **2**, 174-192 (2009).

[45] K. A. Bertness, S. R. Kurtz, D. J. Friedman, A. E. Kibbler, C. Kramer and J. M. Olson, "29.5%-efficient GaInP/GaAs tandem solar cells," Appl. Phys. Lett. **65**, 989-991 (1994).

[46] A. Luque, "Will we exceed 50% efficiency in photovoltaics?" J. Appl. Phys. **110**, 031301 (2011).

[47] J. M. Olson, S. R. Kurtz, A. E. Kibbler and P. Faine, "A 27.3% efficient $Ga_0.5In_0.5P$/GaAs tandem solar cell," Appl. Phys. Lett. **56**, 623-625 (1990).

[48] R. R. King, D. C. Law, K. M. Edmondson, C. M. Fetzer, G. S. Kinsey, H. Yoon, R. A. Sherif and N. H. Karam, "40% efficient metamorphic GaInP/GaInAs/Ge multijunction solar cells," Appl. Phys. Lett. **90**, 183516 (2007).

[49] J. F. Geisz, Sarah Kurtz, M. W. Wanlass, J. S. Ward, A. Duda, D. J. Friedman, J. M. Olson, W. E. McMahon, T. E. Moriarty and J. T. Kiehl, "High-efficiency GaInP/GaAs/InGaAs triple-junction solar cells grown inverted with a metamorphic bottom junction," Appl. Phys. Lett. **91**, 023502 (2007).

[50] R. R. King *et al.*, "Solar cell generations over 40% efficiency," Prog. Photovolt. **20**, 801-815 (2012).

[51] Record efficiency reported as of June 14, 2016: http://www.nrel.gov/ncpv/images/efficiency_chart.jpg.

[52] M. S. Leite, R. L. Woo, J. N. Munday, W. D. Hong, S. Mesropian, D. C. Law and H. A. Atwater, "Towards an optimized all lattice-matched InAlAs/InGaAsP/InGaAs multijunction solar cell with efficiency >50%," Appl. Phys. Lett. **102**, 033901 (2013).

[53] J. N. Munday and H. A. Atwater, "Large integrated absorption enhancement in plasmonic solar cells by combining metallic gratings and antireflection coatings," Nano Lett. **11**, 2195-2201 (2011).

[54] I. Zoric, M. Zach, B. Kasemo and C. Langhammer, "Gold, platinum, and aluminum nanodisk plasmons: material independence, subradiance, and damping mechanisms," ACS Nano **5**, 2535-2546 (2011).

[55] C. Delerue, G. Allan, J. J. H. Pijpers and M. Bonn, "Carrier multiplication in bulk and nanocrystalline semiconductors: mechanism, efficiency, and interest for solar cells," Phys. Rev. B **81**, 125306 (2010).

[56] J. B. Sambur, T. Novet and B. A. Parkinson, "Multiple exciton collection in a sensitized photovoltaic system," Science **330**, 63-66 (2010).

[57] V. Sukhovatkin, S. Hinds, L. Brzozowski and E. H. Sargent, "Colloidal quantum-dot photodetectors exploiting multiexciton generation," Science **324**, 1542-1544 (2009).

[58] P. Wurfel, "Solar energy conversion with hot electrons from impact ionisation," Sol. Energy Mater. Sol. **46**, 43-52 (1997).

[59] P. Aliberti, Y. Feng, Y. Takeda, S. K. Shrestha, M. A. Green and G. Conibeer, "Investigation of theoretical efficiency limit of hot carriers solar cells with a bulk indium nitride absorber," J. Appl. Phys. **108**, 094507 (2010).

[60] G.J. Conibeer, C.-W. Jiang, D. Knig, S. Shrestha, T. Walsh and M.A. Green, "Selective energy contacts for hot carrier solar cells," Thin Solid Films **516**, 6968-6973 (2008).

[61] D. J. Farrell, Y. Takeda, K. Nishikawa, T. Nagashima, T. Motohiro and N. J. Ekins-Daukes, "A hot-carrier solar cell with optical energy selective contacts," Appl. Phys. Lett. **99**, 111102 (2011).

[62] K. Kempa, M. J. Naughton, Z. F. Ren, A. Herczynski, T. Kirkpatrick, J. Rybczynski and Y. Gao, "Hot electron effect in nanoscopically thin photovoltaic junctions," Appl. Phys. Lett. **95**, 233121 (2009).

[63] D. J. Farrell, H. Sodabanlu, Y. Wang, M. Sugiyama and Y. Okada, "Can a hot-carrier solar cell also be an efficient up-converter?" IEEE J. Photovolt. **5**, 571-576 (2015).

[64] L. R. Canfield, R. E. Vest, R. Korde, H. Schmidtke and R. Desor, "Absolute silicon photodiodes for 160 nm to 254 nm photons," IEEE J. Photovolt. **5**, 571-576 (2015).

[65] G. Maidecchi *et al.*, "Deep ultraviolet plasmon resonance in aluminum nanoparticle arrays," ACS Nano **7**, 5834-5841 (2013).

[66] S. M. Sze, *Physics of Semiconductor Devices* (Wiley-Interscience, Hoboken, NJ, 1981).

[67] C. Henry, "Limiting efficiencies of ideal single and multiple energy gap terrestrial solar cells," J. Appl. Phys. **51**, 4494 (1980).

[68] A. Luque and S. Hegedus, *Handbook of Photovoltaic Science and Engineering* (John Wiley and Sons, Hoboken, NJ, 2011).

[69] S. Kurtz and J. Geisz, "Multijunction solar cells for conversion of concentrated sunlight to electricity," Opt. Express **18**, A73-A78 (2010).

[70] O. E. Semonin, J. M. Luther, S. Choi, H.-Y. Chen, J. Gao, A. J. Nozik and M. C. Beard, "Peak external photocurrent quantum efficiency exceeding 100% via MEG in a quantum dot solar cell," Science **334**, 1530-1533 (2011).

[71] R. E. Blankenship *et al.*, "Comparing photosynthetic and photovoltaic efficiencies and recognizing the potential for improvement," Science **332**, 805-809 (2011).

[72] M. C. Beard, A. G. Midgett, M. C. Hanna, J. M. Luther, B. K. Hughes and A. J. Nozik, "Comparing multiple exciton generation in quantum dots to impact ionization in bulk semiconductors: implications for enhancement of solar energy conversion," Nano Lett. **10**, 3019-3027 (2010).

[73] M. C. Hanna and A. J. Nozik, "Solar conversion efficiency of photovoltaic and photoelectrolysis cells with carrier multiplication absorbers," J. Appl. Phys. **100**, 074510-074518 (2006).

[74] J. A. McGuire, M. Sykora, J. Joo, J. M. Pietryga and V. I. Klimov, "Apparent versus true carrier multiplication yields in semiconductor nanocrystals," Nano Lett. **10**, 2049-2057 (2010).

[75] J. A. McGuire, J. Joo, J. M. Pietryga, R. D. Schaller and V. I. Klimov, "New aspects of carrier multiplication in semiconductor nanocrystals," Acc. Chem. Res. **41**, 1810-1819 (2008).

[76] R. T. Ross and A. J. Nozik, "Efficiency of hot-carrier solar energy converters," J. Appl. Phys. **53**, 3813-3818 (1982).

[77] Y. Takeda, T. Ito, T. Motohiro, D. Konig, S. Shrestha and G. Conibeer, "Hot carrier solar cells operating under practical conditions," J. Appl. Phys. **105**, 074905 (2009).

[78] W. A. Tisdale, K. J. Williams, B. A. Timp, D. J. Norris, E. S. Aydil and X.-Y. Zhu, "Hot-electron transfer from semiconductor nanocrystals," Science **328**, 1543-1547 (2010).

[79] M. W. Knight, H. Sobhani, P. Nordlander and N. J. Halas, "Photodetection with active optical antennas," Science **332**, 702-704 (2011).

[80] M. W. Knight, Y. Wang, A. S. Urban, A. Sobhani, B. Y. Zheng, P. Nordlander and N. J. Halas, "Embedding plasmonic nanostructure diodes enhances hot electron emission," Nano Lett. **13**, 1687-1692 (2013).

[81] A. Sobhani, M. W. Knight, Y. Wang, B. Y. Zheng, N. S. King, L. V. Brown, Z. Fang, P. Nordlander and N. J. Halas, "Narrowband photodetection in the near-infrared with a plasmon-induced hot electron device," Nat. Commun. **4**, 1643 (2013).

[82] C. Clavero, "Plasmon-induced hot-electron generation at nanoparticle/metal-oxide interfaces for photovoltaic and photocatalytic devices," Nat. Photon. **8**, 95-103 (2014).

[83] W. Li and J. Valentine, "Metamaterial perfect absorber based hot electron photodetection," Nano Lett. **14**, 3510-3514 (2014).

[84] P. Reineck, G. P. Lee, D. Brick, M. Karg, P. Mulvaney and U. Bach, "A solid-state plasmonic solar cell via metal nanoparticle self-assembly," Adv. Mater. **24**, 4750-4755 (2012).

[85] Y. Nishijima, K. Ueno, Y. Yokota, K. Murakoshi and H. Misawa, "Plasmon-assisted photocurrent generation from visible to near-infrared wavelength using a Au-nanorods/$TiO_2$ electrode," J. Phys. Chem. Lett. **1**, 2031-2036 (2010).

[86] Y. Takahashi and T. Tatsuma, "Solid state photovoltaic cells based on localized surface plasmon-induced charge separation," Appl. Phys. Lett. **99**, 182110 (2011).

[87] A. Manjavacas, J. G. Liu, V. KulKarni and P. Nordlander, "Plasmon-induced hot carriers in metallic nanoparticles," ACS Nano **8**, 7630-7638 (2014).

[88] Y. Tian, X. Shi, C. Lu, X. Wang and S. Wang, "Charge separation in solid-state gold nanoparticles-sensitized photovoltaic cell," Electrochem. Commun. **11**, 1603-1605 (2009).

[89] S. Grover and G. Moddel, "Applicability of metal/insulator/metal (MIM) diodes to solar rectennas," IEEE J. Photovolt. **1**, 78-83 (2011).

[90] W. Brown, "The history of power transmission by radio-waves," IEEE Trans. Microw. Theory Techn. **32**, 1230-1242 (1984).

[91] D. Ward, F. Huser, F. Pauly, J. Cuevas and D. Natelson, "Optical rectification and field enhancement in a plasmonic nanogap," Nat. Nanotechnol. **5**, 732-736 (2010).

[92] F. Wang and N. A. Melosh, "Plasmonic energy collection through hot carrier extraction," Nano Lett. **11**, 5426-5430 (2011).

[93] D. A. Kovacs, J. Winter, S. Meyer, A. Wucher and D. Diesing, "Photo and particle induced transport of excited carriers in thin film tunnel junctions," Phys. Rev. B **76**, 235408 (2007).

[94] T. P. White and K. R. Catchpole, "Plasmon-enhanced internal photoemission for photovoltaics: theoretical efficiency limits," Appl. Phys. Lett. **101**, 073905 (2012).

[95] C. N. Berglund and W. E. Spicer, "Photoemission studies of copper and silver: theory," Phys. Rev. **136**, A1030-A1044 (1964).

[96] C. Scales and P. Berini, "Thin-film Schottky barrier photodetector models," IEEE J. Quantum Electron. **46**, 633-643 (2010).

[97] K. W. Shepard, "Photocurrents through thin films of $Al_2O_3$," J. Appl. Phys. **36**, 796-799 (1965).

[98] D. R. Jennison, P. A. Schultz and J. P. Sullivan, "Evidence for interstitial hydrogen as the dominant electronic defect in nanometer alumina films," Phys. Rev. B **69**, 041405 (2004).

[99] E. Y. Chan, H. C. Card and M. C. Teich, "Internal photoemission mechanisms at interfaces between germanium and thin metal films," IEEE J. Quantum Electron. **16**, 373-381 (1980).

[100] A. I. Braunstein, M. Braunstein and G. S. Picus, "Hot-electron attenuation in thin $Al_2O_3$ films," Phys. Rev. Lett. **15**, 956-958 (1965).

[101] J. G. Simmons, "Generalized formula for electric tunnel effect between similar electrodes separated by a thin insulating film," J. Appl. Phys. **34**, 1793-1803 (1963).

[102] C. Voisin, N. Del Fatti, D. Christofilos and F. Vallee, "Ultrafast electron dynamics and optical nonlinearities in metal nanoparticles," J. Phys. Chem. B **105**, 2264-2280 (2001).

[103] S. V. Pammi, A. Chanda, J.-K. Ahn, J.-H. Park, C.-R. Cho, W.-J. Lee and S.-G. Yoon, "Low resistivity ITO thin films deposited by NCD technique at low temperature: variation of tin concentration," J. Electrochem. Soc. **157**, H937-H941 (2010).

[104] J. Bellingham, W. Phillips and C. Adkins, "Electrical and optical-properties of amorphous indium oxide," J. Phys.- Condens. Mat. **2**, 6207-6221 (1990).

[105] H. Chalabi, D. Schoen and M. L. Brongersma, "Hot-electron photodetection with a plasmonic nanostripe antenna," Nano Lett. **14**, 1374-1380 (2014).

[106] A. Slepko and A. Demkov, "Band engineering in silicide alloys," Phys. Rev. B **85**, 035311 (2012).

[107] P. Kamat, "Quantum dot solar cells. semiconductor nanocrystals as light harvesters," J. Phys. Chem. C **112**, 18737-18753 (2008).

[108] F. Wang and N. A. Melosh, "Power-independent wavelength determination by hot carrier collection in metal-insulatormetal devices," Nat. Commun. **4**, 1711 (2013).

[109] E. W. Cowell, S. W. Muir, D. A. Keszler and J. F. Wager, "Barrier height estimation of asymmetric metal-insulator-metal tunneling diodes," J. Appl. Phys. **114**, 213703 (2013).

[110] Y. Skarlatos, R. Barker and A. Yelon, "Traps in $Al_2O_3$ detected by tunneling," J. Appl. Phys. **47**, 4593-4597 (1976).

[111] B. Ealet, M. Elyakhloufi, E. Gillet and M. Ricci, "Electronic and crystallographic structure of gamma-alumina thin-films," Thin Solid Films **250**, 92-100 (1994).

[112] R. T. Tung, "The physics and chemistry of the Schottky barrier height," Appl. Phys. Rev. **1**, 011304 (2014).

[113] Z. Burshtein and J. Levinson, "Photo-induced tunnel currents in Al-$Al_2O_3$-Au structures," Phys. Rev. B **12**, 3453-3457 (1975).

[114] M. L. Brongersma, N. J. Halas and P. Nordlander, "Plasmon-induced hot carrier science and technology," Nat. Nanotechnol. **10**, 25-34 (2015).

[115] F. P. G. de Arquer, A. Mihi and G. Konstantatos, "Large-area plasmonic-crystal-hot-electron-based photodetectors," ACS Photon. **2**, 950-957 (2015).

[116] H. A. Atwater, "The promise of plasmonics," Sci. Am. **296**, 56-63 (2007).

[117] M. J. Mendes, A. Luque, I. Tobias and A. Marti, "Plasmonic light enhancement in the near-field of metallic nanospheroids for application in intermediate band solar cells," Appl. Phys. Lett. **95**, 071105 (2009).

[118] R. Sundararaman, P. Narang, A. S. Jermyn, W. A. Goddard III and H. A. Atwater, "Theoretical predictions for hot-carrier generation from surface plasmon decay," Nat. Commun. **5**, 5788 (2014).

[119] M. K. Hedayati, F. Faupel and M. Elbahri, "Review of plasmonic nanocomposite metamaterial absorber," Materials **7**, 1221-1248 (2014).

[120] J. A. Bossard, L. Lin, S. Yun, L. Liu, D. H. Werner and T. S. Mayer, "Near-ideal optical metamaterial absorbers with super-octave bandwidth," ACS Nano **8**, 1517-1524 (2014).

[121] J. Spitaler and L. Pardini, "Electronic-Structure Calculations," http://exciting-code.org/beryllium-electronic-structure-calculations.

[122] L. H. Bennett, *Electronic Density of States: Based on Invited and Contributed Papers and Discussion* (U.S. National Bureau of Standards, 1971).

[123] F. Pauly, J. K. Viljas, U. Huniar, M. Hafner, S. Wohlthat, M. Burkle, J. C. Cuevas and G. Schon, "Cluster-based density-functional approach to quantum transport through molecular and atomic contacts," New J. Phys. **10**, 125019 (2008).

[124] D. R. Mason, C. P. Race, M. H. F. Foo, A. P. Horsfield, W. M. C. Foulkes and A. P. Sutton, "Resonant charging and stopping power of slow channelling atoms in a crystalline metal," New J. Phys. **14**, 073009 (2012).

[125] K. Krupski, M. Moors, P. Jozwik, T. Kobiela and A. Krupski, "Structure determination of Au on Pt(111) surface: LEED, STM and DFT Study," Materials **8**, 2935-2952 (2015).

[126] M. Jafari, H. Jamnezhad and L. Nazarzadeh, "Electronic properties of titanium using density functional theory," Iranian J. Sci. and Tech. **36**, 511-515 (2012).

[127] S. Kanagaprabha, A. T. Asvinimeenaatci, G. Sudhapriyanga, A. JemmyCinthia, R. Rajeswarapalanichamy and K. Iyakutti, "First principles study of stability and electronic structure of TMH and $TMH_2$ (TM = Y, Zr, Nb)," Acta Physica Polonica A **123**, 126-131 (2013).

[128] M. A. Ortigoza and T. S. Rahman, "First principles calculations of the electronic and geometric structure of $Ag_27Cu_7$ Nanoalloy," Phys. Rev. B **77**, 195404 (2008).

[129] A. Kumar and D. P. Ojha, "Electrical transport and electronic structure calculation of Al-Ga binary alloys," Acta Physica Polonica A **119**, 408-415 (2011).

[130] V. Fournee, I. Mazin, D. A. Papaconstantopoulos and E. Belin-Ferre, "Electronic structure calculations of Al-Cu alloys: comparison with experimental results on Hume-Rothery phases," Philos. Mag. B **79**, 205-221 (1999).

[131] A. Kumar, D. Banyai, P. K. Ahluwalia, R. Pandey and S. P. Karna, "Electronic stability and electron transport properties of atomic wires anchored on the $MoS_2$ monolayer," Phys. Chem. Chem. Phys. **16**, 20157-20163 (2014).

[132] E. Faizabadi, "Single wall carbon nanotubes in the presence of vacancies and related energy gaps," *Electronic Properties of Carbon Nanotubes*, J. M. Marulanda, ed. (Intech, 2011).

[133] K. Nakada and A. Ishii, "DFT calculation for Adatom adsorption on graphene," *Graphene Simulation*, J. R. Gong, ed. (Intech, 2011).

[134] A. J. Leenheer, P. Narang, N. S. Lewis and H. A. Atwater, "Solar energy conversion via hot electron internal photoemission in metallic nanostructures: efficiency estimates," J. Appl. Phys. **115**, 134301 (2014).

[135] A. O. Govorov and H. Zhang, "Kinetic density functional theory for plasmonic nanostructures: breaking of the plasmon peak in the quantum regime and generation of hot electrons," J. Phys. Chem. C **119**, 6181-6194 (2015).

[136] K. J. Tielrooij, M. Massicotte, L. Piatkowski, A. Woessner, Q. Ma, P. Jarillo-Herrero, N. F. Van Hulst and F. H. L. Koppens, "Hot-carrier photocurrent effects at graphene-metal interfaces," J. Phys.-Condensed Mat. **27**, 16 (2015).

[137] K. J. Tielrooij, J. C. W. Song, S. A. Jensen, A. Centeno, A. Pesquera, A. Z. Elorza, M. Bonn, L. S. Levitov and F. H. L. Koppens, "Photoexcitation cascade and multiple hot-carrier generation in graphene," Nat. Phys. **9**, 248-252 (2013).

[138] D. Sun, G. Aivazian, A. M. Jones, J. S. Ross, W. Yao, D. Cobden and X. Xu, "Ultrafast hot-carrier-dominated photocurrent in graphene," Nat. Nanotechnol. **7**, 114-118 (2012).

[139] T. Gong and J. N. Munday, "Angle-independent hot carrier generation and collection using transparent conducting oxides," Nano Lett. **15**, 147-152 (2015).

[140] T. Gong and J. N. Munday, "Materials for hot carrier plasmonics," Opt. Mater. Express **5**, 2501-2512 (2015).

[141] P. G. Etchegoin, E. C. Le Ru and M. Meyer, "An analytic model for the optical properties of gold," J. Chem. Phys. **125**, 164705 (2006).

[142] G. V. Naik, V. M. Shalaev and A. Boltasseva, "Alternative plasmonic materials: beyond gold and silver," Adv. Mater. **25**, 3264-3294 (2013).

[143] W. Shockley and H. J. Queisser, "Detailed balance limit of efficiency of p-n junction solar cells," J. Appl. Phys. **32**, 510-519 (1961).

[144] R. Brendel, J. H. Werner and H. J. Queisser, "Thermodynamic efficiency limits for semiconductor solar cells with carrier multiplication," Sol. Energy Mater. Sol. Cells **41/42**, 419-425 (1996).

[145] A. Luque and A. Marti, "Increasing the efficiency of ideal solar cells by photon induced transitions at intermediate levels," Phys. Rev. Lett. **78**, 5014-5017 (1997).

[146] A. S. Brown and M. A. Green, "Impurity photovoltaic effect: fundamental energy conversion efficiency limits," J. Appl. Phys. **92**, 1329-1336 (2002).

[147] D. J. Farrell, H. Sodabanlu, Y. Wang, M. Sugiyama and Y. Okada, "A hot-electron thermophotonic solar cell demonstrated by thermal up-conversion of sub-bandgap photons," Nat. Commun. **6**, 8685 (2015).

[148] A. De Vos, "Detailed balance limit of the efficiency of tandem solar cells," J. Phys. D-Appl. Phys. **13**, 839-846 (1980).

[149] M. A. Green, "Third generation photovoltaics: ultra-high conversion efficiency at low cost," Prog. Photovolt. **9**, 123-135 (2001).

[150] M. K. Hedayati, M. Javaherirahim, B. Mozooni, R. Abdelaziz, A. Tavassolizadeh, V. S. K. Chakravadhanula, V. Zaporojtchenko, T. Strunkus, F. Faupel and M. Elbahri, "Design of a perfect black absorber at visible frequencies using plasmonic metamaterials," Adv. Mater. **23**, 5410-5414 (2011).

[151] D. B. Suyatin *et al.*, "Strong Schottky barrier reduction at Au-catalyst/GaAs-nanowire interfaces by electric dipole formation and Fermi-level unpinning," Nat. Commun. **5**, 3221 (2014).

[152] J. R. Pugh, D. Mao, J.-G. Zhang, M. J. Heben, A. J. Nelson and A. J. Frank, "A metal:p-n-CdTe Schottky-barrier solar cell: photoelectrochemical generation of a shallow p-type region in n-CdTe," J. Appl. Phys. **74**, 2619-2625 (1993).

[153] A. Marti, J. L. Balenzategui and R. F. Reyna, "Photon recycling and Shockley's diode equation," J. Appl. Phys. **82**, 4067-4075 (1997).

[154] P. Wurfel, S. Finkbeiner and E. Daub, "Generalized Planck's radiation law for luminescence via indirect transitions," Appl. Phys. A-Mater. Sci. Process. **60**, 67-70 (1995).

[155] S. V. Boriskina, J. Zhou, W.-C. Hsu, B. Liao and G. Chen, "Limiting efficiencies of solar energy conversion and photo-detection via internal emission of hot electrons and hot holes in gold," Proc. SPIE **9608**, 960816 (2015).

[156] Q. Y. Chen and C. W. Bates, "Geometrical factors in enhanced photoyield from small metal particles," Phys. Rev. Lett. **57**, 2737-2740 (1986).

[157] U. Rau, U. W. Paetzold and K. Thomas, "Thermodynamics of light management in photovoltaic devices," Phys. Rev. B **90**, 035211 (2014).

[158] N. I. Landy, S. Sajuyigbe, J. J. Mock, D. R. Smith and W. J. Padilla, "Perfect metamaterial absorber," Phys. Rev. Lett. **100**, 207402 (2008).

[159] B. Y. Zheng, H. Zhao, A. Manjavacas, M. McClain, P. Nordlander and N. J. Halas, "Distinguishing between plasmon-induced and photoexcited carriers in a device geometry," Nat. Commun. **6**, 7797 (2015).

[160] Y.-F. Lao, A. G. Unil Perera, L. H. Li, S. P. Khanna, E. H. Linfield and H. C. Liu, "Tunable hot-carrier photodetection beyond the bandgap spectral limit," Nat. Photon. **8**, 412-418 (2014).

[161] Y. Cui, Y. He, Y. Jin, F. Ding, L. Yang, Y. Ye, S. Zhong, Y. Lin and S. He, "Plasmonic and metamaterial structures as electromagnetic absorbers," Laser Photon. Rev. **8**, 495-520 (2014).

[162] Y. Zhan, K. Wu, C. Zhang, S. Wu and X. Li, "Infrared hot-carrier photodetection based on planar perfect absorber," Opt. Lett. **40**, 4261-4264 (2015).

[163] V. G. Veselago, "The electrodynamics of substances with simultaneously negative values of SIGMA and MU," Soviet Phys. Uspekhi **10**, 509-514 (1968).

[164] D. R. Smith, J. B. Pendry and M. C. K. Wiltshire, "Metamaterials and negative refractive index," Science **305**, 788-792 (2004).

[165] T. Koschny, M. Kafesaki, E. N. Economou and C. M. Soukoulis, "Effective medium theory of left-handed materials," Phys. Rev. Lett. **93**, 107402 (2004).

[166] D. T. Viet, N. T. Hien, P. V. Tuong, N. Q. Minh, P. T. Trang, L. N. Le, Y. P. Lee and V. D. Lam, "Perfect absorber metamaterials: peak, multi-peak and broadband absorption," Opt. Commun. **322**, 209-213 (2014).

[167] D. R. Smith, S. Schultz, P. Markos and C. M. Soukoulis, "Determination of effective permittivity and permeability of metamaterials from reflection and transmission coefficients," Phys. Rev. B **65**, 195104 (2002).

[168] D. R. Smith, D. C. Vier, T. Koschny and C. M. Soukoulis, "Electromagnetic parameter retrieval from inhomogeneous metamaterials," Phys. Rev. E **71**, 036617 (2005).

[169] Z. Li, K. Aydin and E. Ozbay, "Determination of the effective constitutive parameters of bianisotropic metamaterials from reflection and transmission coefficients," Phys. Rev. E **79**, 026610 (2009).

[170] J. Y. Rhee, Y. J. Yoo, K. W. Kim, Y. J. Kim and Y. P. Lee, "Metamaterial-based perfect absorbers," J Electromagnet. Wave. **28**, 1541-1580 (2014).

[171] R. A. Shelby, D. R. Smith and S. Schultz, "Experimental verification of a negative index of refraction," Science **292**, 77-79 (2001).

[172] R. A. Shelby, D. R. Smith, S. C. Nemat-Nasser and S. Schultz, "Microwave transmission through a two-dimensional, isotropic, left-handed metamaterial," Appl. Phys. Lett. **78**, 489-491 (2001).

[173] G. Dayal and S. A. Ramakrishna, "Design of highly absorbing metamaterials for Infrared frequencies," Opt. Express **20**, 17503-17508 (2012).

[174] J. Hao, L. Zhou and M. Qiu, "Nearly total absorption of light and heat generation by plasmonic metamaterials," Phys. Rev. B **83**, 165107 (2011).

[175] D. Li, A. Babel, S. A. Jenekhe and Y. Xia, "Nanofibers of conjugated polymers prepared by electrospinning with a two-capillary spinneret," Adv. Mater. **16**, 2062 (2004).

[176] K. Aydin, V. E. Ferry, R. M. Briggs and H. A. Atwater, "Broadband polarization-independent resonant light absorption using ultrathin plasmonic super absorbers," Nat. Commun. **2**, 517 (2011).

[177] D. A. Bobb, G. Zhu, M. Mayy, A. V. Gavrilenko, P. Mead, V. I. Gavrilenko and M. A. Noginov, "Engineering of low-loss metal for nanoplasmonic and metamaterials applications," Appl. Phys. Lett. **95**, 151102 (2009).

[178] A. Boltasseva, "Empowering plasmonics and metamaterials technology with new material platforms," MRS Bulletin **39**, 461-468 (2014).

[179] G. V. Naik, J. Kim and A. Boltasseva, "Oxides and nitrides as alternative plasmonic materials in the optical range," Opt. Mater. Express **1**, 1090-1099 (2011).

[180] T. Lu and A. Srivastava, "Modeling and layout optimization for tapered TSVs," IEEE Trans. Very Large Scale Integr. (VLSI) Syst. **23**, 3129-3132 (2015).

[181] J. S. G. Bouillard, W. Dickson, D. P. O'Connor, G. A. Wurtz and A. V. Zayats, "Low-temperature plasmonics of metallic nanostructures," Nano Lett. **12**, 1561-1565 (2012).

[182] J. R. Haynes and W. Shockley, "The mobility and life of injected holes and electronics in germanium," Phys. Rev. B **81**, 835-843 (1951).

[183] W. Walukiewicz, "Intrinsic limitations to the doping of wide-gap semiconductors," Phys. B: Condens. Mat. **302-303**, 123-134 (2001).

[184] S. Law, D. C. Adams, A. M. Taylor and D. Wasserman, "Mid-infrared designer metals," Opt. Express **20**, 12155-12165 (2012).

[185] P. R. Hageman, W. J. Schaff, J. Janinski and Z. Liliental-Weber, "n-type doping of wurtzite GaN with germanium grown with plasma-assisted molecular beam epitaxy," J. Cryst. Growth **267**, 123-128 (2004).

[186] J. Kim, G. V. Naik, N. K. Emani, U. Guler and A. Boltasseva, "Plasmonic resonances in nanostructured transparent conducting oxide films," IEEE J. Sel. Top. Quantum Electron. **19**, 4601907 (2013).

[187] J. W. Cleary, R. E. Peale, D. J. Shelton, G. D. Boreman, C. W. Smith, M. Ishigami, R. Soref, A. Drehman and W. R. Buchwald, "IR permittivities for silicides and doped silicon," J. Opt. Soc. Am. B-Opt. Phys. **27**, 730-734 (2010).

[188] M. G. Blaber, M. D. Arnold and M. J. Ford, "A review of the optical properties of alloys and intermetallics for plasmonics," J. Phys.-Condens. Mat. **22**, 143201 (2010).

[189] G. V. Naik, J. L. Schroeder, X. Ni, A. V. Kildishev, T. D. Sands and A. Boltasseva, "Titanium nitride as a plasmonic material for visible and near-infrared wavelengths," Opt. Mater. Express **2**, 478-489 (2012).

[190] M. B. Cortie, J. Giddings and A. Dowd, "Optical properties and plasmon resonances of titanium nitride nanostructures," Nanotechnology **21**, 115201 (2010).

[191] H. Ferguson, U. Guler, N. Kinsey, V. M. Shalaev, T. B. Norris and A. Boltasseva, "Hot Electron Relaxation in Thin Titanium Nitride Films," in CLEO: QELS_Fundamental Science, FF2D.1 (2016).

[192] U. Guler, W. Li, N. Kinsey, G. V. Naik, A. Boltasseva, J. Guan, A. V. Kildishev and V. M. Shalaev, "Plasmonic Titanium Nitride Nanostructures for Perfect Absorbers," in Renew. Energy Environ., PW3B.8 (2013).

[193] T. Lu and A. Srivastava, "Detailed electrical and reliability study of tapered TSVs," 3D Syst. Integr. Conf. (3DIC), 2013 IEEE Int., pp 1-7 (2013).

[194] P. R. West, S. Ishii, G. V. Naik, N. K. Emani, V. M. Shalaev and A. Boltasseva, "Searching for better plasmonic materials," Laser Photon. Rev. **4**, 795-808 (2010).

[195] L. Zhou, Y. Tan, J. Wang, W. Xu, Y. Yuan, W. Cai, S. Zhu and J. Zhu, "3D self-assembly of aluminium nanoparticles for plasmon-enhanced solar desalination," Nat. Photon. **10**, 393398 (2016).

[196] Th. Koschny, P. Markos, E. N. Economou, D. R. Smith, D. C. Vier and C. M. Soukoulis, "Impact of inherent periodic structure on effective medium description of left-handed and related metamaterials," Phys. Rev. B **71**, 245105 (2005).

[197] A. Boltasseva and H. A. Atwater, "Low-loss plasmonic metamaterials," Science **331**, 290 (2011).

[198] C. Gong and M. S. Leite, "Noble metal alloys for plasmonics," ACS Photon. **3**, 507513 (2016).

[199] R. Martel, V. Derycke, C. Lavoie, J. Appenzeller, K. K. Chan, J. Tersoff and Ph. Avouris, "Ambipolar electrical transport in semiconducting single-wall carbon nanotubes," Phys. Rev. Lett. **87**, 256805 (2001).

[200] J. Cumings and A. Zettl, "Low-friction nanoscale linear bearing realized from multiwall carbon nanotubes," Science **289**, 602-604 (2000).

[201] K. Yu, G. Lu, Z. Bo, S. Mao and J. Chen, "Carbon nanotube with chemically bonded graphene leaves for electronic and optoelectronic applications," J. Phys. Chem. Lett. **2**, 15561562 (2011).

[202] W. H. Shin, H. M. Jeong, B. G. Kim, J. K. Kang and J. W. Choi, "Nitrogen-doped multiwall carbon nanotubes for lithium storage with extremely high capacity," Nano Lett. **12**, 22832288 (2012).

[203] S. Hong and S. Myung, "Nanotube electronics: a flexible approach to mobility," Nat. Nanotechnol. **2**, 207-208 (2007).

[204] M. Freitag, Y. Martin, J. A. Misewich, R. Martel and Ph. Avouris, "Photoconductivity of single carbon nanotubes," Nano Lett. **3**, 10671071 (2003).

[205] H. Kataura, Y. Kumazawa, Y. Maniwa, I. Umezu, S. Suzuki, Y. Ohtsuka and Y. Achiba, "Optical properties of single-wall carbon nanotubes," Synth. Met. **103**, 2555-2558 (1999).